BIO-FUNCTIONAL COATING ON SELECTIVE LASER MELTING MANUFACTURED POROUS TI6AL4V SCAFFOLDS PRODUCED BY USING PLASMA ELECTROLYTIC OXIDATION

By

Siti Hidayatul Aqmar binti Zakaria

A thesis submitted in partial fulfillment of the requirements for the degree of Doctor of Engineering

Supervisor: Professor Masahiro Todoh

Division of Human Mechanical Systems and Design

Graduate School of Engineering, Hokkaido University

October 2020

ABSTRACT

The recent advances in manufacturing such as selective laser melting (SLM) have allowed the fabrication of complex geometries and lightweight three-dimensional (3D) components. Lattice structure serves as an alternative design to existing implants by reducing the stiffness thereupon to eliminate the stress-shielding effect whilst improving the osseointegration process. In purpose to reinforce the osseointegration with the adjacent tissue after the surgery, the porous scaffold is coated with bio-functional coating by using plasma electrolytic oxidation (PEO) technique. Ti6Al4V has been material of choice for medical application and it is viable for SLM technology and PEO technique. The aim of this study is four-fold. Firstly, to develop SLM manufactured porous Ti6Al4V coated with a bio-functional PEO-treated layer. Secondly, to evaluate the characteristics of bio-functional PEO coatings on SLM manufactured porous Ti6Al4V scaffolds. Thirdly, to investigate the mechanical properties of scaffolds and the effect of PEO process on mechanical strength of SLM manufactured scaffolds. Fourthly, and last, to identify the bioactivity of the PEO-treated scaffolds with Simulated Body Fluid (SBF) immersion test.

Coating formed were probed using field emission scanning electron microscopy (FESEM), electron dispersive spectroscopy (EDS), X-ray diffraction analysis (XRD) and X-ray photoelectron spectroscopy (XPS). ImageJ open software was used to carry out image analysis, which allowed the investigation of coating properties such as size of micropores formed on the coating. The compressive test according to ISO 13314:2011 was conducted on the scaffolds and showed a comparable result to human cancellous bone mechanical properties. The scaffolds also have the ability of apatite formation after 28 days of immersion time.

This study has indicated the potential of PEO treatment of Ti6Al4V porous scaffolds for orthopedic implants in the aspect of bio-functionality and bioactivity of the coating. Additionally,

PEO treatment slightly enhances the mechanical properties of SLM manufactured Ti6Al4V porous scaffolds with increasing treatment time. These results provide a benchmark against which further work optimizing PEO process parameters on SLM manufactured porous Ti6Al4V to enhance the bio-functionality of scaffolds could be undertaken.

ACKNOWLEDGEMENTS

At the very outset of this thesis, I would like to extend my sincere and heartfelt obligations towards all the personages who have helped me in this endeavor. It would not have been possible to write this doctoral thesis without the help and support of the kind people around me.

Most of all, I would like to record my heartfelt admiration and gratitude to my principal supervisor, Prof. Masahiro Todoh, who took me under his wing and has been supporting my work right up to the end. I am ineffably indebted to my co-supervisor, Prof. Dato' Ir. Dr. Mohd Hamdi Abd Shukor, for his insightful advice, constructive criticism and unsurpassed knowledge of coating and manufacturing technology.

I would like to thank my Ph.D. financial sponsor, Japan International Cooperation Agency (JICA) via JICA Innovative Asia Program, in which without the scholarship I would not have been able to carry out this research.

Sample preparation of the research has been performed within the collaborative research project with Centre of Advanced Manufacturing and Material Processing (AMMP), University of Malaya. I would like to thank researchers and staffs at the organization, particularly Dr. Farazila binti Yusof for invaluable advice, support, and friendship on both an academic and a personal level during my research stay.

Thanks are also due to Dr. Kaori Kuribayashi-Shigetomi from Nitobe College in particular for unleashing my potential in research presentation skills and not forgetting Prof. Datuk Paduka Dr. Hj. Kamaruzaman Jusoff from UKM Press for his one-on-one guidance and advice in writing an excellent manuscript.

I also acknowledge with a deep sense of reverence, my gratitude towards my parents and siblings. My family has given me their unequivocal support throughout, as always, for which my mere expression of thanks likewise does not suffice. Thanks are also due to my friends and lab mates who stood by me when things became increasingly difficult and burdensome with a big pile of works to do.

Any omission in this brief acknowledgment does not mean a lack of gratitude.

Aqmar Zakaria,
Hokkaido, Japan,
October 2020

CONTENTS

FIGURE CAPTIONS

TABLE CAPTIONS

CHAPTER 1: INTRODUCTION

A key building block of bone is the organic and inorganic components. The organic components are collagen extra-cellular matrix (ECM) and the inorganic components are calcium phosphate or hydroxyapatite (HAp) along with a large quantity of water. In the case of naturally occurring HAp compared to synthetic HAp, its non-stoichiometric form contains other elements than its base component, such as carbonates, sodium, and silicon ions. The osseointegration mechanisms of HAp include the HAp dissolution from the coating and formation of apatite layer. Subsequently, the ions exchange, absorb and incorporate biological molecules into the apatite layer. These ameliorate the differentiation and proliferation of osteoblast cells (matrix-producing cells) on the surface of HAp bulk. However, brittle properties of HAp hinder their use as potential material for implants in load-bearing applications.

Titanium has been a biocompatible material in the field of orthopedic and orthodontic implants to substitute defect joints, stabilize fractures and reduce pain. Despite the biocompatibility properties, titanium is bioinert material which does not promote excellent bone in-growth on the surface. Therefore, surface treatment is introduced on the bare metal implants, to induce bone adhesion on the surface of the implants. Synthetic HAp is the most common material used for coatings in the orthopedic and orthodontic field. The deposition of HAp coating on the metallic substrates would gain the upper hand in the success of implants which combines the benefit of the good strength of titanium and bone bonding ability of the surface coating. The bioactive coating would also interfere with the bacterial colonization, hence, reduce the post-implant infection. In addition, the bioactive coating would enhance the cell adhesion thus reduce the implant loosening.

Metal additive manufacturing techniques such as selective laser sintering, SLM and electron beam melting (EBM) have enabled the fabrication of remarkably interconnected porous titanium alloy biomaterials with accurately controlled micro-architectures. Additively manufactured porous structure is fully interconnected, has a precisely-controlled pore size that structurally similar, for example, bone tissue pore size to optimize cell attachment, proliferation, and migration, and would exhibit mechanical properties similar to bone mechanical properties. Furthermore, the abundant pore space allows the incorporation of bioactive material that releases calcium and phosphate ions to boost the bone regeneration performance of the biomaterial.

1.1 AIM AND OBJECTIVES

The overall aim of this project is to develop a bio-functional coating on additively manufactured porous Ti6Al4v scaffold produced by using PEO technique. This research project is divided into three different phases. Figure 1 summarizes these phases.

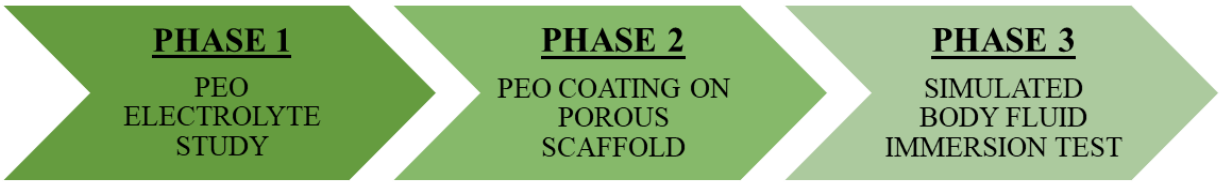

Figure 1. Three different phases of this research study.

1. Phase 1

   During this phase, an electrolyte was developed with different chemicals that contain calcium and phosphate elements. At an early stage, the developed electrolyte was investigated with Ti6Al4V substrate to verify the electrolyte either it is able to allow the formation of a bio-functional coating or not. The coating formed on Ti6Al4V was analyzed by FESEM, EDS, XRD, and micro-scratch test.

2. Phase 2

   Ti6Al4V porous scaffolds were fabricated by using SLM technique and coated with bio-functional layer with PEO. FESEM was used to study surface morphology and thickness of the coating. EDS, XRD and XPS were used to investigate chemical composition of the coatings. Finally, a compression test was conducted to assess the effect of PEO coating on the mechanical properties of the scaffolds.

3. Phase 3

   In the final phase, bioactivity of the coating was examined with simulated body fluid (SBF) immersion test. The apatite formation on the coating was analyzed using FESEM, EDS, XRD and XPS.

The objectives of this project are to:

1. Verify the formation of bio-functional coating on the Ti6Al4V substrate with developed electrolyte solution containing calcium, phosphate, and fluoride elements.
2. Investigate the characteristics of PEO coatings on 3D printed porous Ti6Al4V scaffold.
3. Examine the effect of PEO on the mechanical properties of scaffolds.
4. Evaluate the bioactivity (apatite formation ability) of PEO coated scaffold with SBF immersion test.

1.2 DISSERTATION OVERVIEW

Chapter 2 provides an overview of the PEO process and resulting surface morphologies. It also overviews additive manufacturing in particular SLM method and existing study of PEO coating on porous scaffold.

Chapter 3 presents details of surface characterization methods utilized in the present work. The equipments and analysis include FESEM, EDS, XRD and XPS. Furthermore, microscratch test method on coating layer of Ti6Al4V plate is presented in this chapter.

Chapter 4 introduces PEO treatment on Ti6Al4V plate substrate with our electrolyte solution to introduce bio-functional elements on the coating. The adhesion strength is conducted to examine the mechanical properties of the PEO coating. The surface morphologies are analyzed using FESEM and chemical compositions are investigated using EDS, and XRD.

Chapter 5 discusses PEO treatment on Ti6Al4V additively manufactured porous scaffold with similar electrolyte solution as mentioned in Chapter 4. The surface morphologies and chemical compositions are analyzed using similar technique as mentioned in Chapter 4 with addition of XPS analysis. The effect of PEO treatment on mechanical properties of porous scaffolds is investigated by conducting quasi static compression test and the results are presented in this chapter.

Chapter 6 discusses the bioactivity of the coating for both types of substrate; plate and additively manufacture porous scaffold, with SBF immersion test. The apatite formation on the coating surface after 28 days of immersion is examined.

Chapter 7 summarizes and concludes the major findings of this study and provides the outlook for further research.

CHAPTER 2: LITERATURE REVIEW

2.1 PLASMA ELECTROLYTIC OXIDATION (PEO)

PEO or microarc oxidation [1] or anodic spark deposition [2] is an electrochemical surface treatment technique for valve metals such as aluminum, magnesium and titanium [3]. The topic related to PEO has been gaining attention in these recent years due to its irrefutable benefits. Figure 2 indicates the number of publications with titles including the words "plasma electrolytic oxidation" on Sciencedirect website is increasing over years. The PEO process involves immersing the substrate which acts as an anode in an aqueous electrolyte solution [4] and the stainless-steel tank that holds the electrolyte or stainless-steel cooling tube which acts as a cathode [5]. The voltage applied for PEO process is also higher than conventional anodization method; this allows discharge to occur at the substrate/electrolyte interface [6,7]. During the process, oxide coating would grow on the surface of substrate with complex composition composing of multiple elements emanate partly from the substrate and partly from electrolyte. The discharge and plasma could be observed on the coating/electrolyte interface during the process due to higher potential and current densities applied by an external power supply and result in formation of unique porous surface morphology which has triggered significant interest in the biomedical field.

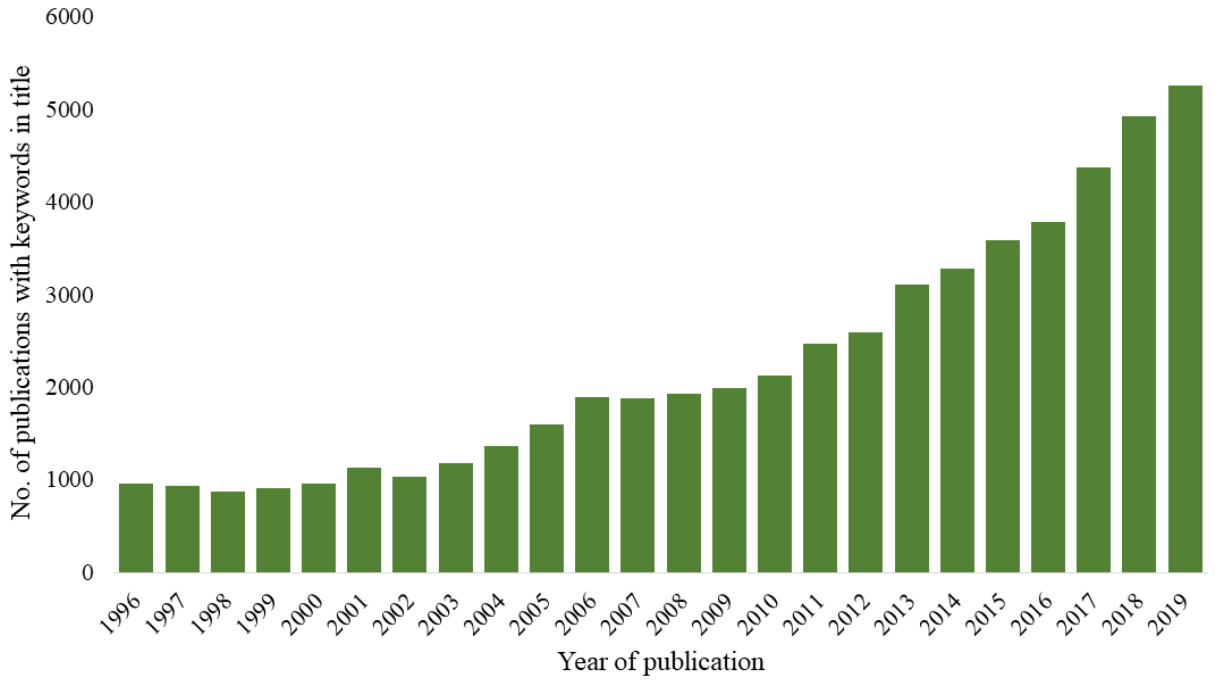

Figure 2. Increasing number of studies on PEO found on Sciencedirect website.

To control the properties and functionality of PEO coating formed on the substrate, several parameters, for instance as shown in Figure 3, treatment time [8,9], electrical parameters [10,11], electrolyte solution [12,13], and substrate [14], may be adjusted. From all these factors, a key parameter that would bring a great effect on the PEO coating is the chemical constituent of electrolyte solution by adjusting the chemical species or by adding different additives [15,16]. Additionally, alkaline solution has been a primary option for PEO electrolyte [17].

Micro-arc discharge formation is a unique event which eventually contributes to the deposition of anodic oxide film on the light metal surface during PEO process. A few researchers have attempted to investigate the nature of spark discharge triggering by the applied high voltages [18–20], yet it is still not fully understood due to the complexity to analyze an individual sparking event.

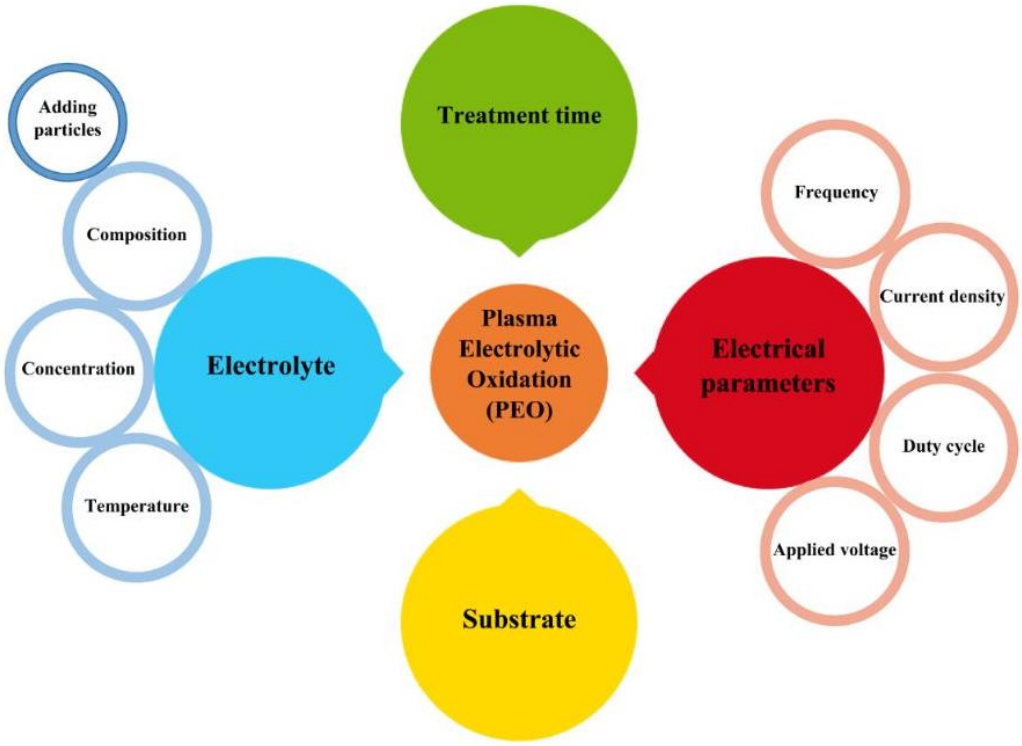

Figure 3. Main PEO parameters that can be modified to tailor coating layer [6].

2.2 EFFECTS OF ELECTROLYTE

The underlying effects of electrolytes to PEO process are briefly explained as follows: (i) induce spontaneous metal passivation to deposit a thin insulating film and initiate dielectric breakdown to generate spark discharge; (ii) complete the circuit, conduct current and convey required energy for anode oxidizing occur at the interface of substrate/electrolyte; (iii) serve as an oxygen source in the form of oxysalt required for oxidation; (iv) responsible for surface modification by incorporating components consisting in the electrolyte solution which eventually modify the features of PEO coatings.

The leading sine qua non for dielectric breakdown, additives, for instance, silicates, aluminates, and phosphates has been widely used in electrolyte solution preparation to promote

strong surface passivation. The advantages of these three groups of additives thereby are as follows: (i) promote swift sparking voltage; (ii) allow the incorporation of the species consist in the electrolyte into the coating in a facile manner by poly-reactions and deposition; (iii) deposition of wear- and corrosion-resistant coating with the utilization of cost-effective and environmental friendly electrolyte that would benefit for the commercial purpose.

Anion additives such as Na_2WO_4 [21] to enhance erosion and corrosion resistance and fine powder additives with hard, high melting point materials (SiC, ZrO_2) [22], coloring agents (chromia pigment, Darvan C-N) [23] and organic and/or inorganic HAp [24,25], can be introduced into the electrolyte solution for particular applications, obtaining cataphoretic effects to be incorporated into the coating.

2.3 BASIC AND UNIQUE CHARACTERISTICS OF PEO COATINGS

Surface porosity

Pore formed on PEO coating morphology is attributed to the spark discharge intensity. Curran et al. [26] showed in their study that approximately 20% of the pore population is in micrometer scale can be found on aluminium alloys and 40% on coating formed on Mg alloys. The morphology of pores has a prominent influence on features and characteristics of PEO coatings.

On the one hand, typical PEO coating consists of interconnected pores, which is favorable for osteoblast cell anchorage in orthopedic applications as well as natural enclosure for surface impregnation with a wide variety of compounds to enhance the properties and functionality of the coating. A study by Teixeira et al. [27], reported surfaces with 62 μm pore size yield better expression of osteoblast phenotype. This study suggests that the 3D design of the porous structures

which has trabecular bone alike structures would encourage cell proliferation as well as enhance bone ingrowth. However, the optimum pore size and surface morphology for bone ingrowth are still in debate.

On the other hand, due to the presence of pores, the coatings are susceptible to the degrade mechanical properties and low thermal conductivity and poor corrosion resistance. However, low stiffness limits the differential thermal expansion stresses over the surface and low conductivity promotes an effective thermal barrier function, which is favorable for thermal protection of the substrates.

High adhesive strength between substrate and coating

It has been proved that high adhesive strength coatings can be achieved by using PEO process. The mechanisms of coating growth – dissolution of substrate – contribute to this characteristic. Empirical results from scratch tests have confirmed the fact. Yerokhin et al. [28] investigated the adhesive strength of PEO coating deposited on aluminium alloy from an alkaline electrolyte consisting of additives Na_2SiO_3 and $Na_2P_2O_7$ and found the critical load Lc1 6.8-7.7N. The strength is a little bit feeble, yet it is satisfactory for major tribological applications. Wang et al. [29] evaluated shearing strength PEO coating formed after immersion in silicate and aluminate based electrolytes and compared both results. The coating forming in aluminate electrolyte (14 MPa) demonstrated higher value compared to coating forming in silicate electrolyte (11 MPa). According to their study, treatment time which is longer than 30 minutes would reduce the mechanical properties of the coating. Generally, longer treatment time would increase the coating thickness, hence the weaker the adhesion strength of coating to substrate surface.

Internal stress of the coating

Investigating residual stress in PEO coating is essential due to the effect of internal stress on the mechanical properties, for instance, hardness, adhesion, wear resistance and fatigue cracking. In order to comprehend the importance of internal stress for the mechanical properties of the coating, Khan et al. [30] studied the formation of residual stresses in PEO coating on BS Al 6082 alloy by using $\sin^2\Psi$ X-ray diffraction technique. They found that normal stress varies from -111 (±19) MPa to -818 (±47) MPa as well as shear stress differs from -45 (±27) MPa to -422 (±24) MPa. The values of internal normal stress and shear stress were influenced by the applied PEO current pulse parameters during the process. In another study by Guan et al. [31], a four-point bending test was performed to investigate the failure mechanisms of PEO coating and interface fracture of PEO coating was observed. The plastic deformation in the substrate revealed that the interfacial crack extension caused plastic deformation in the substrate and the crack could be categorized as ductile crack. Furthermore, the compression strength of the coating is about 600 MPa obtained from finite element analysis.

2.4 PEO COATING ON TI ALLOYS SUBSTRATE FOR ORTHOPEDIC APPLICATION

One of standard materials for orthopedic and dental implants is titanium and its alloys owing to their good biocompatibility, high strength to weight ratio and excellent corrosion resistance. Yet, titanium has bio-inert properties that would limit their usage in medical applications. Therefore, PEO surface treatment has been implemented to enhance the bio-functionality of the titanium-based implants. The first PEO coating on titanium substrate containing Ca and P was developed by Ishizawa et al. [32]. The main purpose of their study is to improve biocompatibility of titanium by immersing the substrate in electrolyte prepared with calcium compounds for PEO treatment. The typical PEO coating morphology has micropores which is beneficial for bone in-growth,

enhance osteointegration and eventually attain strong chemical bonding between implant and adjacent tissue.

Besides electrolyte compositions that contain calcium salt, applied electric regime also partially plays a key role in the formation of bioactive components. High voltage provokes a large arc discharge intensity, which promotes the crystalline transformation from amorphous phase on the coating surface. Titania-based coatings are easily produced at high voltages which is rich in crystalline phases of TiO_2, $CaTiO_3$, $Ca_2P_2O_7$ and $Ca_3(PO_4)_2$ or TiO_2 and HAp. This type of coating has high bioactivity for orthopedic purposes. In contrast, PEO coatings produced at low voltages compose mainly of TiO_2 phases with a tiny amount of amorphous phase and are weak or do not have ability for apatite-forming ability.

2.5 ADDITIVE MANUFACTURING: SELECTIVE LASER MELTING AND ITS APPLICATION IN MEDICINE

Additive manufacturing (AM) or Rapid Prototyping or 3D printing is an alternative approach to conventional manufacturing to improve the effectiveness in the manufacturing of complex parts which has been becoming drawbacks in traditional or conventional manufacturing. Computerized Numerical Control (CNC) is a well-known conventional manufacturing process, involving subtraction of material to obtain the desired geometry, contrary to AM process, the desired geometry creates by adding material to form the desired product.

There are seven categories of AM namely, vat photopolymerization, material jetting, binder jetting, powder bed fusion (PBF), material extrusion, directed energy deposition and sheet lamination. Albeit the differences between process, entire categories have a similar main concept of creating process by building the part or product layer upon layer based on the design from digital file in 3D. This alludes that the 3D piece is built by the superposition of a subtle two-dimensional

(2D) sheet in each layer. AM technology has allowed the fabrication of complex geometries or parts in a facile manner which is impossible by using other or conventional manufacturing processes.

Powder bed fusion is a process whereby the heat source selectively melts or sinter a metallic powder to form 3D objects. PBF can further be categorized into two major techniques; laser melting or laser sintering and EBM which both techniques use a different type of power source. Yet, basic principles of both techniques are similar. The laser beam is passed to powder particles within a powder bed platform, which gradually gauges down as each layer is completed and new powder is spread on the top of the previously built surface and the process is repeated until the powder is consolidated into the desired 3D object.

SLM utilizes high power-density laser to fully melt and fuse metallic powder into a 3D object [33]. Figure 4 shows the schematic diagram of a typical SLM. SLM still stays as an expensive manufacturing technique, therefore it is mainly used in high value-added industries such as medical. Furthermore, the aptitude of this technique to fabricate metallic complex geometries with porous structure has allowed researchers to develop lightweight structures for the automotive and aerospace industries as well as conformal cooling channels for tooling.

Implant performance depends on the ability to bear mechanical loading concurrently the implant should have stiffness as low as adjacent tissue to avoid stress shielding from happening. Therefore, SLM-manufactured implants have been developed as a novel approach and design since the regular porous structure can be precisely controlled pore shape, pore size, and pore distribution within the implant design. This approach is susceptible to improving the long-term functionality of implants with bone-mimicking properties. Besides, it is possible to fabricate patient-specific

design implants with SLM and promote and accelerate bone ingrowth as the key success of AM implant is the achievement of osseointegration.

An SLM-manufactured biocompatible metal framework for dental prostheses has been developed by Kruth et al. [34]. A study by Wehmoller et al. [35] reported the feasibility of complex biological structures at macroscale and integration of microstructure geometry into the body implants of cortical bone, mandibular canal segment, and tubular bone made from titanium and stainless steel by means of SLM. Chen et al. [36] also reported the development of SLM denture frameworks with the same materials. Bibb et al. [37] confirmed that SLM is viable to manufacture steel parts for medical applications and they presented four successful case studies in surgical guides of different maxillofacial surgeries.

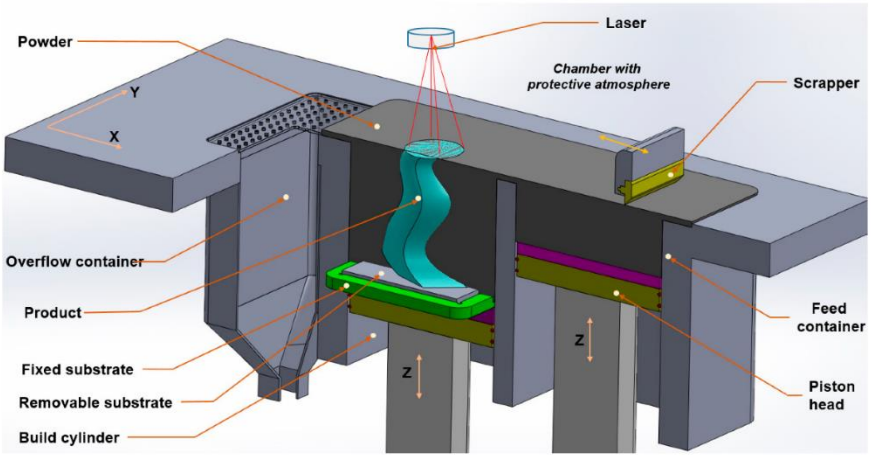

Figure 4. Schematic diagram of SLM [38].

2.6 PEO ON POROUS SCAFFOLD FOR ORTHOPEDIC APPLICATION

Although SLM manufactured macro-porous geometries are excellent design in implants, the challenges correlated to surface characteristics remain a limitation to allow bone ingrowth on the implant surface. For instance, a titanium-based implant is difficult to interact with host bone due

to their bioinert properties which may lead to fibrotic lining or scar tissue at bone/implant interface and eventually degrade implant fixation [39]. Therefore, surface treatment is crucial to the success of metallic prostheses. However, surface treatment on a scaffold or complex geometries is more complicated than that bulk material and only limited technique can be implemented. But, thankfully, PEO may be a potential effective surface treatment technique to form bio-functional coating on valve metals with complex geometry. Generally, metallic implants have smooth surfaces with low wettability that would limit the cell to adhere to the surface. A few researchers have investigated the relationship between surface roughness and cell proliferation or differentiation and they found the surface roughness within the range of 0.16 -2.19 μm is desirable for cell proliferation [40,41].

Xiu et al. [42] developed 3D printed porous titanium manufactured by EBM technique and coated the surface with a homogeneous TiO_2 and amorphous calcium phosphate with micro-arc oxidation method. Coated porous titanium scaffold exhibited enhanced apatite forming ability, alkaline phosphatase activity and cytocompatibility. After implantation of the treated scaffold into a rabbit model, the bone formation increased both in and around the scaffolds compared to uncoated scaffolds in which the bone only grew at the periphery of the scaffold. A push-out test demonstrated stronger osteointegration strength on the MAO treated scaffold.

Recently, Hengel et al. [43] reported development of selective laser melted porous titanium bone implants coated with HAp containing strontium and silver nanoparticles. The coating layer was deposited on the surface of porous titanium by means of PEO. Assessment of antibacterial activity exhibited the coating can eliminate methicillin-resistant *Staphylococcus aureus* in vitro and in an ex vivo murine model. Furthermore, this synergistic approach enhanced osteogenic behavior of the PEO treated porous titanium and showed higher levels of alkaline phosphatase

activity compared to non-treated porous titanium. Karaji et al. [44] investigated the effect of PEO on the mechanical properties of SLM-manufactured scaffolds based on the cubic unit cell with four different relative density. The static compression test results revealed that relative density considerably affected the mechanical properties of the scaffolds. Nevertheless, the results obtained demonstrated PEO treatment did not affect the mechanical properties of scaffolds except for elastic modulus. In addition, all the scaffolds in this study can bear cyclic loading of 10^6 cycles at 70% of their yield stress.

CHAPTER 3: BIO-FUNCTIONAL COATING ON TI6AL4V SURFACE PRODUCED BY USING PLASMA ELECTROLYTIC OXIDATION

3.1 INTRODUCTION

Titanium and its alloys have been widely used for medical applications. In particular, titanium is a feasible material for dental and orthopedic implants owing to its excellent properties, including high strength-to-weight ratio, corrosion resistance, and bioinert properties [45]. Despite those advantages, titanium always exhibits weak biological bonding with adjacent tissues [46]. Therefore, the incorporation of bioactive materials at the titanium/bone tissue interface would enhance the functionality and bioactivity of titanium substrates. Calcium phosphate, or HAp, is among the main natural elements of the bone and has the potential to endow bone formation on the implant surface [47]. Fluoride is a sought after element for its antibacterial effects [48]. It is able to disrupt bacterial metabolism and boost the proliferation and differentiation of osteoblast cells. Antibacterial properties are not only crucial to prevent dental caries for dental implants, but they also hinder initial post-surgery infections after the insertion of orthopedic implants, which always leads to implant failure [49]. The combination of HAp or tricalcium phosphate with fluoride is known as fluorapatite (FAp), and has been recently corroborated to bear the potential of reinforcing mineralization and crystallization of HAp on the coating surface. Therefore, FAp would extensively increase the performance and durability of dental implants and prostheses.

In order to incorporate these elements onto and into the coating layer, a surface treatment technique could be applied. Thus, surface treatment methods, such as conversion coating, electroplating, anodization, PEO, organic coating, and vapor-phase processes have been exploited as a means to accomplish this purpose. Among these methods, PEO, or micro-arc oxidation, has been employed on valve metals and its alloys, namely Mg, Ti, Al, and Zr, with alkaline or

phosphate electrolyte solutions, which is then followed by micro-spark formation, resulting in a ceramic-like coating. PEO is one of the techniques that has gained attention in recent years [50]. The development of bio-functional PEO-treated coating with an electrolyte solution consisting of bio-functional elements such as Zn, Mg, Mn, Si and Sr recently seems to be necessary [51,52]. Besides, the incorporation of calcium and phosphate elements via the PEO of Ti alloys has been reported by several authors [3], [7]–[10]. Despite the need for implants to have antibacterial properties, only several antibacterial coatings have been developed by using distinct antibacterial elements such as Cu, Ag, Zn, and Zr through the PEO technique, and their antibacterial properties have been examined [57–59]. PEO coating incorporated with fluoride element has been investigated until the present time for various purposes such as to enhance the corrosion resistance of Mg and Al [60–62]. More specifically, Santos-Coquillat et al. studied PEO coating enriched with fluoride to reinforce the biological performance of titanium implants [49,63]. PEO coatings are commonly amorphous or crystalline in phases, and the additional elements of the coating could be possibly tailored by adjusting the process parameters and electrolyte constituents. During PEO treatment, the TiO_2 layer is initially formed, then the cationic and anionic components are merged into the coating layer. As previously mentioned, by introducing calcium phosphate and fluoride to the substrate surface [53,64], it would promote a better bone ingrowth to the implant surface [65].

Santos-Coquillat et al. [49] developed a multifunctional PEO coating on a Ti6Al4V substrate for orthopedic applications by incorporating Ca and P as bioactive elements and adding Si and F as antibacterial elements. Hydrogen fluoride, nitric acid, and calcium carbonate were used as the electrolyte solution in this study. The authors studied the effect of treatment time on the coating composition and its morphology, and they investigated the coating's bioactivity and antibacterial effect with osteoblast cells and *S. aureus*, respectively. The result demonstrated that

a longer treatment time altered the TiO_2 phase from anatase to rutile and promoted the generation of HAp and FAp. With respect to the antibacterial effect, the coating with the highest amount of fluoride exhibited the least number of bacteria on the coating surface, up to 60%, which is a significant result. Hence, this study exhibits that fluoride is an excellent candidate as an antibacterial element.

A prior study has documented the effectiveness of using a CaF_2 additive in a phosphate electrolyte solution to form an oxide layer on a magnesium alloy by PEO, which then successfully improved the corrosion resistance and bioactivity of the substrate [66]. In the present work, we extend the study on the growth of bio-functional coatings with a one-step PEO approach, using alkaline phosphate electrolyte solution containing trisodium orthophosphate, potassium hydroxide and calcium fluoride, on Ti6Al4V. The results discuss the electrical response, phase composition of the coating and the mechanism of coating growth, surface and cross-section morphologies, and the adhesion of the coating onto the substrate, which were determined by micro-scratch tests.

3.2 MATERIALS AND METHODS

3.2.1 TI6AL4V PLATE SUBSTRATE PREPARATION

Ti6Al4V substrates of 15 mm × 15 mm × 2 mm (Figure 5) were abraded with SiC emery paper up to 2000 grade. Subsequently, they were polished with an Extec Chemic Cloth and diamond suspension. Then, the abraded substrates were rinsed with distilled water and cleaned ultrasonically with 70% ethanol and distilled water before PEO treatment. These cleaning procedures were conducted to ensure that the surfaces of the substrates were free from contaminants prior to the PEO experiments.

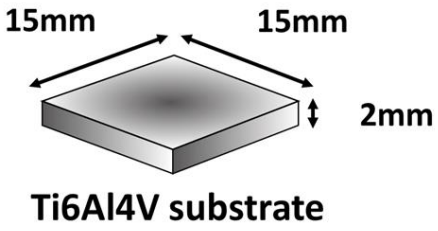

Figure 5. Ti6Al4V plate substrate dimension.

3.2.2 PEO TREATMENT SET UP

Ti6Al4V (Tokyo Titanium Co., Ltd ., Japan) substrates were immersed in the electrolyte. The electrolyte solution comprised 5 g of tri-sodium orthophosphate (Ajax Finechem, Australia), 3 g of calcium fluoride (Sigma -Aldrich, United States), and 2 g of potassium hydroxide (Sigma-Aldrich, United States) in 1000 mL distilled water with a pH of 12.55. Then, the solution was stirred using a magnetic stirrer for 2 hours and subsequently sonicated using an ultrasonic bath for another 2 hours. These two steps are crucial to ensure the chemical powders are well dissolved in distilled water and to prevent any settling and agglomeration of the powder particles. The substrates were set as the anode, and the stainless-steel beaker containing the electrolyte solution served as the cathode. Recommended material for the cathode in the PEO process is an inert material such as stainless steel with a purpose simply to complete the circuit. PEO treatment was performed for 10 min under an auto-ranging DC power supply unit (Keysight Technologies Deutschland GmbH, Model No: N8957A, Germany) with a maximum voltage of 1500 V and a current capacity of 30 A. The setup was equipped with a stirrer to ensure the consistency of the electrolyte and a water-cooling system to maintain the electrolyte at a low temperature during the process (Figure 6). The temperature of the electrolyte was recorded before and upon completing the treatment. Before the process, the temperature was 23 °C, and it eventually increased to 53 °C

upon turning off the power supply. Considering the safety of the PEO user, the temperature of the electrolyte was not measured during the process. The parameters that were used for the PEO treatment are shown in Table 1. The electrical response was recorded throughout the process.

Table 1. Parameters set during PEO process.

PEO Parameters	**Quantity**
Voltage threshold (V)	400
Maximum current applied (A)	1
PEO treatment time (min)	10

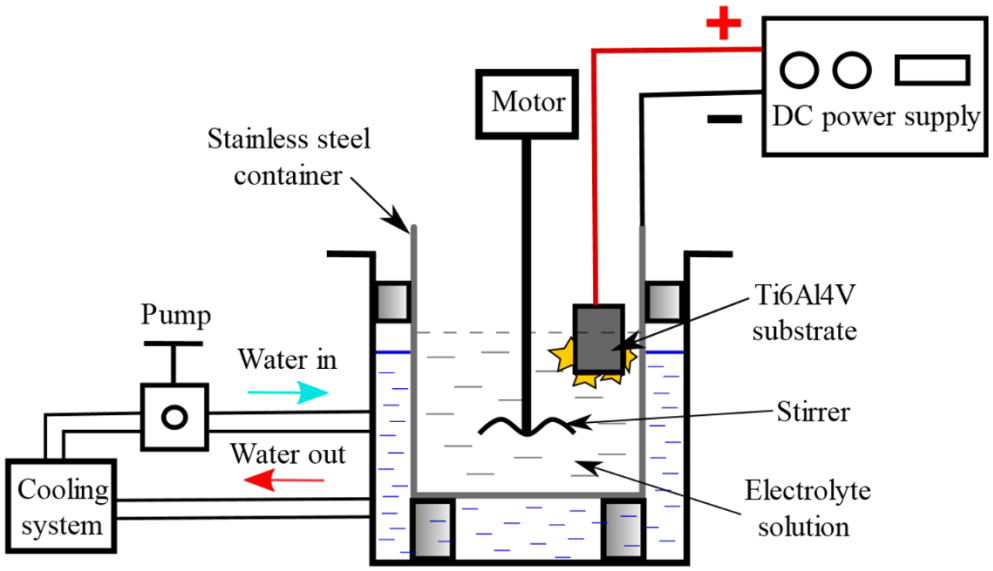

Figure 6. In-house PEO setup.

3.2.3 COATING CHARACTERIZATION

3.2.3.1 FESEM AND EDS ANALYSIS

Surface morphology and elemental composition of the coated substrates was observed by FESEM and EDS (FESEM-EDS, JSM-7001FA, JEOL, Japan) (Figure 7). Pore density population and sizes on the coating were estimated by using open source software ImageJ. The substrate was cross-sectioned and carbon-coated to study the thickness and the distribution of the elements across the coating.

Figure 7. FESEM-EDS at Creative Research Institution (CRIS), Hokkaido University.

3.2.3.2 X-RAY DIFFRACTION ANALYSIS

The coating layer formed on the Ti6Al4V plate was analyzed using a Rigaku Smartlab XRD (CuKα = 0.154056 A°) at a step size of 0.02° for plate substrate and 0.1° for porous scaffolds substrate and scanning speed of 2° per minute from 5° to 90° scan range of 2θ. Then, the phase compositions of the PEO coating were analyzed using PDXL Version 2.2 (Rigaku Corporation, Tokyo, Japan) software, which is an integrated XRD analysis software for Rigaku Smartlab XRD.

3.2.3.3 MICROSCRATCH TEST

Micro-scratch tests (Micro Materials Ltd. Wrexham, UK) were performed on the coating of Ti6Al4V plate only by using a conical Rockwell diamond tip of radius 25 µm. The scratch length was set to 1000 µm, and a linearly increasing load in the range of 0-2000 mN was fixed. The onset of delamination at critical load Lci was taken as the adhesion strength of the coating substrate system. Finally, the scratch track was probed by optical microscopy to observe the failure modes of the coating.

3.3 RESULTS AND DISCUSSION

3.3.1 ELECTRICAL RESPONSE OF PEO COATINGS

Figure 8 displays the typical output voltage shift and current behavior that were acquired during the PEO process of the Ti6Al4V substrate. According to few studies [18,67,68], the plot could be segregated into four different stages, indicating the changes in coating resistance, viz., Stage I, Stage II, Stage III, and Stage IV.

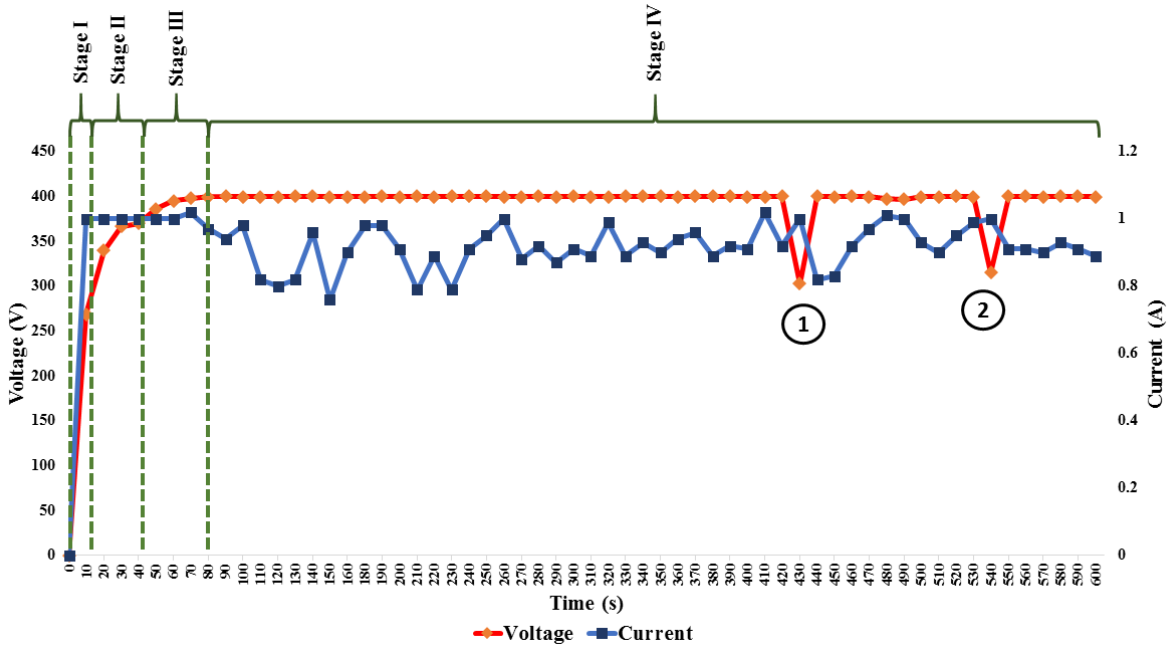

Figure 8. A real-time plot of voltage and current acquired for 10 minutes of treatment time.

Stage I is the onset of the process. The voltage and current escalate rapidly for 10s only, and this pattern coincides with the passive oxide film growth, known as anodic oxidation in the conventional electrochemical method [69]. The passive oxide film functions as a barrier layer between the metal substrate and electrolyte during the early stage of the process, as illustrated in Figure 9a.

Stage II is when the voltage transient begins to decline, but the current keeps linearly increasing until the end of this stage. The micro-arc sparks could be noticed to emerge across the substrate surface, during the process which suggests the breakdown of the passive oxide layer, during the process which suggests the breakdown of the passive oxide layer (Figure 9b) [70]. Furthermore, a higher voltage causes local heating at the substrate/electrolyte interface with high

temperature and pressure, and it eventually induces the melting of the substrate where the Ti, Al and V ions and electrons are ejected, as shown in Equation (1-3).

Stage III shows the current becoming constant, and the voltage change is much slower compared to Stage II. The coating grows thicker and augments the resistance of the PEO coating; thereby, it modifies the feature of the plasma and larger sparks could be observed during the process.

Stage IV is when the voltage reaches its threshold of 400 V, and the current begins to oscillate to find the stability of the circuit. The sparks become more powerful, which may cause thermal cracking. The instability at points 1 and 2 may be inferred as the crack formation and lead to disturbances in current flow through the coating. In addition, the emergence of the oscillating current may represent the stage of oxide breakdown and regrowth, which maintains the thickness of the layer since the voltage is limited to 400 V only.

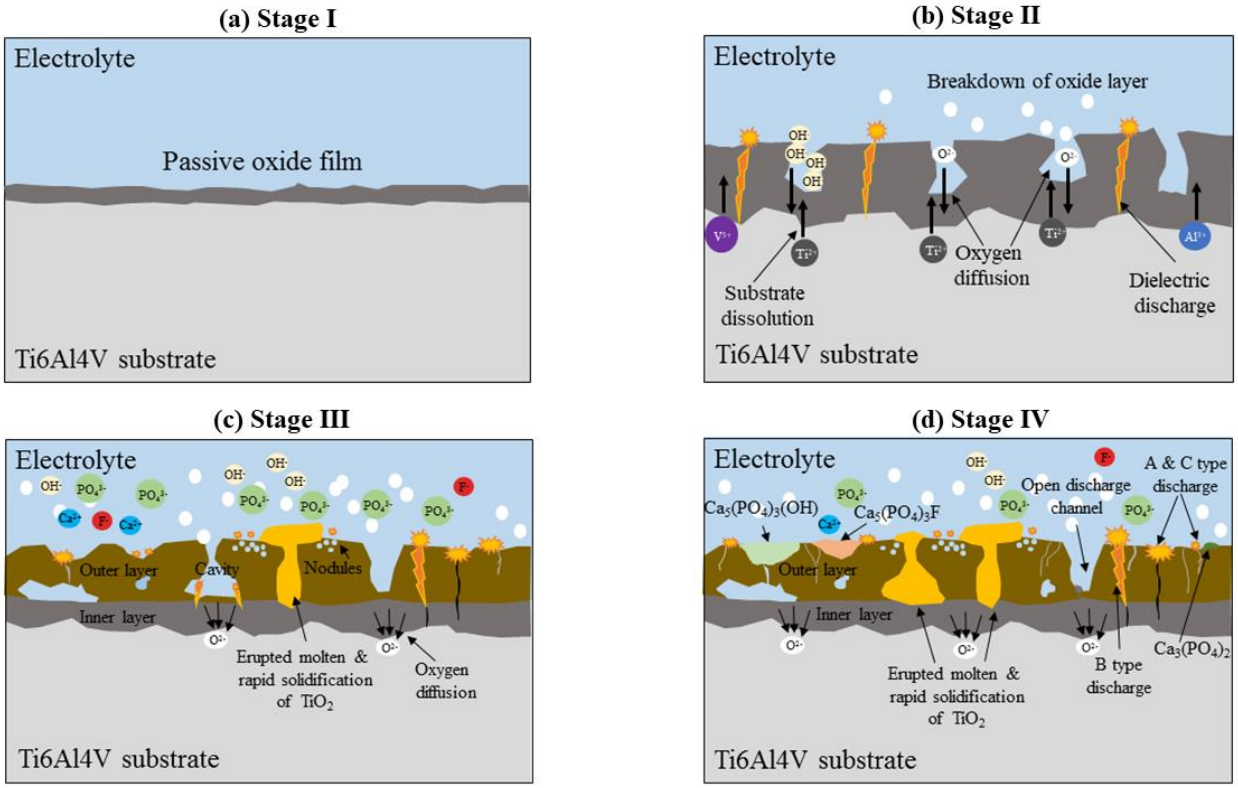

Figure 9. Schematic of the PEO process during four different stages (adapted from [70]).

3.3.2 THE PHASE COMPOSITION OF THE COATING AND THE MECHANISM OF GROWTH COATING

The element composition was probed on the coating surface and the Ca/P ratio was determined. The coating had a Ca/P ratio of 1.303 ± 0.01, which is lower than the ratio of stoichiometric HAp (1.67) [71]. The substrate melted and contributed to the formation of TiO_2. Thereby, Al and V could be discerned as well as they were a part of Ti alloy constituent, which dissolved together with Ti during the process. The presence of Ca, P, and F are related to the discharge on the coating surface as described in Figure 9c and 9d.

Figure 10 illustrates the XRD pattern of Ti6Al4V and the PEO coating, which exhibited seven distinct phase compositions, namely FAp, HAp, tricalcium phosphate, anatase, rutile,

aluminium oxide and vanadium (V) oxide which was obtained during the PEO process. XRD process was carried out to corroborate and to analyze the phases that were incorporated in the coating layer. As reported in a previous study by Laveissière et al. [72], all the compounds used in the electrolyte solution preparation would be involved in the process. However, the elements that do not play any key role to fulfil the purpose of the coating development were not analyzed. Anatase and rutile are two polymorphs from TiO_2 that have a tetragonal crystal structure and are favorable for bone implants, owing to their bioactivity and biocompatibility [53,56]. According to Hussein et al. [70], the coating layer growth mechanisms could always be classified into two different layers, inner layer (inward growth) and outer layer (outward growth). The dissolution of the Ti, Al and V from the substrate and oxygen diffusion produce TiO_2, Al_2O_3 and V_2O_5 in the inner layer.

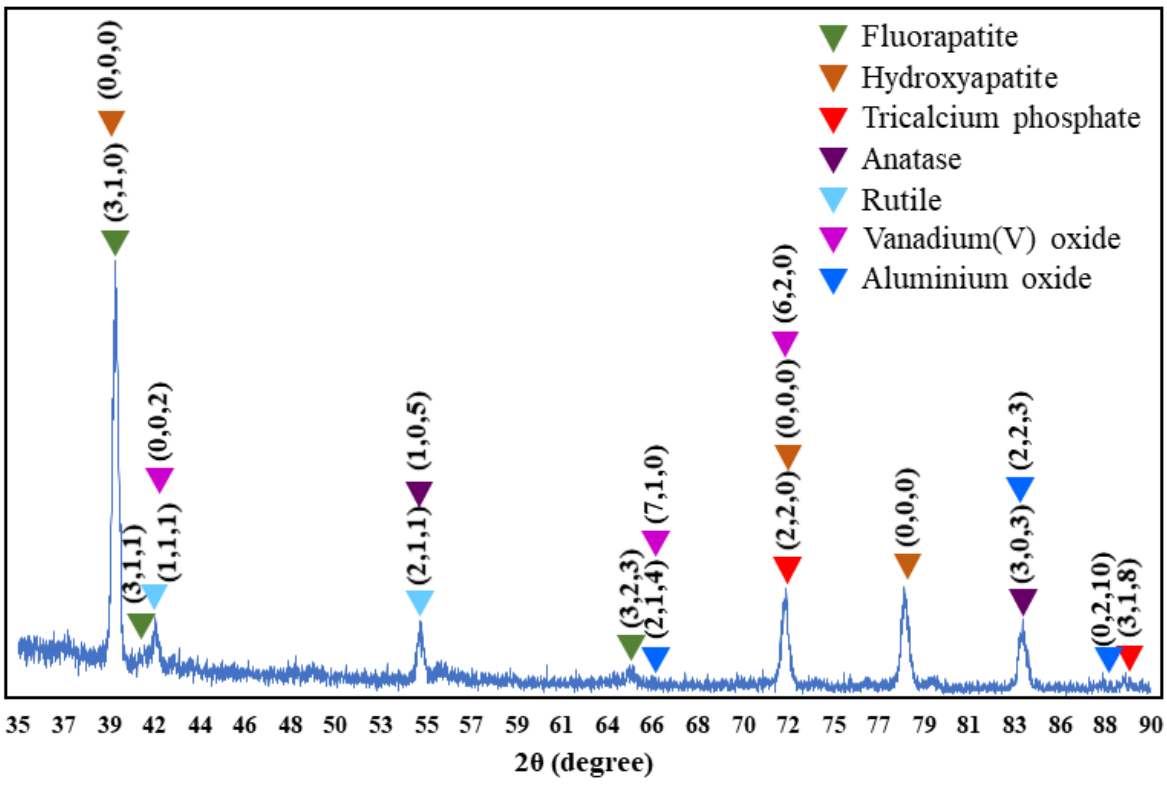

Figure 10. XRD pattern of different phase compositions on the coating surface layer.

A high voltage is one of the features of PEO process, and in most cases, the dissolution of the substrate occurs when the voltage passes the breakdown voltage, where it then instantaneously generates a micro-arc discharge and eventually induces the dissolution of the Ti, Al and V of the substrate (Equations (1–3)). Potassium hydroxide (KOH) is ionized to form hydroxyl ions (Equation (4)), which then evolve into gaseous O_2 (Equation (5)). The O_2 appears in either two forms; a gas or O^{2-} ions, which leads to the formation of TiO_2. Ti^{4+} would subsequently be attracted to O^{2-} (Equation (7)) and slightly react with OH^- (Equation (6)) resulting from the electrostatic attraction to form TiO_2. Likewise, Al_2O_3 and V_2O_5 were formed through the direct oxidation and dissolution of Al and V of the substrate. However, the substrate has a higher constituent of Ti compared to Al and V, thus, the coating layer is predominantly composed of TiO_2.

$$Ti \rightarrow Ti^{4+} + 4e^-, \quad (1)$$

$$Al \rightarrow Al^{3+} + 3e^- \quad (2)$$

$$V \rightarrow V^{5+} + 5e^- \quad (3)$$

$$KOH \rightarrow K^+ + OH^-, \quad (4)$$

$$4OH^- \rightarrow O_2 + 2H_2O + 4e^-, \quad (5)$$

$$Ti + 4OH^- \rightarrow TiO_2 + 2H_2O + 4e^-, \quad (6)$$

$$Ti^{4+} + 2O^{2-} \rightarrow TiO_2, \quad (7)$$

$$Al^{3+} + O^{2-} \rightarrow Al_2O_3 \quad (8)$$

$$2V^{5+} + 5O^{2-} \rightarrow V_2O_5 \quad (9)$$

In addition, the thickening of the coating was due to the ejection of the oxidized molten Ti through the discharge channels to the surface. The erupted molten TiO_2, as interpreted in Figure

9c, rapidly cooled down and solidified at the coating/electrolyte interface [73,74]. As described by Hussein et al. [70], discharge cavities repeatedly occur throughout the process, allowing the molten oxidized Ti to pass through the channels and solidify on the surface. As a matter of fact, this phenomenon is committed to the growth of the outer layer.

Ionization of the electrolyte causes the compounds calcium fluoride and tricalcium phosphate to ionize into ions such as Ca^{2+}, HPO_4^{2-} or PO_4^{3-}, OH^-, and F^-, which form a sea of ions in the electrolyte solution. These ions then incorporate into the TiO_2 layer and TiO_2, assisting the nucleation and crystallization of HAp, tricalcium phosphate, and FAp by micro-discharges on the coating surface, as depicted in Figure 9d. Moreover, electrical attraction during the process draws fluorine and phosphorus anions to the substrate and contributes to the formation of HAp and FAp [66]. The equations of the reactions are as below:

$$3Ca^{2+} + 2PO_4^{3-} \rightarrow Ca_3(PO_4)_2 \quad (10)$$

$$5Ca^{2+} + 3PO_4^{3-} + OH^- \rightarrow Ca_5(PO_4)_3(OH) \quad (11)$$

$$5Ca^{2+} + 3PO_4^{3-} + F^- \rightarrow Ca_5(PO_4)_3F \quad (12)$$

Hence, an outer layer at the coating surface/electrolyte interface was formed by micro-discharge and the emission of molten Ti to the surface, which eventually oxidized and solidified.

3.3.3 SURFACE AND CROSS-SECTION MORPHOLOGIES

SEM images of the surface morphologies of the PEO coating produced from the phosphate–alkaline electrolyte are presented in Figure 11a. The coating surface was overlaid with irregular micropores of different sizes and dominated by crimped shape pores. As shown in Figure 11d, the size of the micropores was in the range of 0.158 μm^2 to 34.013 μm^2 (surface characteristics

of the coating can be found in Table 2), and these pores may promote cell adhesion to the coating surface [75]. Sowa et al. [76] investigated the bioactivity of a coating containing Ca and P on a Ti alloy substrate, where the mesenchymal stem cells proliferated into the osteoblast cell with regards to the nature of Ca and P as natural bone elements. On top of that, the cells were well spread on the coating surface as they responded to the pores that formed on the PEO coating, which looked like the structure of porous bone. In fact, the biological response of the cell depends on surface features such as the chemical composition and surface topography [77–82]. Therefore, the micropore features developed by the PEO technique would enhance the proliferation and differentiation of cells [82]. The micropores could be interpreted from the release of gaseous oxygen and tracks of the micro-arc discharge channels. During the process, Ti ions from the substrate were dissolved and ousted through the discharge channels to the coating/electrolyte interface; meanwhile, oxygen ions diffused into the coating layer, which contributed to the formation of TiO_2. In short, the rapid solidification of the Ti oxide occurred, thereby sintering and accumulating on the coating surface, which eventually contributed to the growth of the coating.

Owing to the rising local temperature on the substrate and the electrolyte temperature that was kept as low as possible during the process, the molten Ti oxide promptly solidified and induced thermal stress and residual stress. The evidence points to the likelihood that, in most cases, these may contribute to the formation of cracks on the coating surface, as illustrated in Figure 12.

The presence of crooked lines at the coating/substrate interface resulted from the dissolution of the substrate in the early stage of the PEO process [83]. A typical PEO coating always comprises two particular layers (as mentioned before), namely the inner layer and outer layer where inhomogeneous pores and defects are spread on both layers. The inner layer is well adhered to, less perforated, and has better mechanical properties compared to the outer layer. Then,

the extent of connected porosity can be observed at the cross-section, as shown in Figure 13 a,b. The total thickness of the coating surface varied in the range of 5–9 µm. The thickness of the coating was measured at ten distinct points, and the average coating thickness was calculated from those points; thereby, the average coating thickness was 7.89 µm with a standard deviation of 0.46. It appears that the cracks on the outer layer may be associated with the grinding process of the cross-section sample for SEM analysis and proving that the outer layer is flimsy and not dense. According to the Pilling–Bedworth ratio (P–B ratio), titanium's P–B ratio is approximately 1.73, where the underlying metal is protected against further oxidation or corrosion by the passivated oxide coating; Figure 13b shows the contrary—there were open micropores on the coating layer. Repeated melting, melt-flow, and the re-solidification of the oxide coating from the plasma discharges and large sparks probably caused the formation of these open micropores. Despite these microstructures, corrosion might not happen due to titanium's outstanding resistance to corrosion properties.

It was found from cross-sectional SEM images and accompanying EDS maps (Figure 14) that Ti, Ca, P, and F spread over the surface layer of the sample, while Al and V elements came from the dissolution of the substrate. V can scarcely be found compared to Ti and Al due to lower composition in the substrate. The distribution of chemical elements confirmed that the compounds dissolved in the electrolyte play an important role during the PEO process, according to the ratio of compounds used during the preparation of the electrolyte solution. Oxygen typically can be identified covering up the coating layer, ascribed to the oxidation during the process, which eventually nurtured the nucleation and adsorption of HAp and FAp on the outer layer of the coating. Because calcium was entangled along the coating surface, tricalcium phosphate, HAp, and FAp could be found on the outer layer only. The power supply for PEO treatment plays a vital role in

the resulting coating characteristics. DC power supply introduced positive bias where it would diminish the ability to attract positively charged ions to the surface by electrostatic forces. Therefore, the Ca incorporation in Figure 14 appears deficient, thus the condition was unconducive for the nucleation of HAp and FAp onto the surface coating during the treatment.

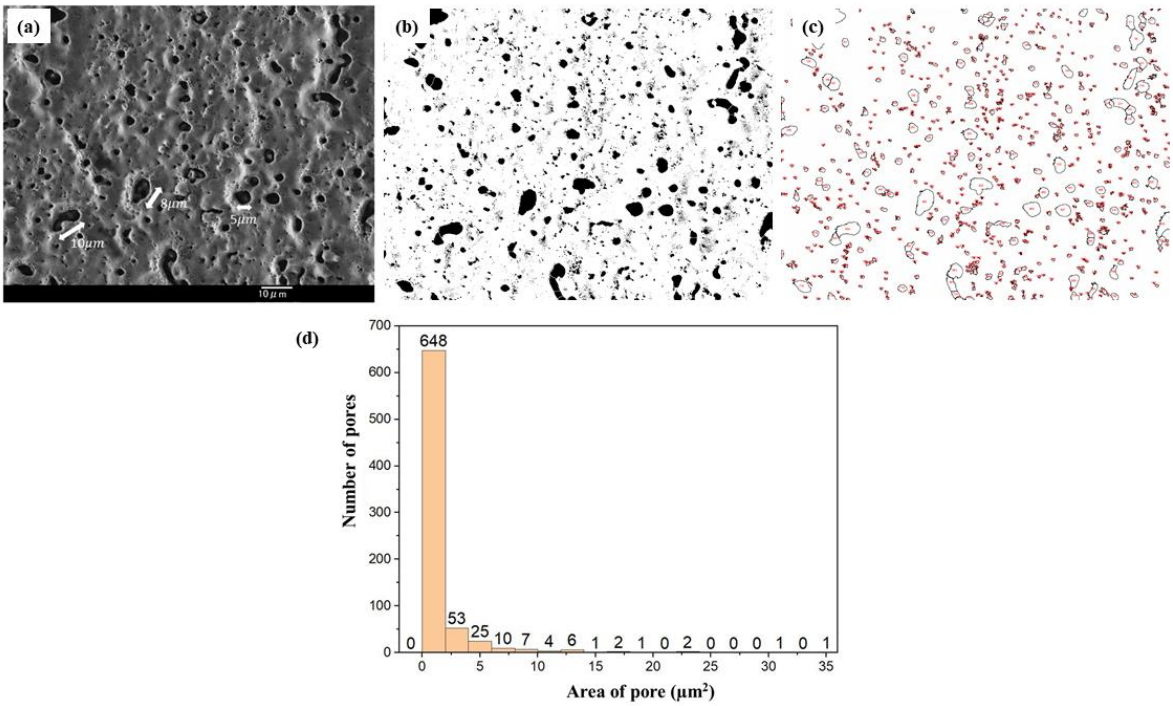

Figure 11. Image analysis to measure the population density of pores; (a) original image; (b) thresholded image; (c) segmentation after using built-in Analyze Particles Image J plugin; (d) histogram of pores distribution.

Table 2. Surface characteristics of the coatings.

Properties of the coating	**Quantity**
Population density of pores (pores/mm^2)	760,423.599
Pore size (μm^2) Min. Max.	 0.158 34.013
Average size (μm^2)	1.315
Standard deviation	2.952

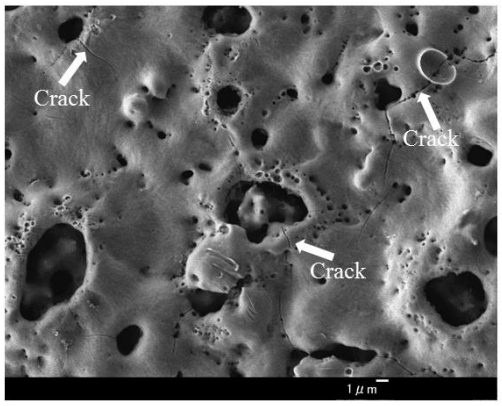

Figure 12. Crack formation around the pores on the coating surface.

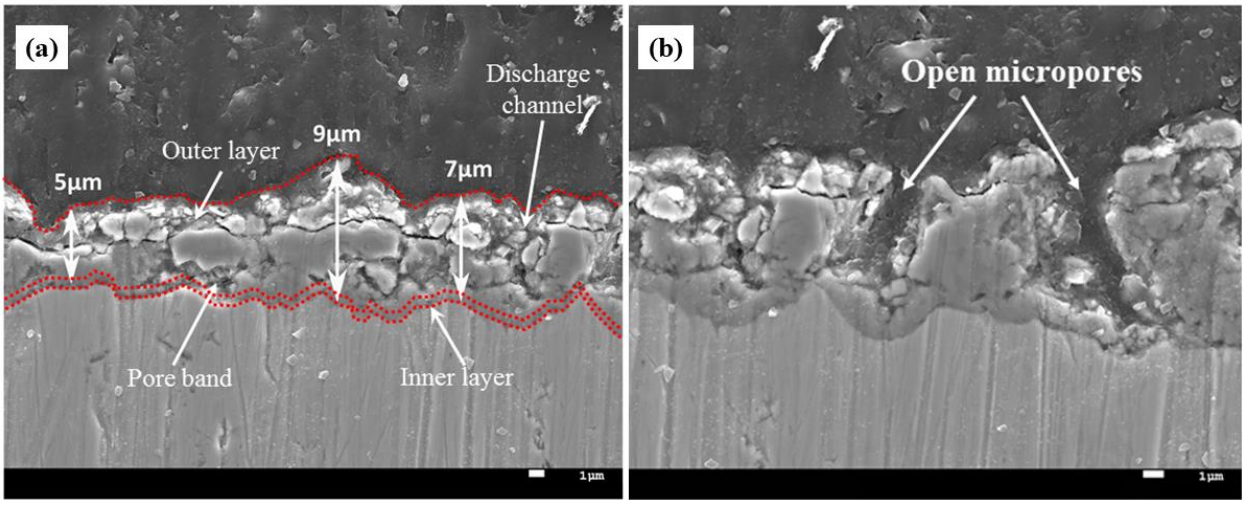

Figure 13. The cross-section morphology with: (a) two typical layers: inner layer and outer layer; (b) the open micro-discharge channels developed in the cooling layer.

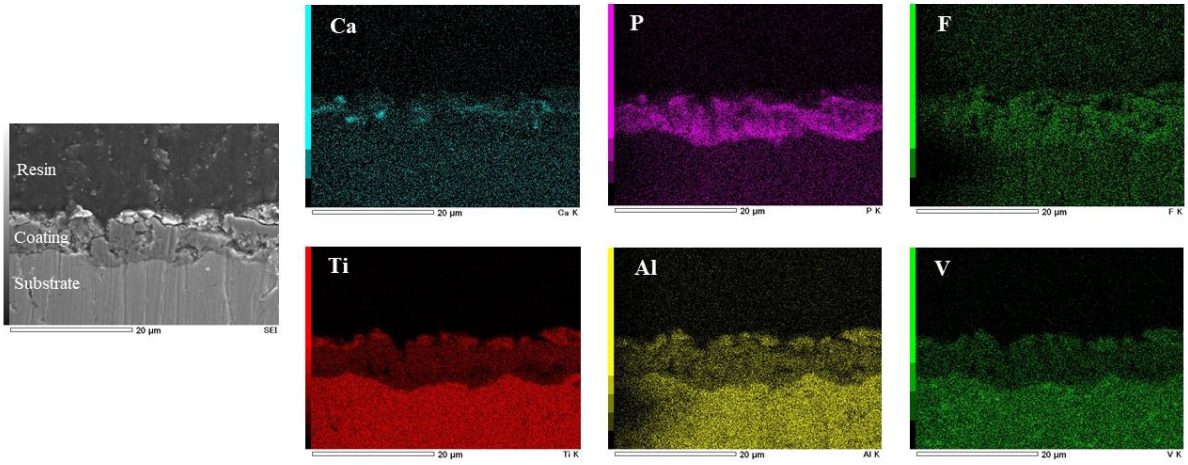

Figure 14. Cross-section EDS maps of the coating with different chemical elements namely, P, F, O, Ca, Al and V.

3.3.4 MICRO-SCRATCH TEST

The micro-scratch test was carried out to assess the adhesive strength of the coating layer on the Ti6Al4V substrate. This test was extensively used in the coating industry and coating research laboratories to assess the tribological properties of coatings [84]. HAp and FAp were

ceramic coatings that were considered brittle, especially in bulk form, and yet it is somehow proven they were indemnified of this limitation when they were deposited as a coating. Thus, it is substantial to understand its mechanical behaviors and its failure modes with crack patterns when stresses are applied to the coating.

During the micro-scratch test, a progressive normal load was applied through a diamond indenter on the coating surface from left to right, as shown in Figure 15. The key transition points of the coating failure mechanisms are determined by a critical load, and these were confirmed by microscopy.

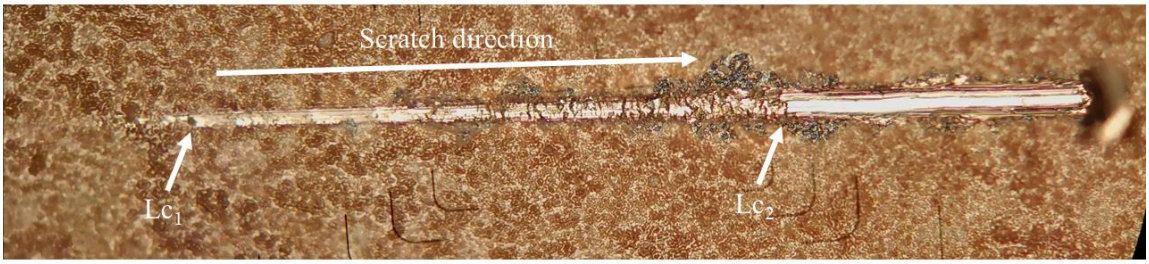

Figure 15. Scratch direction acquired by optical microscope.

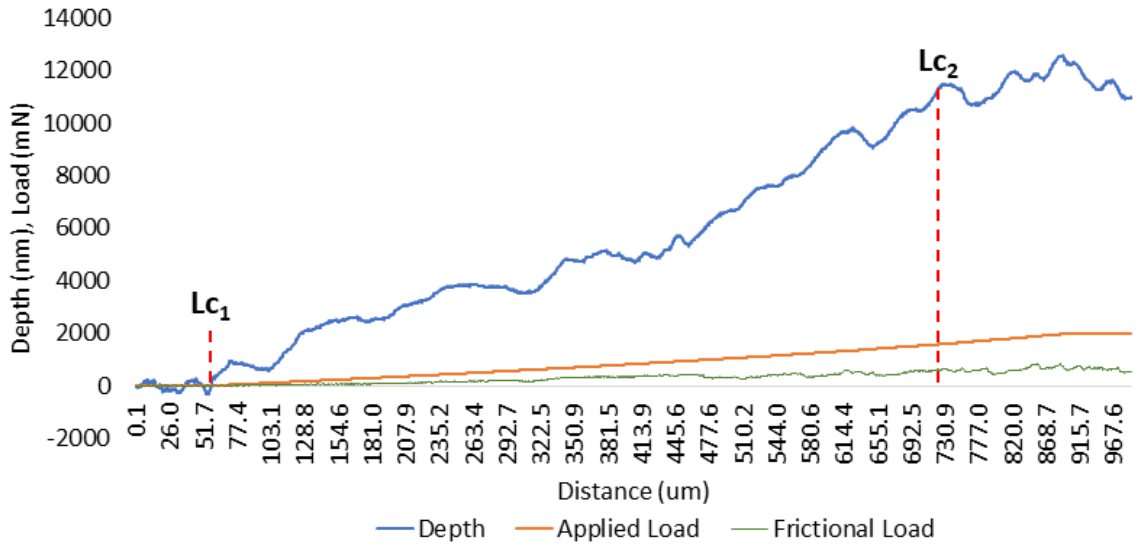

Figure 16**.** The scratch distance, indentation depth, applied load, and frictional load plot of the micro-scratch test.

The coating started to indicate traces of failure when the diamond indenter was pulled over the surface of the coating. Coating failure can be determined with critical loads, and in this study, Lc_1 and Lc_2 were the two values generally depicting the different degrees of failure. The failure commenced with the plastic deformation where no spallation of the coating with minor cracks could be found. In this study, Lc_1 was designated as the onset of delamination or major cracks, where transverse, semi-circular chips on the trackside were observed after this point. The indenter penetrated more into the coating, which generated mild tensile cracking, and the indenter tip applied stress on the coating, where stress on the coating was relieved by delamination on the trackside. The Lc_2 was recorded when the coating broke through the scratch path and uncovered the substrate as a result of the induction of an adequate normal load and penetration depth of the indenter into the coating layer. The critical loads were quantified in accordance with the scratch

profile of the load-displacement plot, and the scratch image was obtained from an optical microscope, as shown in Figures 15 and 16. The Lc_2 happened approximately at the scratch length of 717.13 μm with a critical load of 1553.38 mN, a depth of 522.56 nm, and a frictional load of 577.91 mN. This indicated that the diamond touched the substrate surface. This result is comparable with previous work by Adeleke et al. [54].

3.4 SUMMARY

The chemical element constituents from the species contained in the electrolyte solution were successfully incorporated into the coating layer. The TiO_2 coating layer promotes the nucleation and formation of tricalcium phosphate, HAp, and FAp, and this was assisted by plasma discharges that happened during the process. The presence of HAp and FAp in the coating layer could contribute to the bioactivity and antibacterial properties of the TiO_2–PEO coating layer. The irregular micropores, with sizes approximately up to 34.013 μm^2 on the coating surface, are the traces of discharges that may offer a better proliferation of osteoblast cells on the coating. However, the bioactivity test of the actual osteoblast cells' response to these PEO-treated coatings will require specific investigations in a further step of the work. Overall, the PEO HAp-FAp coating exhibited the potential to overcome the deficits of titanium alloys and supported the application of the coating for orthopedic implants. Future work shall investigate the optimal amount of fluoride in the coating layer that obtains excellent results without causing adverse effects in adjacent tissue.

CHAPTER 4: COATING CHARACTERISTICS AND MECHANICAL PROPERTIES OF PEO-TREATED SELECTIVE LASER MELTED POROUS SCAFFOLD

4.1 INTRODUCTION

Conventional techniques to generate porous metallic structure such as plasma spraying, space holder method, powder sintering approach, combustion synthesis, and polymeric sponge replication, have shown that they have poor control over pore architecture and implants design. Additive manufacturing (AM) has been an advanced innovation in recent days that enables the fabrication of lighter, stronger and complex structures. Metal AM, namely SLM and EBM has enabled the manufacturing of regular porous metallic structures, complex geometries and lightweight 3D components. In addition to the capability to produce complex geometries, AM could fabricate implant design with precisely control the distribution of mechanical and physical properties which is favorable for improving the lifespan of bone-mimicking porous biomaterials. Titanium and its alloys are known as a bioinert and hydrophobic material, which could hinder cell attachment and cause additively manufactured porous scaffold remains dormant. One may hence require implementing bio-functionalization techniques to introduce preferable surface chemistry and nano topography to enhance cell attachment, prompt bioactivity on the surface of porous titanium and improve the osseointegration of 3D printed porous scaffold after the implantation. These approaches are to fulfill twofold most important aspects of metallic implants; reduce stress shielding of metal implants and promote osseointegration by contact bone in-growth.

Contrary to the solid implants, surface treatments of additively manufactured porous metals have several vitally important issues to be tackled. The first, the anchorage of endosseous implants, where Oshorn and Newesley (1980s) proposed two mechanisms of integration namely contact osteogenesis and distance osteogenesis. Contact osteogenesis is bone formation that takes place

from the implant to the adjacent tissues, in which the implant surface acts as a site of bone proliferation. Distance osteogenesis in contrast is bone formation from the host bones to the implant surface. In addition, contact osteogenesis is 30% quicker than distance osteogenesis and it is favorable to possess contact osteogenesis for the porous implant. This concept has not been yet applied for porous metal, but from the literature review, it could be deduced that bone in-growth at the as-manufactured porous titanium demonstrates a pattern of distance osteogenesis where bone tissues grow from the periphery toward the middle part of the scaffold. The second, bone remodeling due to the stress shielding caused by the scaffold itself. Contrary to contact osteogenesis, bone formation takes place on the surface of bone enclose at the implant site, thus exhibits the absence of direct bone contact with the implant surface. Consequently, the bone would remodel in response to the lack of load distribution from the scaffold to the bones within it. Surface treatment would be a choice of a solution on the ground of optimizing the patterns of bone in-growth within the scaffold.

In a study by Karaji et al., they developed additively manufactured Ti6Al4V based on the cubic unit cell coated with bio-functional PEO coating. The purpose of the study is to study the effect of PEO on mechanical properties on the additively manufactured scaffold. Thus, two different treatment times were applied on scaffolds with four different values of relative density and the effects of the PEO were analyzed by SEM, EDS, optical microscopy as well as static and dynamic (fatigue) mechanical testing under compression. The thickness form on the surface increase as the oxidation time increase based on SEM images. PEO treatment hardly affects most of the mechanical properties such as maximum stress, yield stress, plateau stress, and energy absorption. However, PEO treatment did influence the elastic modulus change significantly and

the scaffolds did not fail after putting under fatigue loading with 10^6 loading cycles at 70% of their yield stress.

3D printed porous Ti6Al4V coated with a homogeneous layer of microporous TiO_2 and amorphous calcium-phosphate produced with one step micro-arc oxidation or PEO described by Xiu et al. In vivo test in a rabbit model was conducted on the untreated and treated scaffold. Bone formation was observed only at the periphery of the scaffold for untreated scaffold with the pattern of distance osteogenesis. Unlike the untreated scaffold, the MAO-treated scaffold allowed contact osteogenesis where bone formed in situ and encircled the scaffold. The results suggest that contact osteogenesis could promote bone in-growth in and around the scaffold subsequently undermine bone remodeling. In addition, microporous topographies enhance bone tissue adhesion on the surface and generate a more robust bone/implant interface. Then, a push-out test was conducted to investigate the osseointegration strength between bone tissues and implants. In short, MAO improves bioactivity of the implant surface, enhances the osteointegration strength and bone/implant interlocking with contact osteogenesis.

In order to reinforce the osseointegration with the adjacent tissue after the surgery, the porous scaffold is coated with fluoridated calcium phosphate by using PEO technique. Ti6Al4V has been the material of choice for medical application and it is viable for SLM technology and PEO technique. The aims of this study are to investigate the PEO coating morphology formed on the surface of porous scaffolds and to determine the effect of PEO treatment on the compressive fracture behavior of fluoridated calcium phosphate coated lattice scaffolds. This chapter will discuss the coating morphology, the chemical/compounds contents in the coating layer, the compressive properties of as-built and coated porous scaffolds with the following parameters; plateau stress, quasi-elastic gradient, compressive offset stress and energy absorption rate.

4.2 MATERIALS AND METHODS

4.2.1 POROUS SCAFFOLD FABRICATION

There are three different processes involved for porous scaffold fabrication namely, pre-processing, build-up process and postprocessing (Figure 17). Before starting the build-up process, the porous scaffolds are designed in nTopology software, create STL files and transfer to the SLM 280HL machine at Contraves, Malaysia (Figure 18). Table 3 briefly demonstrates the technical specifications of the machine. Then, a batch of scaffolds is fabricated layer-by-layer by completely melting the Ti6Al4V powder and manufactured the scaffolds on the metal platform. System operated in an overpressure argon environment with processing chamber oxygen level below 0.2%. The fabrication process parameters are shown in Figure 19 and Table 4. Figure 20 shows the process of taking out the scaffolds from the chamber. Two different dimensions were fabricated according to the use of the scaffolds for the designated test with two different batches of fabrication. All scaffolds are cylinders with a porous structure with a similar strut diameter (0.3mm) but two different porosity (51.86% and 56.24%) designated as S_2mm and S_3mm (Figure 21). First batch fabrication of scaffolds was applied to heat treatment prior to removal of scaffolds from the platform while second batch fabrication of scaffolds was directly removed from the platform. Finally, the scaffolds are removed from the platform by using a cutting machine with a diamond blade.

Pre-processing

Design porous part in **nTopology** software, arrange the layout of parts on the platform and create stl file for the machine.

Production

SLM process, the main process to obtain the part (took 6 hours)

Postprocessing

Heat treatment, remove the parts from the platform, grind and clean the parts with acetone, ethanol and distilled water

Figure 17. Three different stages of porous scaffold fabrication process.

Figure 18. SLM 280 HL at Contraves, Malaysia.

Table 3. Technical specifications of SLM 280 HL.

Build envelope (L x W x H)	280mm x 280mm x 365mm
Laser beam	400W
Build rate	Up to 55cm^3/h
Layer thickness	20µm - 75µm
Min. feature size	150µm
Beam focus diameter	80µm - 115µm
Max. scan speed	10m/s

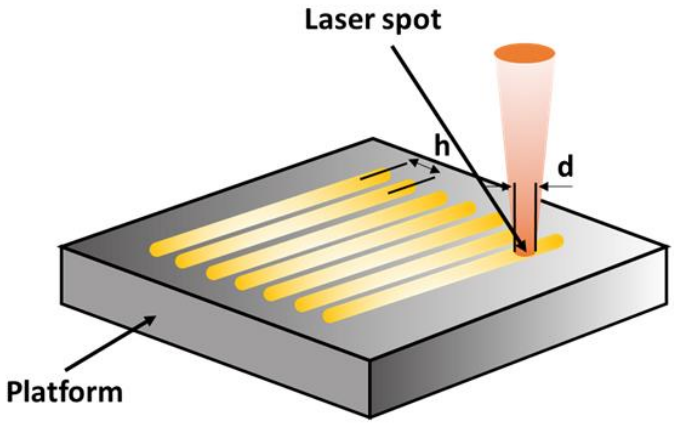

Figure 19. SLM process parameters.

Table 4. Parameters are set during the fabrication process.

Laser power (Watt)	200
Laser spot diameter, d (µm)	100
Hatching distance, h (µm)	80
Scan speed (mm/s)	1300

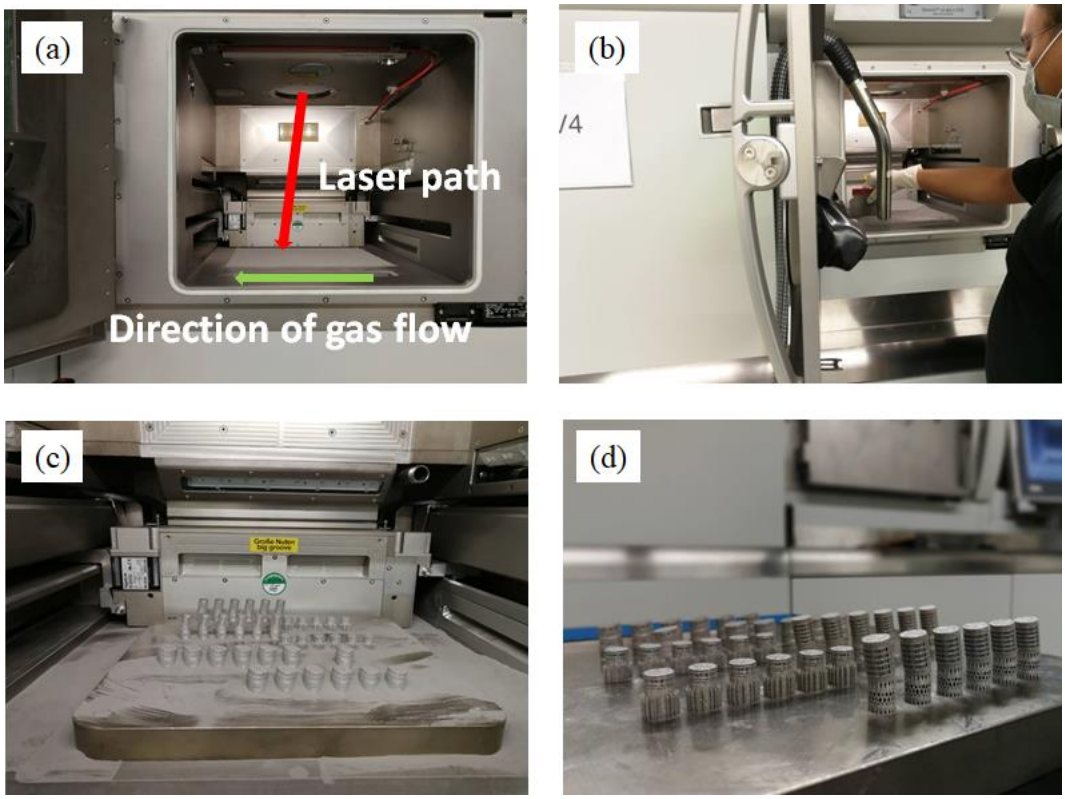

Figure 20. The scaffolds were taken out from the work chamber; (a) real machines work chamber, (b) the technician was cleaning the unmelted powder, (c) the scaffolds built on the platform while still in the work chamber, and (d) the scaffolds before post-processing stage.

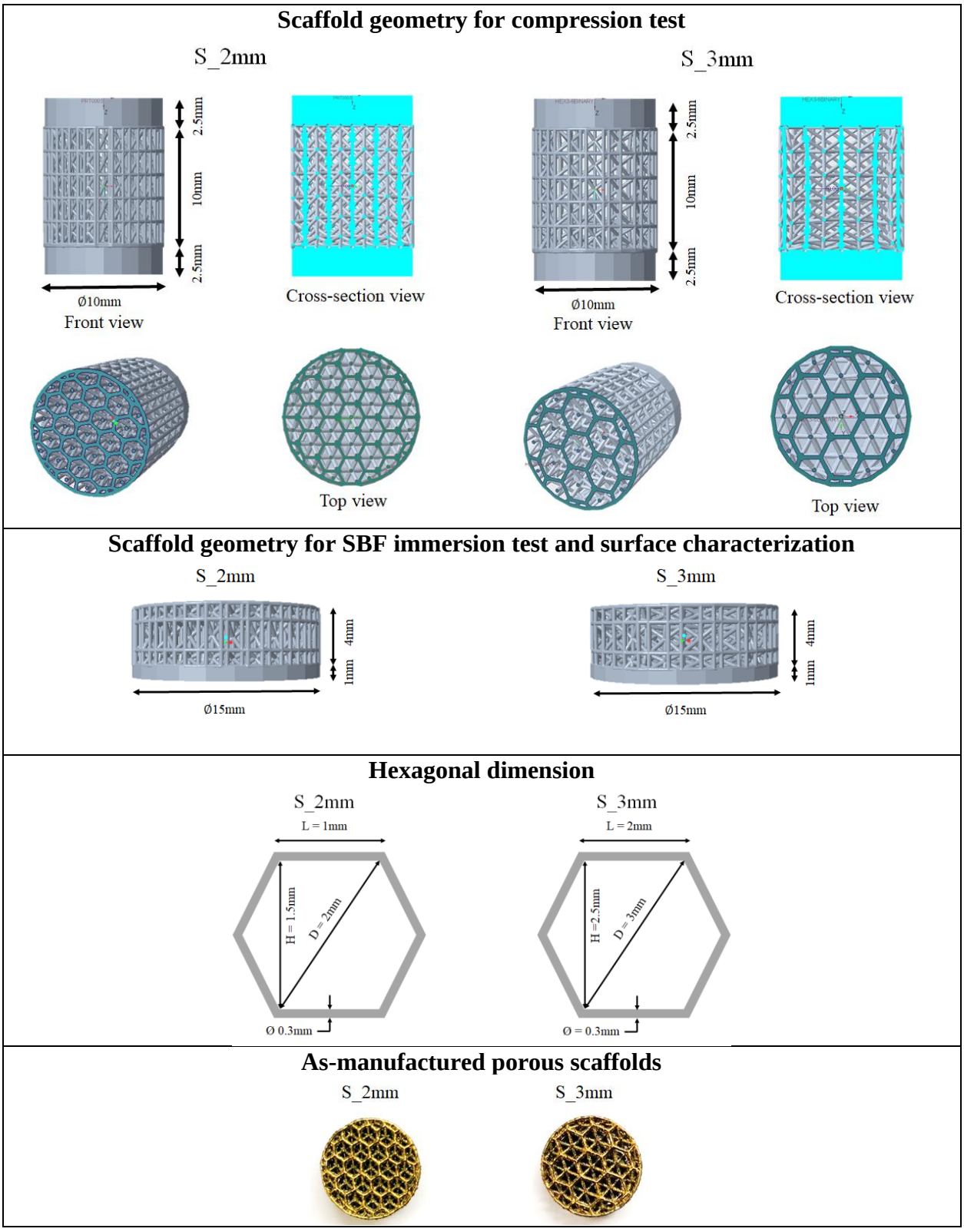

Figure 21. Dimensions of porous scaffolds.

4.2.2 PEO TREATMENT SETUP

The similar PEO setup (showed and explained in 3.2.2) was used but different parameters was set as shown in Table 5. The parameters that had been used for Ti6Al4V plate substrate did not work for porous scaffold substrate due to different geometry of substrate would effect the electric conductivity of PEO process.

Table 5. Scaffolds with different treatment time and scaffolds labeling (S_D_PEO treatment time).

	Voltage threshold (V)	**Maximum current applied (A)**	**PEO treatment time (min)**
S_2mm 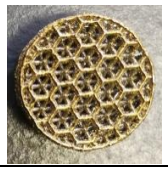	-	-	-
S_2mm_5mins 	400	7	5
S_2mm_7mins 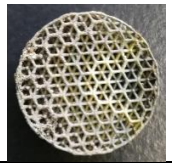	350	7	7
S_3mm 	-	-	-

Table 5. Scaffolds with different treatment time and scaffolds labeling (S_D_PEO treatment time) (Continued).

S_3mm_5mins 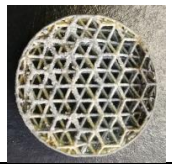	400	7	5
S_3mm_7mins 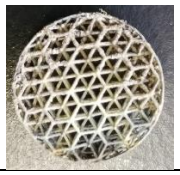	350	7	7

4.2.3 COATING CHARACTERIZATION

Similar FESEM-EDS, XRD and ImageJ software that were used to characterizing the PEO coating on Ti6Al4V plate in Chapter 3 were used to investigate the coating characteristic formed on the porous scaffolds. The details have been described in section 3.2.3.1 and 3.2.3.2.

4.2.3.1 XPS ANALYSIS

XPS analysis was carried out on JEOL JPS-9010MC (JEOL, Japan) attached with 10 kV and 10 mA X-ray gun using monochromatic Al Ka radiation (Figure 22). Wide scan and narrow scan were conducted. The pass energy was 20 eV at the region measurement. The following core levels were analyzed: C 1s, Ca 2p 3/2, P2p 3/2, F 1s, Ti 2p 3/2, and O 1s. By determination of the binding energy on these states, the present chemical bonds have been accurately determined. Quantification of the spectra was performed with SpecSurf version 4.10 software (JEOL, Japan). The applied binding energy database NIST X-ray Photoelectron Spectroscopy Database.

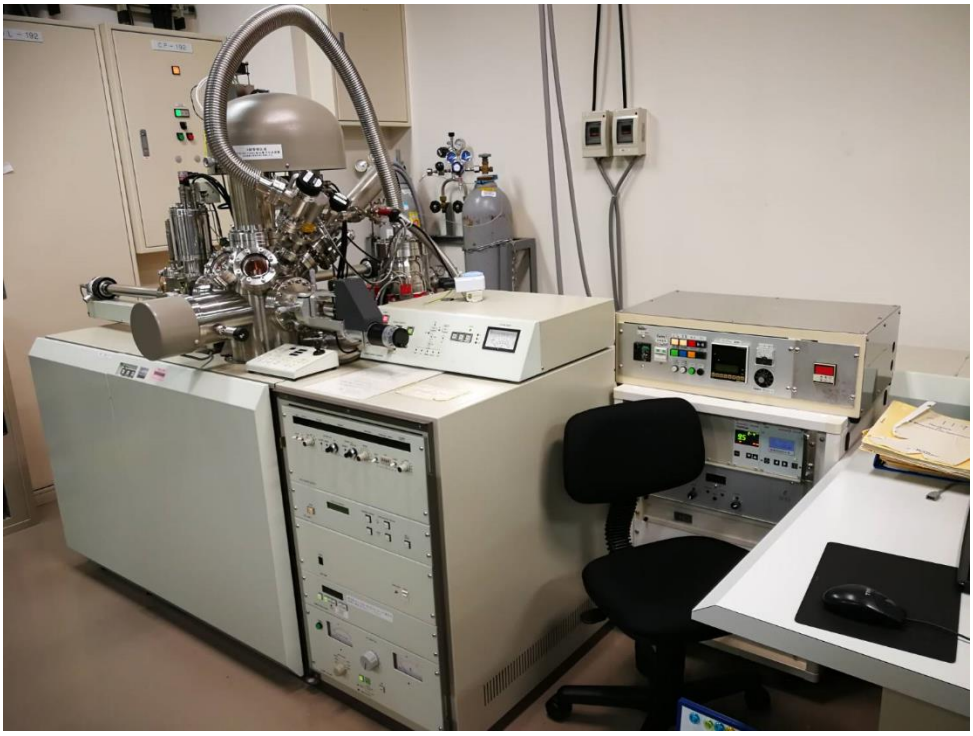

Figure 22. XPS machine at CRIS, Hokkaido University.

4.2.4 COMPRESSION TEST

Universal material testing machine Autograph AG250kND (Shimadzu Corporation, Kyoto, Japan) located at Hokkaido Research Organization is used for the compression test of the uncoated and coated porous scaffolds (Figure 23). The compression test is carried out according to the ISO standard 13314:2011. Cylindrical porous scaffolds with a length of 10mm attaching to 2.5mm length of the bulk plate at the bottom and on the top and diameters of 10mm as shown in Figure 21 were used for the test. The camera was set up to record the fracture behavior of the scaffolds throughout the process. The testing condition can be referred to in Table 6.

Table 6. A testing condition set according to ISO 13314:2011.

Crosshead speed	1mm/min
Strain rate	10^{-3}/s
Test force	200kN
Data sampling frequency	50Hz
Crosshead displacement limit	10 mm for scaffolds without heat treatment and 7 mm for scaffolds with heat treatment

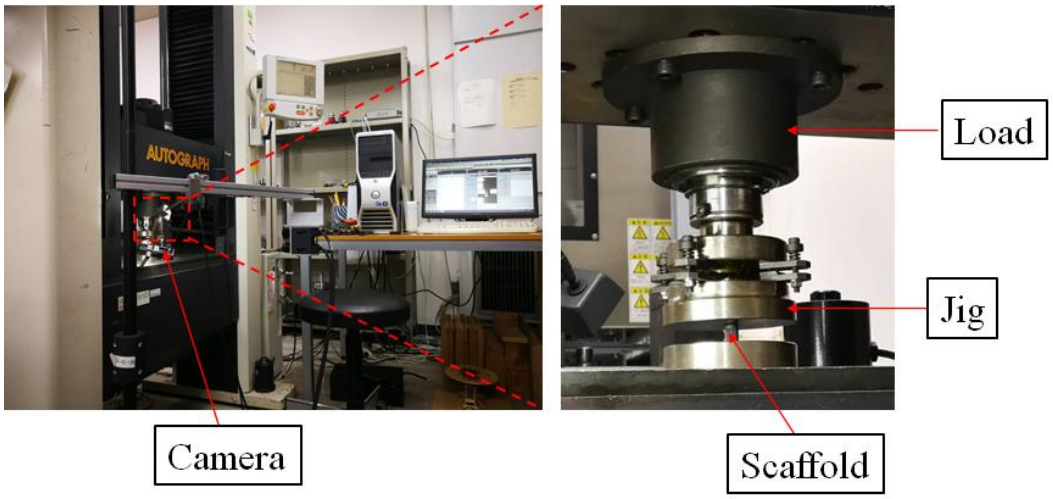

Figure 23. Universal material testing machine Autograph AG250kND.

4.3 RESULTS AND DISCUSSION

4.3.1 ELECTRICAL RESPONSES

Figure 24 reveals the current response to the voltage sweep of the SLM-manufactured porous Ti6Al4V porous scaffolds with two different porosity percentage and treatment time. The plots also could be divided into four stages based on the consistent pattern of the current and voltage shift demonstrated in Figure 24 a, b, c, and d. The curves pattern could be attributed to the kinetics of electrochemical processes that occur at the surface of the anode within the electrolyte as has been explained in section 3.3.1 and 3.3.2.

The current-voltage behavior in Stage I and II showed features consistent with Ti6Al4V plate substrate. In Stage I, the voltage and current linearly increase with time where the current appears to locate a maximum value of 7 A for all different substrates while voltage was detected at a different value in the range of 150 to 270 V. The voltage and current linear rise appear within less than 20s to be a result of oxide formation similar as indicated in 3.3.1 for Ti6Al4V plate substrate. Habazaki et al [85] and Teh et al [86] suggested that anodic oxidation taking place at around 20 to 50 V correlate to oxygen generation during amorphous to crystalline transition in the passive oxide film during anodizing of titanium alloy plate substrate. In our study, the anodization occurs at a higher voltage and it may be related to the pH level of electrolyte and element species contain in an electrolyte. According to a study by Neupane et al [87], the increase of the electrolyte pH would lead to more powerful reactions at the anode surface. These results comply with the striking increase of current and voltage in this stage.

A plateau region of current in Stage II can be observed for all substrates with different duration (40s for S_2mm_5mins, 20s for S_2mm_7mins, 70s for S_3mm_5mins and 40s for

S_3mm_7mins) while voltage transient begins to decline up to the plateau region in Stage III. Stage II is defined as the region in which the breakdown of the passive layer would occur and the migration of species from Ti6Al4V outward and oxygen species inward similar to Ti6Al4V plate substrate.

In Stage III, the current-voltage behavior is different compared to Ti6Al4V plate substrate. The current value drops before showing a disturbance in Stage IV and voltage linearly increases again to the maximum threshold. The phenomenon occurs in 10s for all substrates.

The voltage reaches its threshold in Stage IV and the current begins to oscillate. It can be assumed that the breakdown of the oxide layer and regrowth as described in 3.3.1 and 3.3.2. It is interesting to observe the curve pattern may change according to the different geometry of the substrate and the significant influence of the geometry of the substrate on the PEO process.

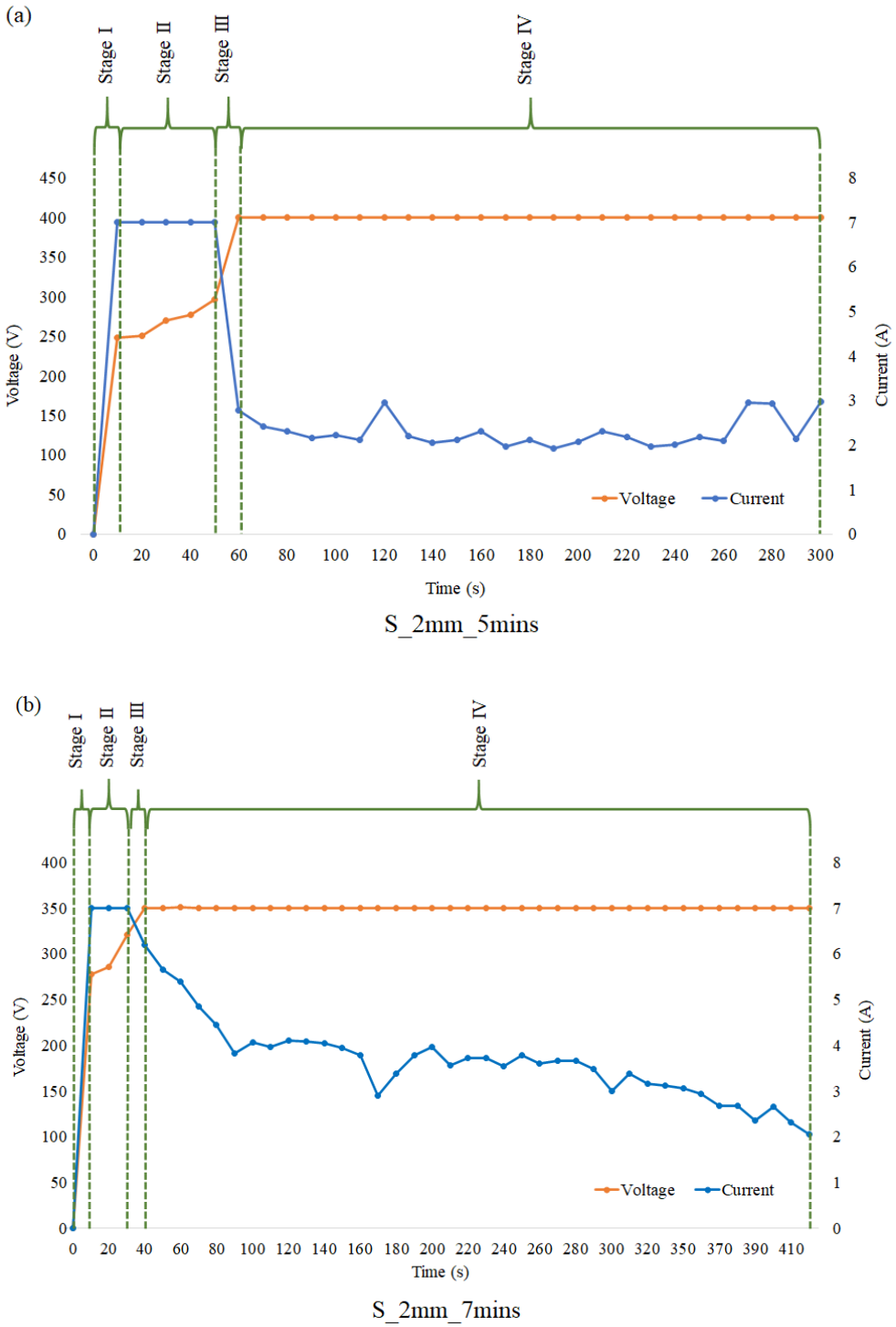

Figure 24. A real-time plot of the voltage and current obtained for two different PEO treatment time (5 minutes and 7 minutes) for porous scaffolds namely, (a) S_2mm_5mins, (b) S_2mm_7mins, (c) S_3mm_5mins and (d) S_3mm_7mins (Continue on next page).

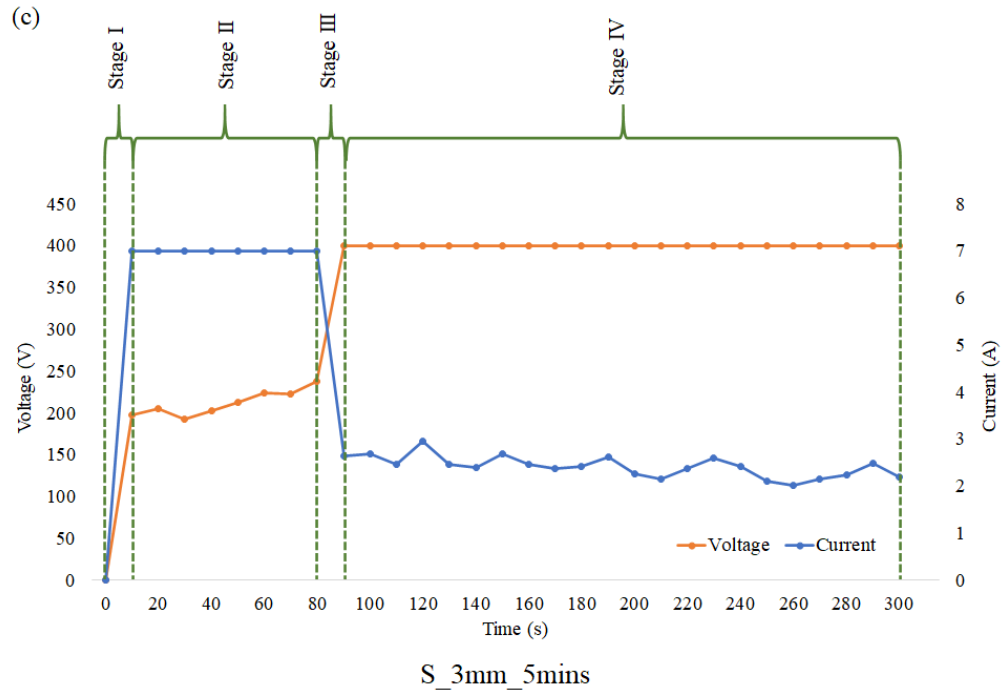

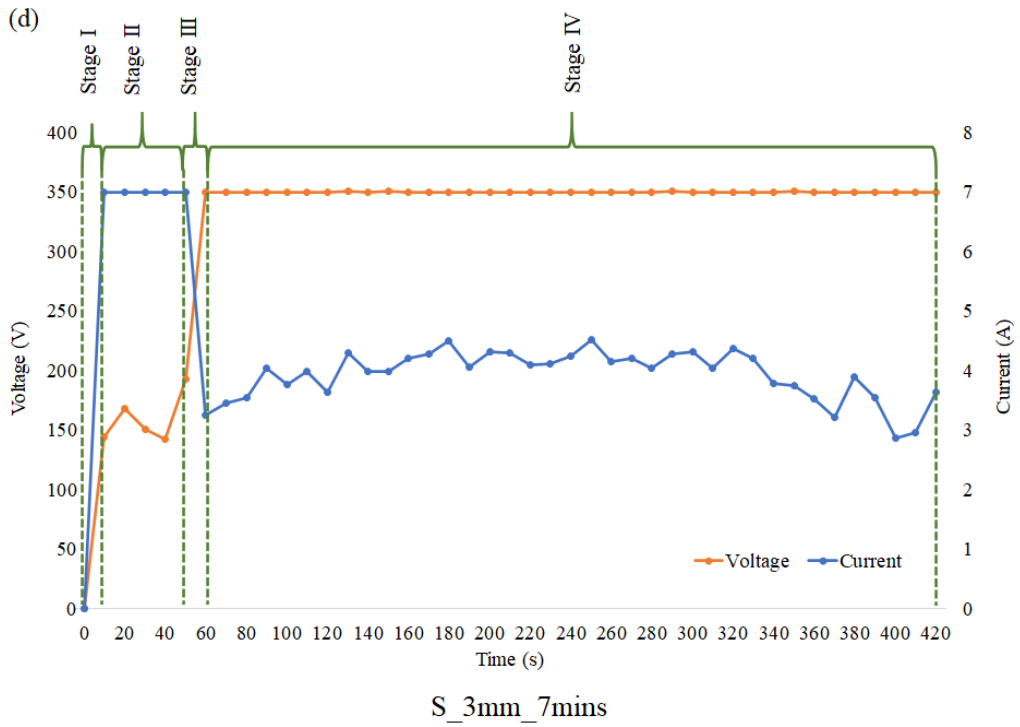

Figure 24. A real-time plot of the voltage and current obtained for two different PEO treatment time (5 minutes and 7 minutes) for porous scaffolds namely, (a) S_2mm_5mins, (b) S_2mm_7mins, (c) S_3mm_5mins and (d) S_3mm_7mins.

4.3.2 COATING DEPOSITION PATTERN

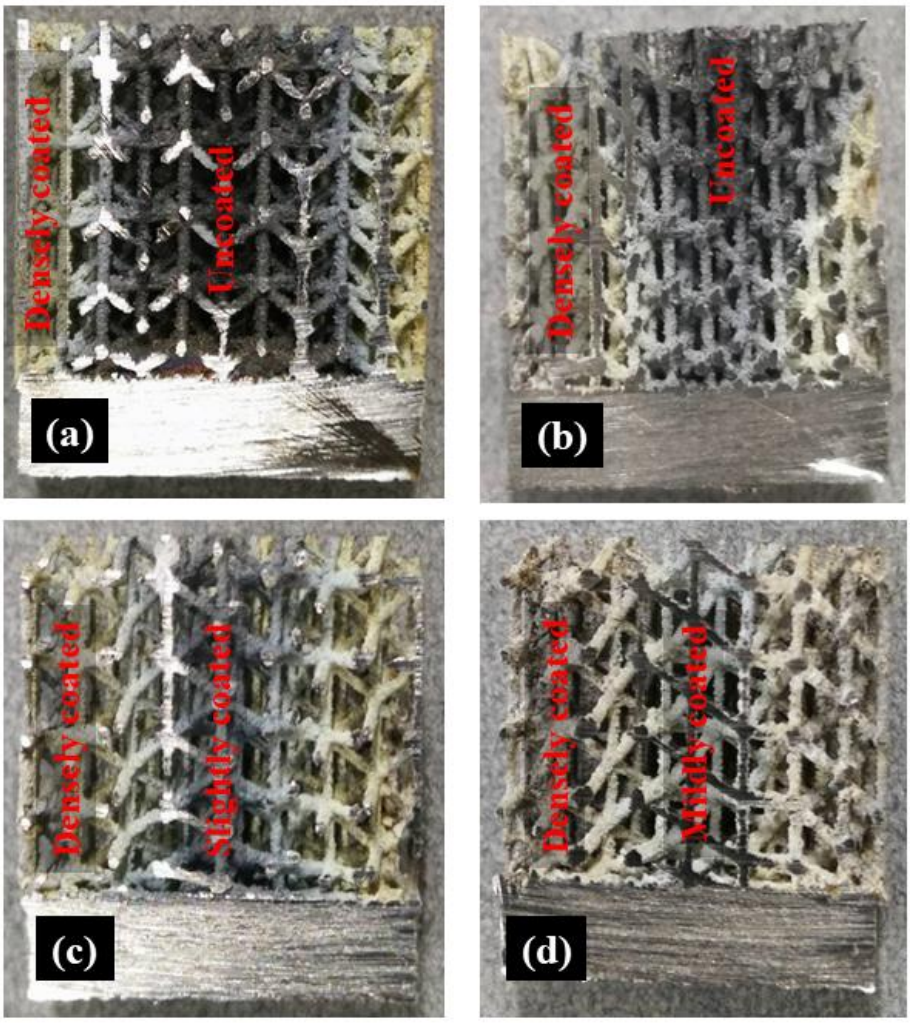

Figure 25. PEO coating deposition pattern from the periphery to the inner part of the porous scaffolds; (a) S_2mm_5mins, (b) S_2mm_7mins, (c) S_3mm_5mins, and (c) S_3mm_7mins.

PEO coating was successfully distributed on the Ti6Al4V porous scaffolds. The cylindrical scaffolds were cut into half to observe the coating pattern from the outer surface to the inner surface of the scaffolds. Figure 25 shows that the coating deposition depends on the size of pores and treatment time. The coating of S_2mm_5mins is densely coated on the outside layer only and the middle of the scaffold remains uncoated. As for S_2mm_7mins, the substrate is slightly coated at

the middle bottom and the area of densely coated is improved. S_3mm_5mins scaffold has better coating deposition compared to S_2mm_5mins and S_2mm_7mins, and the middle part is slightly covered with the PEO coating. Lastly, S_3mm_7mins scaffold is totally covered with PEO coating from the outside surface to the inner surface of the scaffold.

Figure 25 illustrates different coating deposition patterns for every scaffold, which is due to the ability of the sparks formed during the PEO process pass across the pores and longer treatment time would allow stronger sparks to move in the direction from the outside surface to the middle of the scaffolds. Therefore, even though smaller pore size is more promising for bone-ingrowth, it is unfavorable for homogeneous coating deposition patterns on porous scaffold surfaces.

4.3.3 SURFACE CHARACTERIZATION

4.3.3.1 SURFACE MORPHOLOGY

Figure 26 shows SEM images of surface morphologies of Ti6Al4V porous scaffolds before and after PEO process with three different magnifications on the surface of the outer side of the scaffold. The as-manufactured scaffolds (S_2mm and S_3mm) appear to have a certain amount of unmelted particles initial powders (sphere shapes on the surface of struts) adhere to the surface. It is a drawback of powder-bed techniques which can be attributed to the big temperature difference between a loose powder in a powder bed and a solidified material underneath [88]. This occurrence is defined as thermal diffusion [89].

The scaffolds are densely covered with PEO coating on its surface. PEO coating formed on the porous scaffolds is inhomogeneous with regard to its morphologies. It may due to the spark and micro-discharge distribution over the surface of the scaffolds [90]. The morphologies of PEO-

coated surface on the porous scaffolds appear different from the PEO-coated surface on the Ti6Al4V plate substrate. The flocculent structure could be seen over the surface of struts for S_2mm_5mins and S_3mm_5mins. From the enlarged images, the coatings on S_3mm_5mins has the volcanic cone morphology surrounded by different size discharge micropores and numerous numbers of large aperture. The volcanic cone morphology also could be observed with a smaller number of micropores and some cracks on the surface of S_3mm_7mins scaffold. It is fascinating to note the matrix on the surface displays a relatively coarser appearance on S_2mm_5mins and S_2mm_7mins than that on S_3mm_5mins and S_3mm_7mins.

Scaffolds	FESEM images
S_2mm	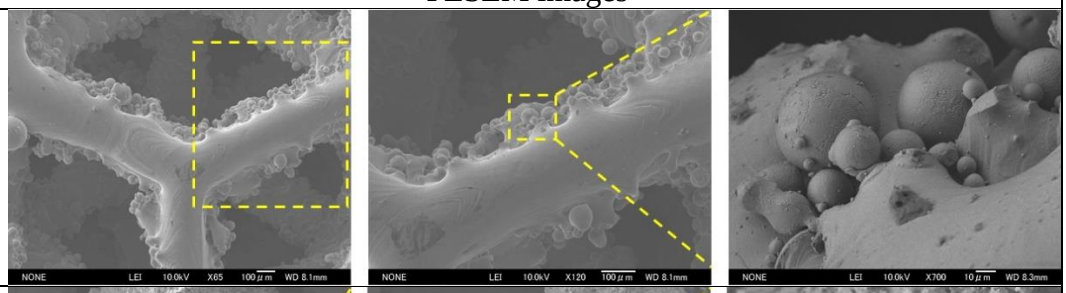
S_2mm_ 5mins	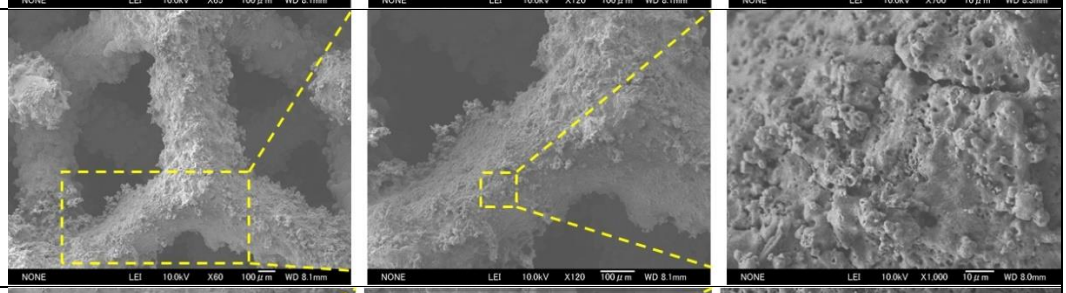
S_2mm_ 7mins	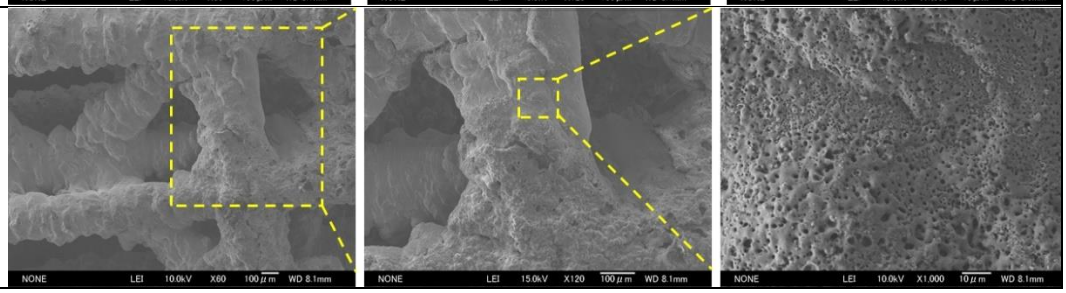

Figure 26. FESEM images of uncoated and PEO coated scaffolds with three different magnification (Continue on next page).

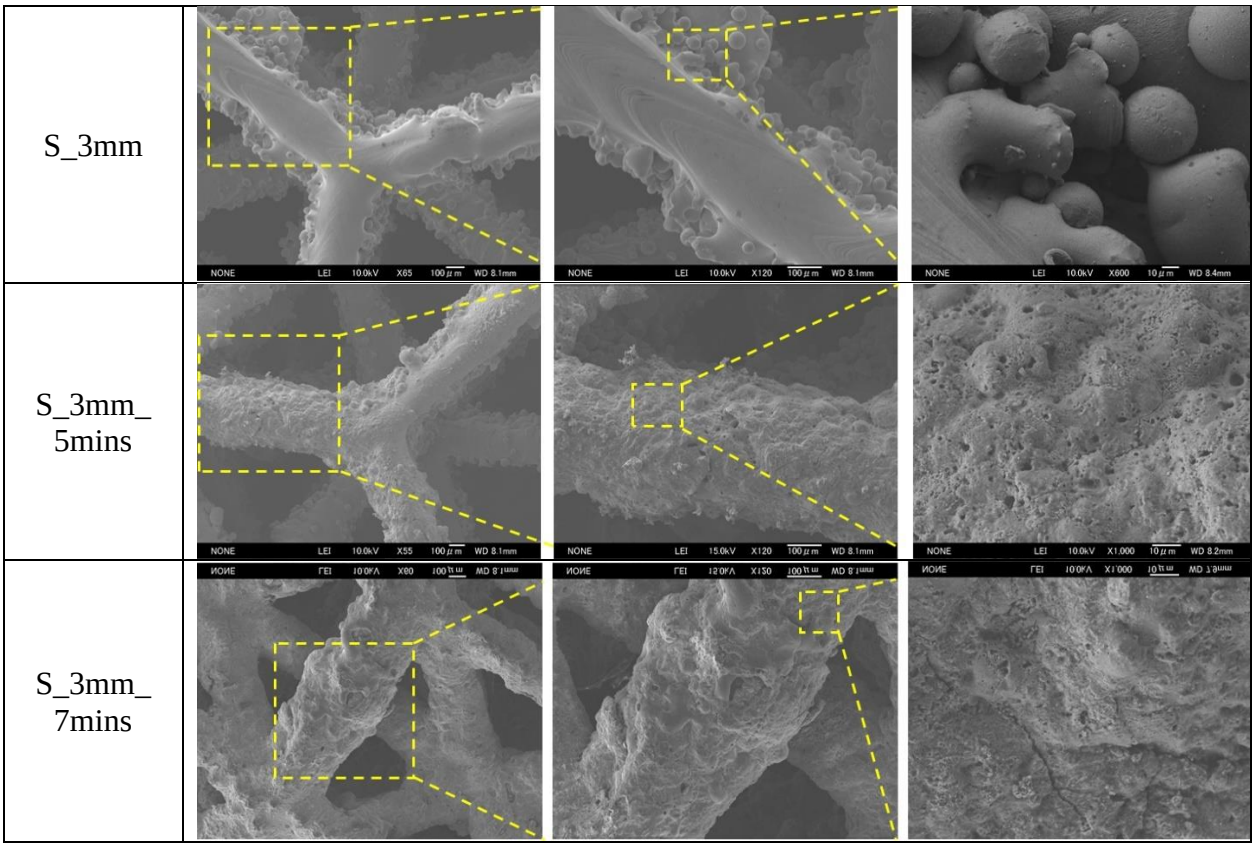

Figure 26. FESEM images of uncoated and PEO coated scaffolds with three different magnification.

The enlarged images filled with micropores were analyzed and Figure 27 shows the micropores characteristic determined with ImageJ software. Figure 28 depicts all the coatings have almost similar average size in the range of 0.656 ~ 0.699 except for S_3mm_5mins has larger micropores average size of 1.553 ± 3.802. However, S_3mm_5mins scaffold has the lowest number of population density of pores compared to other scaffolds. The sizes of micropores and number of population density of pores stretched on the surface of the scaffolds correspondingly related to the sizes and behavior of micro discharge sparks during the process [91]. By analyzing the FESEM images, we could determine the population and characteristics of the micro discharges during PEO process.

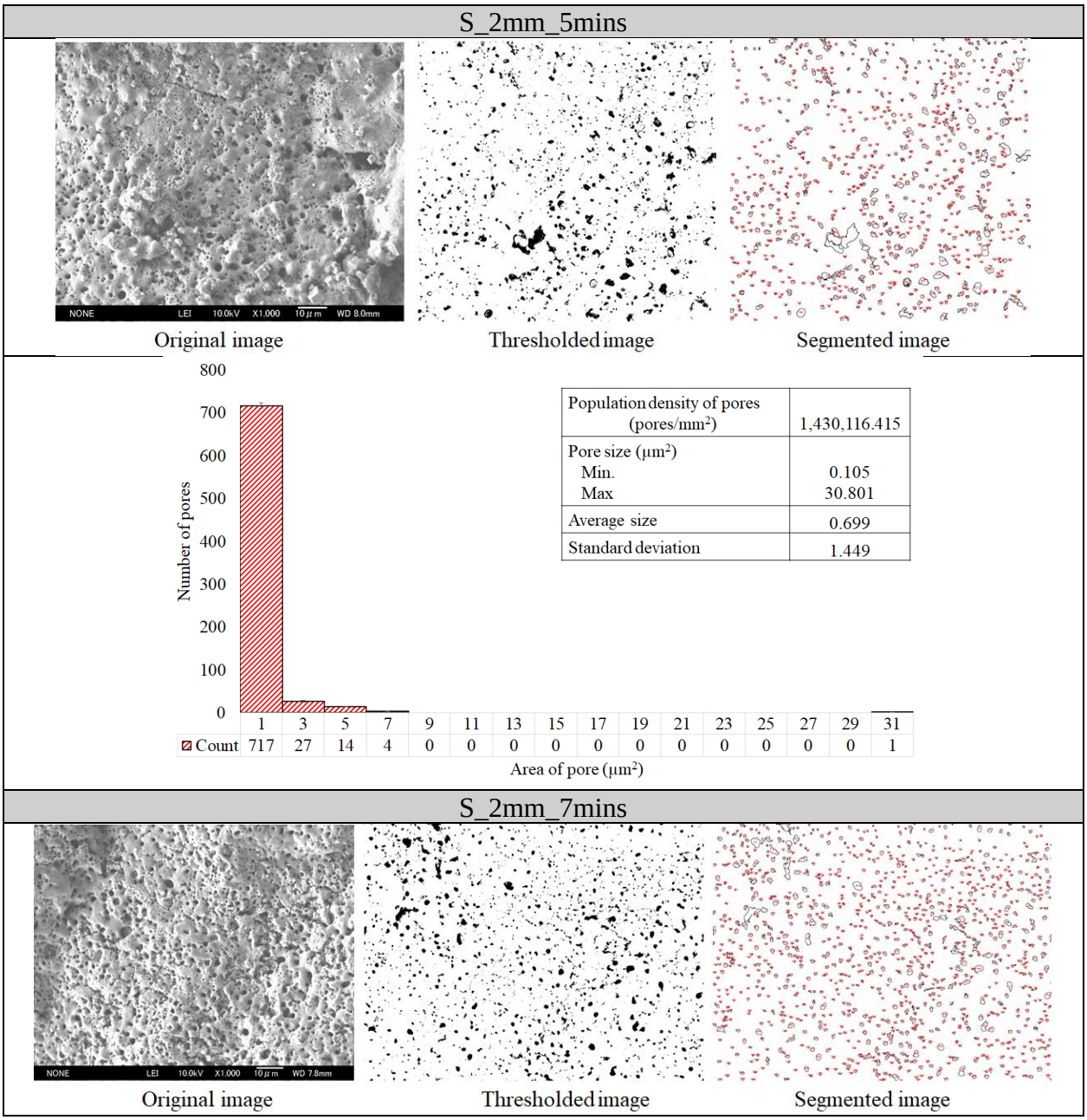

Figure 27. Image analysis on the surfaces of PEO treated porous scaffolds (Continue on next page).

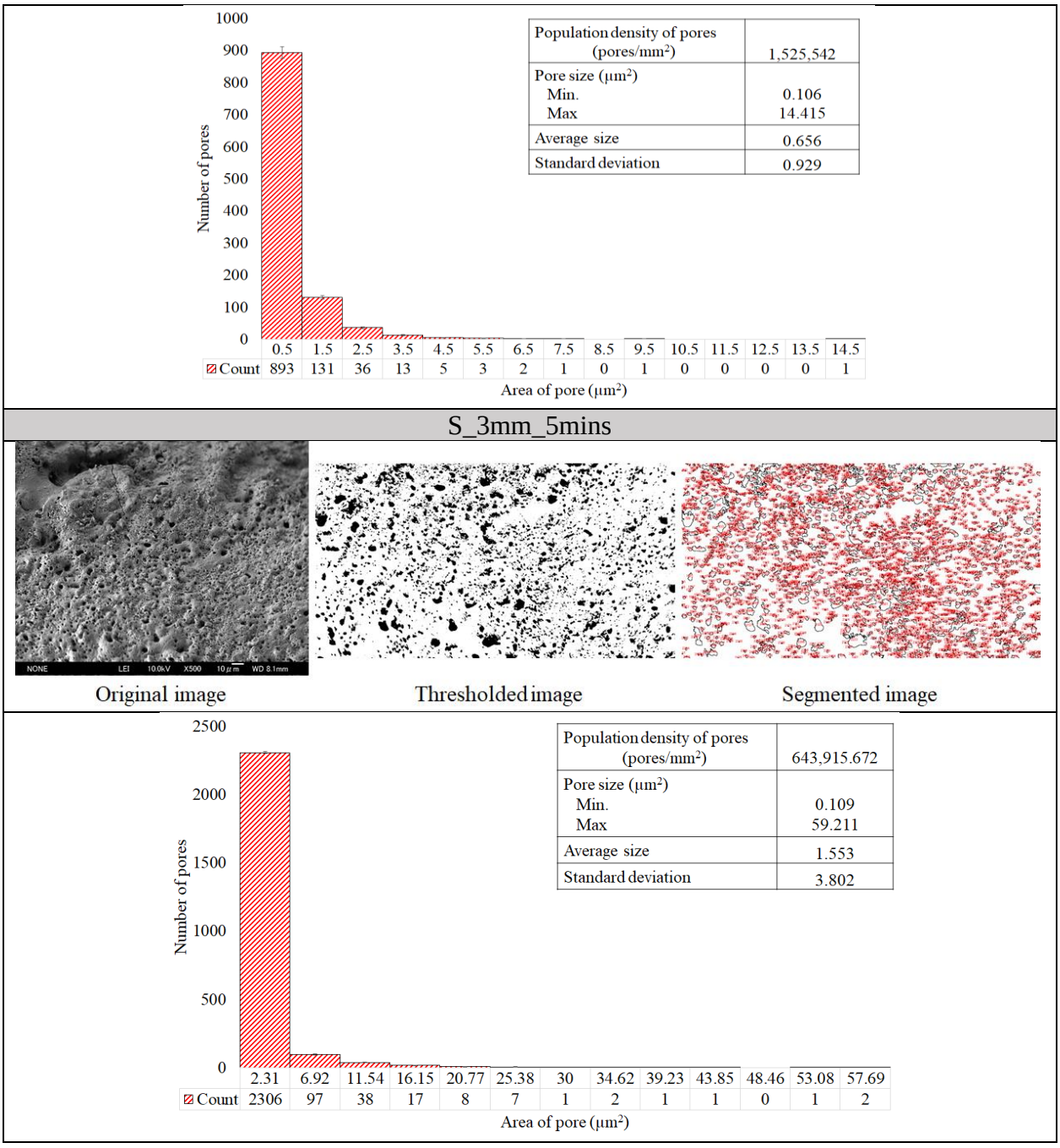

Figure 27. Image analysis on the surfaces of PEO treated porous scaffolds (Continue on next page).

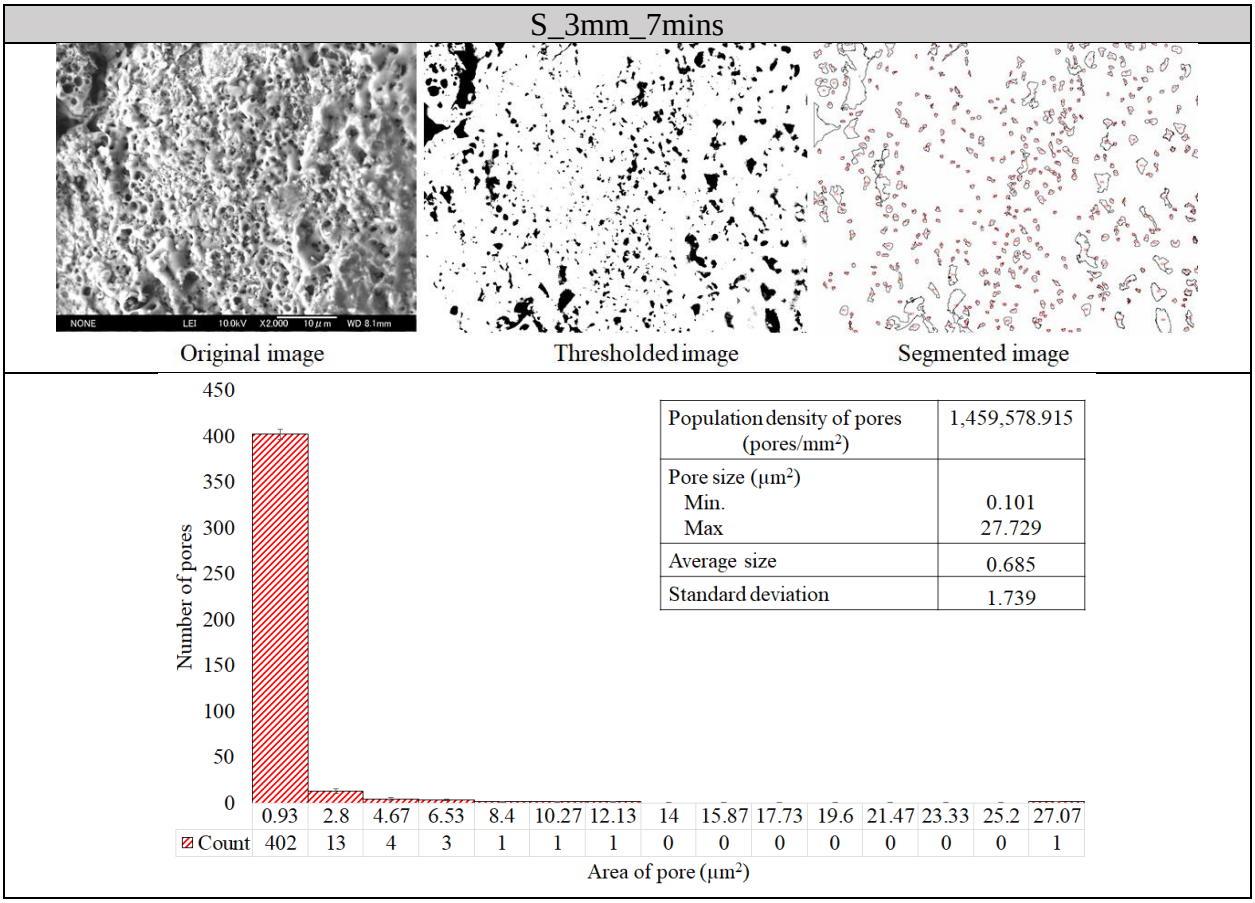

Figure 27. Image analysis on the surfaces of PEO treated porous scaffolds.

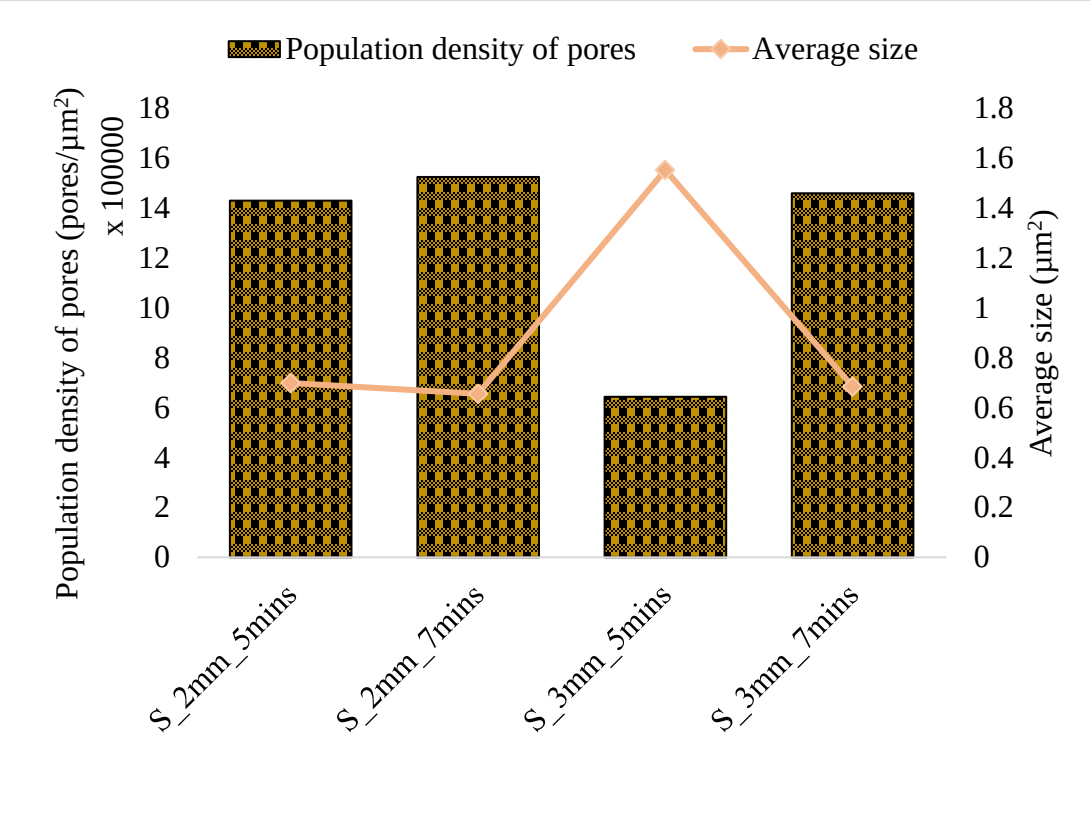

Figure 28. Histogram of population density of pores and the average size of pore for S_2mm_5mins, S_2_7mins, S_3mm_5mins and S_3mm_7mins.

The elemental composition of the coating on Ti6Al4V scaffolds derived from corresponding EDS spectra is shown in Figure 29. Albeit a known shortcoming of EDS analysis in detecting light elements (such as O and F) due to limited sensitivity, must be kept in mind, the analyses still can provide a compositional estimate on the coating surface. The EDS spectra revealed the incorporation of Ca, P and F species from the electrolyte along with the oxygen and the constitutive elements of Ti6Al4V alloy. As reported by Karaji et al [44], the oxidation time would modify the concentration of the alloying elements – the amount of Ti, Al and V decrease and the concentration of Ca and P species increase as the oxidation time increase from 2 to 5 minutes. Figure 30 indicates the amount of atomic % of Ca, P and F elements. In agreement with the study, the concentration of Ti, Al and V had decreased, and Ca, P and F had increased as the

treatment time increase for scaffolds S_3mm_5mins and S_3mm_7mins. In the contrary, the concentration of Ti, Al and V had increased, and Ca, P and F had decreased as the treatment time increase for scaffolds S_2mm_5mins and S_2mm_7mins. This may be due to the selection of the area for the EDS analysis for S_2mm_7mins contain lower concentrations of those elements. The irregularity of the PEO coating on Ti6Al4V scaffolds would lead to non-homogeneity of elemental compositions distribution in the coating. Thus, the result may improve if we could find a region that contains higher chemical elements composition on the surface. Furthermore, in this study and previous works [92,93], oxygen is a predominant element for all the scaffolds. Typical chemical constituent of Ti6Al4V alloy with distinct Ti, Al, and V peaks and absence of other coating element peaks can be observed for as-fabricated scaffolds (S_2mm and S_3mm).

<table>
<tr><th></th><th>EDS spectra</th><th>Chemical element composition</th></tr>
<tr><td>S_2mm</td><td> 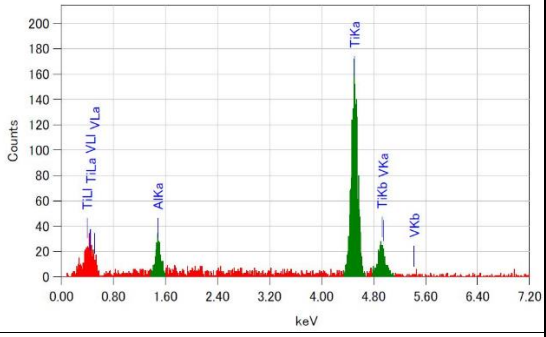
</td><td>
<table>
<tr><th>Element</th><th>Weight %</th><th>Atomic %</th></tr>
<tr><td>Ti K</td><td>92.50</td><td>88.63</td></tr>
<tr><td>Al K</td><td>5.76</td><td>9.81</td></tr>
<tr><td>V K</td><td>1.73</td><td>1.56</td></tr>
<tr><td>Total</td><td>100</td><td>100</td></tr>
</table>
</td></tr>
<tr><td>S_2mm_ 5mins</td><td> 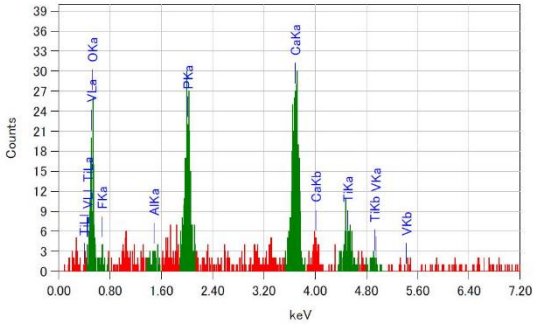
</td><td>
<table>
<tr><th>Element</th><th>Weight %</th><th>Atomic %</th></tr>
<tr><td>Ti K</td><td>7.09</td><td>3.25</td></tr>
<tr><td>Al K</td><td>0.63</td><td>0.51</td></tr>
<tr><td>V K</td><td>1.26</td><td>0.54</td></tr>
<tr><td>Ca K</td><td>23.71</td><td>13.00</td></tr>
<tr><td>P K</td><td>12.99</td><td>9.22</td></tr>
<tr><td>F K</td><td>5.34</td><td>6.17</td></tr>
<tr><td>O K</td><td>48.98</td><td>67.30</td></tr>
<tr><td>Total</td><td>100</td><td>100</td></tr>
</table>
</td></tr>
</table>

Figure 29. EDS spectra with the elemental composition containing in the coating layer and on as-built scaffolds surfaces (Continue on next page).

S_2mm_ 7mins	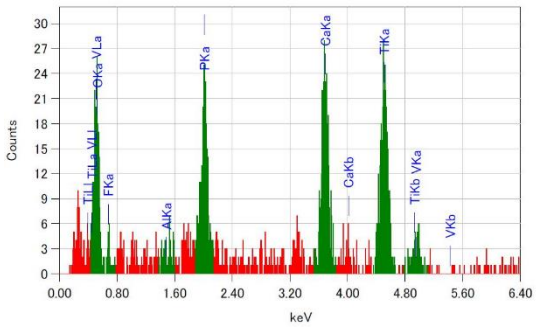	

Element	Weight %	Atomic %
Ti K	24.54	11.91
Al K	-	-
V K	0.11	0.05
Ca K	15.21	8.82
P K	8.90	6.68
F K	8.35	10.21
O K	42.89	62.32
Total	100	100

S_3mm	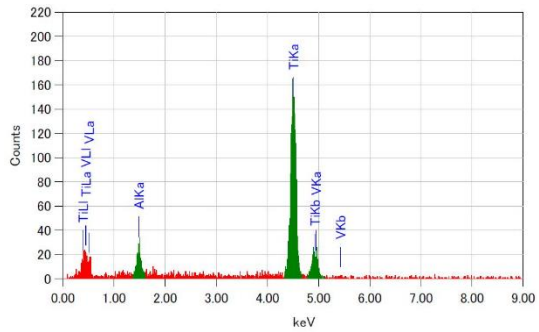	

Element	Weight %	Atomic %
Ti K	94.16	90.18
Al K	5.69	9.68
V K	0.15	0.14
Total	100	100

S_3mm_ 5mins	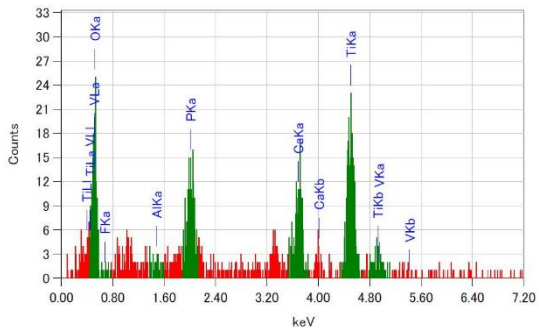	

Element	Weight %	Atomic %
Ti K	28.50	13.34
Al K	0.46	0.38
V K	-	-
Ca K	10.29	5.75
P K	6.42	4.65
F K	1.05	1.23
O K	53.29	74.65
Total	100	100

S_3mm_ 7mins	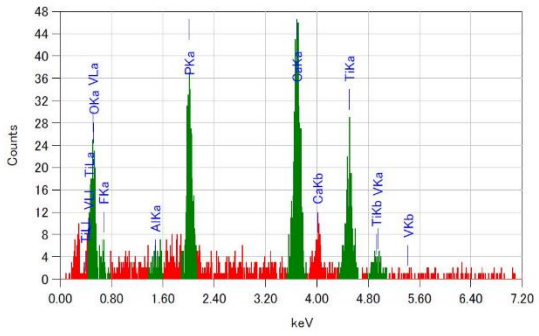	

Element	Weight %	Atomic %
Ti K	19.42	10.14
Al K	0.50	0.46
V K	-	-
Ca K	24.92	15.55
P K	13.93	11.25
F K	7.65	10.07
O K	33.59	52.53
Total	100	100

Figure 29. EDS spectra with the elemental composition containing in the coating layer and on as-built scaffolds surfaces.

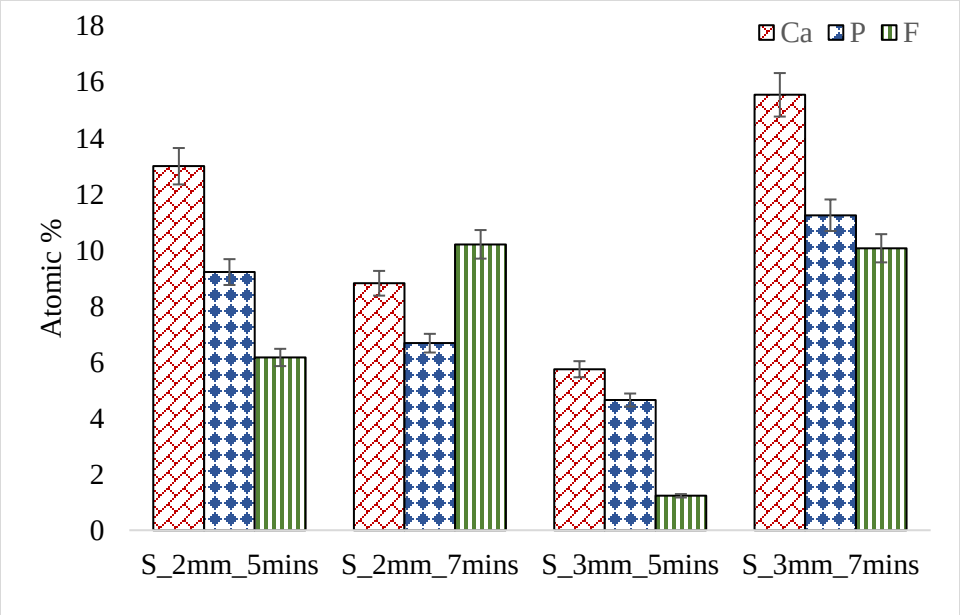

Figure 30. Atomic % of main desired elements from the coating (Ca, P and F) to improve bio-functionality of the scaffolds.

Ca/P ratio of atomic % on the scan area was calculated and shown in Figure 31 and Table 7. The Ca/P ratio of S_2mm_7mins (1.32) is lower than S_2mm_5mins (1.41) due to the lower content of Ca and P in the area of EDS analysis was conducted contrary to others studies when typically the Ca/P ratio would increase when the treatment time increase. Results for S_3mm_5mins and S_3mm_7mins show a slight upward trend with Ca/P ratio of 1.24 and 1.38, respectively. Furthermore, Ca/P ratio of all the scaffolds is almost the same as that of the HAp of natural bone (1.67).

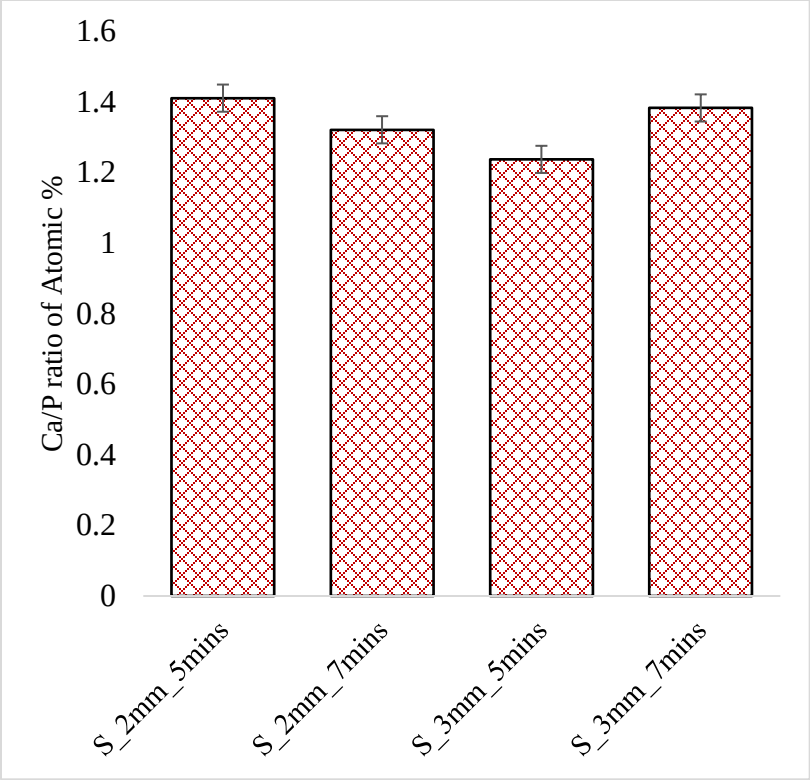

Figure 31. Ca/P ratio of atomic % for PEO coated porous scaffolds.

Table 7. Ca/P ratio of atomic % for PEO coated porous scaffolds.

Scaffolds	Ca/P ratio of Atomic %
S_2mm_5mins	1.41
S_2mm_7mins	1.32
S_3mm_5mins	1.24
S_3mm_7mins	1.38

4.3.3.2 PHASE COMPOSITIONS

XRD analysis on PEO coated surface of Ti6Al4V scaffolds demonstrates peaks corresponding to the scaffold and crystalline phases FAp, HAp, tricalcium phosphate, anatase, rutile, vanadium (V) oxide, aluminum oxide and titanium (Figure 32). As discussed in 3.3.2, the electrolyte used in this study exhibited the ability to incorporate HAp and FAp crystals on Ti6Al4V

plate as well as on SLM manufactured Ti6Al4V porous scaffolds. Moreover, the electrolyte solution allows the incorporation of a greater amount of bio-functional phases on SLM manufactured Ti6Al4V porous scaffolds compared to the Ti6Al4V substrate despite shorter PEO treatment time. XRD spectra for S_2mm and S_3mm demonstrate the phase of titanium as a dominant element in Ti6Al4V alloy. The peaks are consistent with XRD database 9008517, suggesting all the peaks in Figure 32 a,b (for 2mm and 3 mm without coating) belong to titanium. In general, it can be noted that more diffraction peaks can be observed on XRD spectra of S_2mm_5mins. This could be a result of a larger surface area to allow the deposition of PEO coating on the scaffold surface. Peaks corresponding to HAp and FAp for S_2mm_5mins show higher intensity in the region $2\theta = 30°$ to 35° and compared to other PEO-coated scaffolds. Furthermore, the peaks attributed to HAp and FAp for S_2mm_5mins appear more abundant compared to the other PEO-coated scaffolds. Peaks attributed to anatase and rutile are observed in the XRD spectra of the PEO-coated scaffolds, with rutile peaks predominantly present in the XRD spectra, indicating that rutile becomes more abundant in the coating. It has been envisaged that the anatase to rutile phase transformation is a time and temperature-dependent process – longer treatment time would transform more anatase to rutile phase. Peaks corresponding to titanium still can be found on all coated scaffolds (with lower intensity compared to uncoated scaffolds) along with the oxidation of aluminum and vanadium (V). S_2mm_7mins exhibits low content of HAp and FAp despite longer treatment time and this is due to the XRD spot analysis is in the region where the crystalline phase is little. Shin et al [94] suggested that low HAp content in the coating could be correlated to HAp particles reacting with phosphate ions in the electrolyte or TiO_2 and decay as treatment time and/or temperature increase.

S_3mm_5mins is enriched with rutile and anatase and low of HAp and FAp compared to S_2mm_5mins and this is possibly resulting from the lower temperature that could transfer through larger pores [44]. S_3mm_7mins demonstrates a pattern with broad scattering hump and mild intensity diffraction but intensely covered with HAp and FAp with rutile and anatase becomes less abundant in the coating. Sets of peaks that match vanadium (V) oxide and aluminum oxide can be observed in the pattern of S_3mm_5mins and S_3mm_7mins scaffolds.

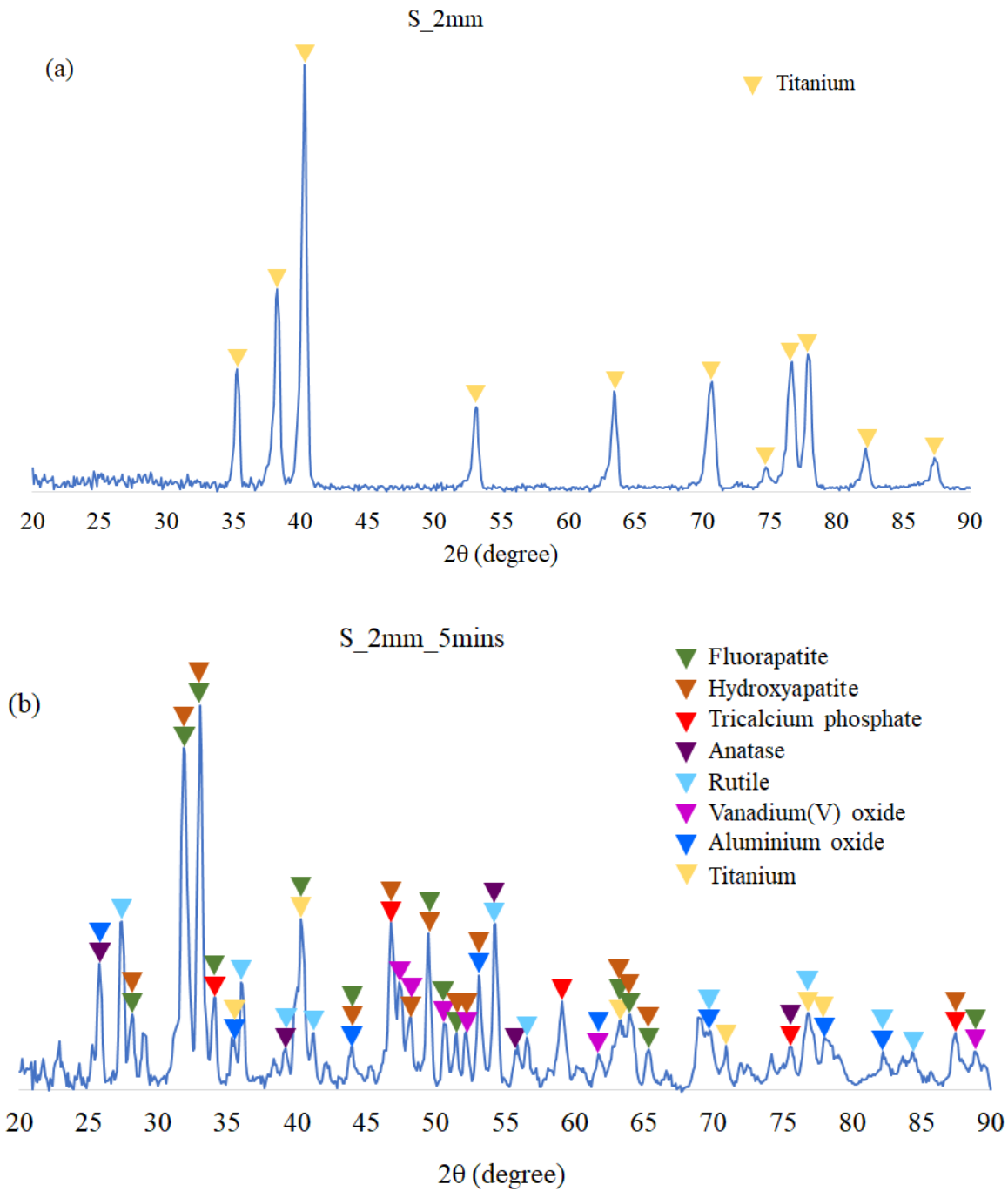

Figure 32. XRD pattern of PEO coatings on the surfaces of SLM-manufactured porous scaffolds; (a) S_2mm, (b) S_2mm_5mins, (c) S_2mm_7mins, (d) S_3mm, (e) S_3mm_5mins, and (f) S_3mm_7mins (Continue on next page).

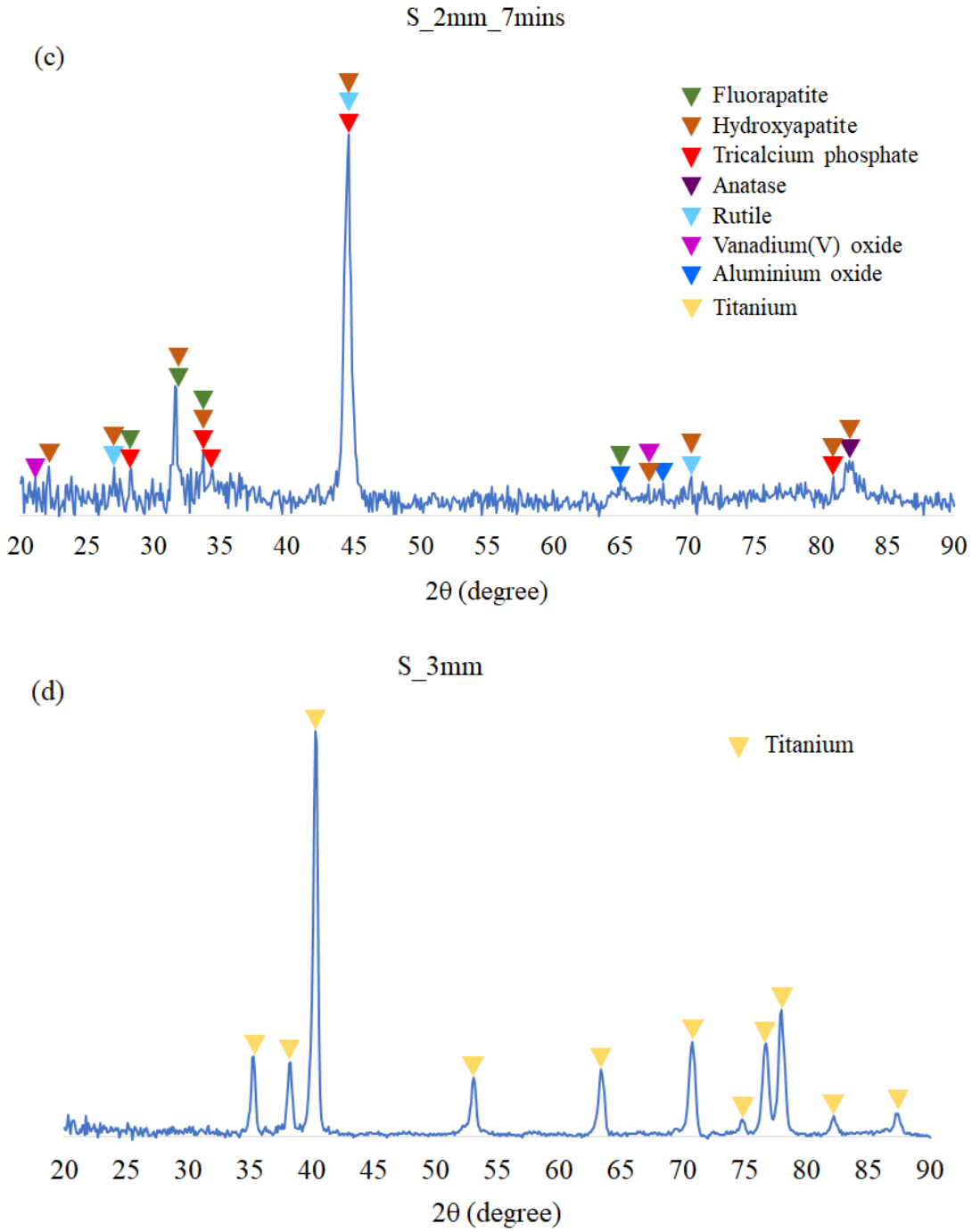

Figure 32. XRD pattern of PEO coatings on the surfaces of SLM-manufactured porous scaffolds; (a) S_2mm, (b) S_2mm_5mins, (c) S_2mm_7mins, (d) S_3mm, (e) S_3mm_5mins, and (f) S_3mm_7mins (Continue on next page).

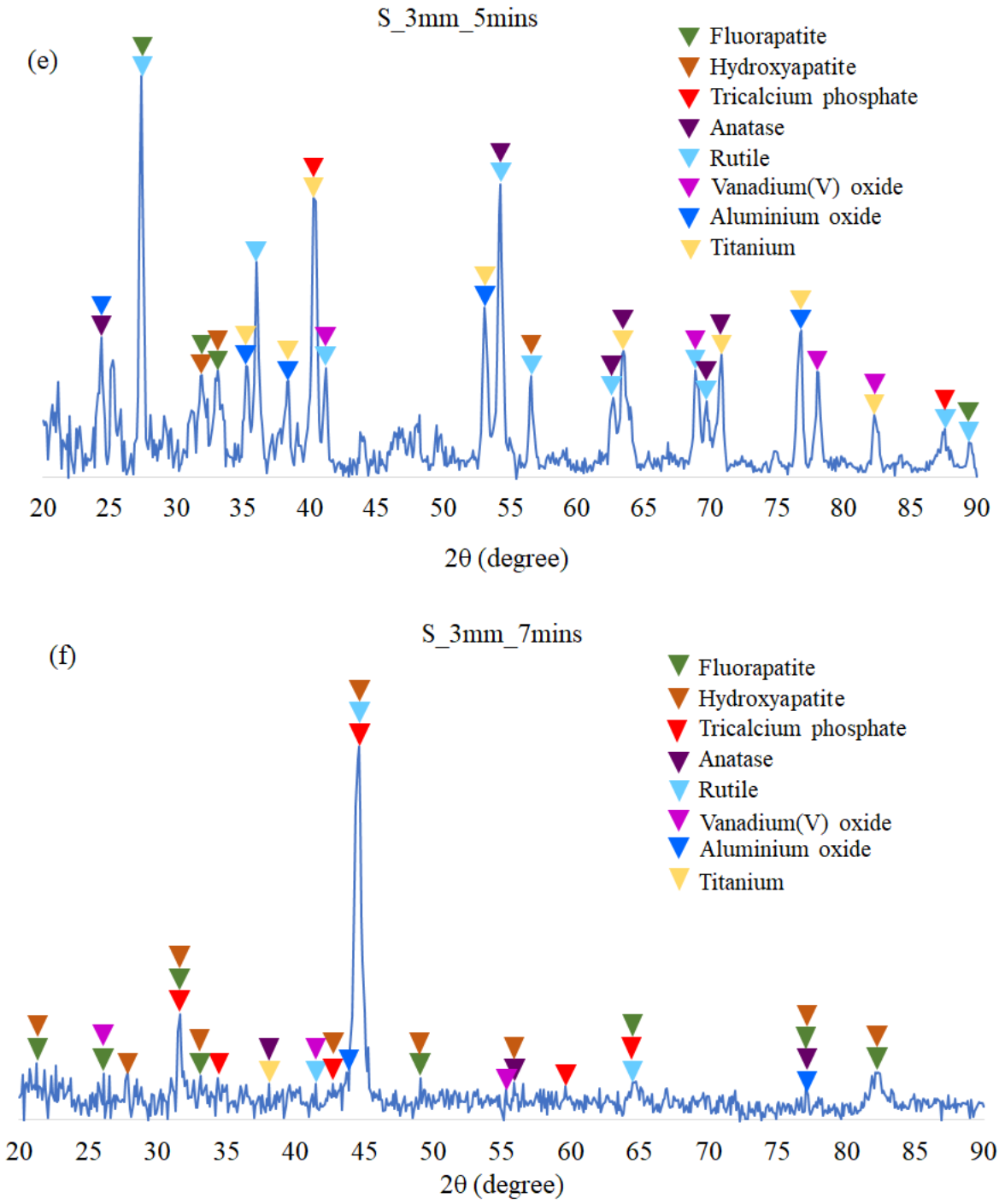

Figure 32. XRD pattern of PEO coatings on the surfaces of SLM-manufactured porous scaffolds; (a) S_2mm, (b) S_2mm_5mins, (c) S_2mm_7mins, (d) S_3mm, (e) S_3mm_5mins, and (f) S_3mm_7mins.

By using XPS survey spectra, distinct elements distribution on the coating namely, calcium (Ca 2p 3/2), phosphorus (P 2p 3/2), fluorine (F 1s), titanium (Ti 2p 3/2) and oxygen (O 1s) along with adventitious carbon (C 1s) can be observed (Figure 33). The C 1s peak position due to the adventitious carbon was detected at the binding energy (BE) within the range of 282 to 294 eV for all coatings the peak was used to calibrate the XPS spectrum.

In Ca 2p 3/2 spectra the higher sub-peak centered at 351.9 eV for S_2mm_7mins and S_3mm_7mins and slightly shift to 348.6 eV for S_2mm_5mins and S_3mm_5mins, proving the presence of Ca salt and the effect of PEO treatment time on the composition of Ca in the coating. The Ca 2p 3/2 peaks in the spectra are in accordance with the binding energies of calcium in HAp and FAp. The P 2p 3/2 spectra also exhibit a slight shift of peak for longer treatment time; 134.5 eV for S_2mm_5mins and S_3mm_5mins and 137.5 eV for S_2mm_7mins and S_3mm_7mins. The finding asserts the existence of PO_4^{3-} in the coating and confirms the coating contains HAp. The F 1s bands have peaks centered at a range of 685.9 to 689.4 eV for all treated scaffolds, which can be referred to F in FAp.

The binding energies of Ti 2p 3/2 equaling to 460 eV, 461.6 eV, 459.9 eV and 462.5 eV for S_2mm_5mins, S_2mm_7mins, S_3mm_5mins and S_3mm_7mins, respectively, can suggest the presence of titanium in the surface layer. Regarding O 1s spectra, it can be observed peaks at 531.4 eV, 534.9 eV, 531.9 eV and 534.7 eV for S_2mm_5mins, S_2mm_7mins, S_3mm_5mins and S_3mm_7mins, respectively, which correspond to Ti-O bonds in TiO_2 layer presented after PEO treatment.

Scaffolds	XPS narrow scan peaks
S_2mm_5mins	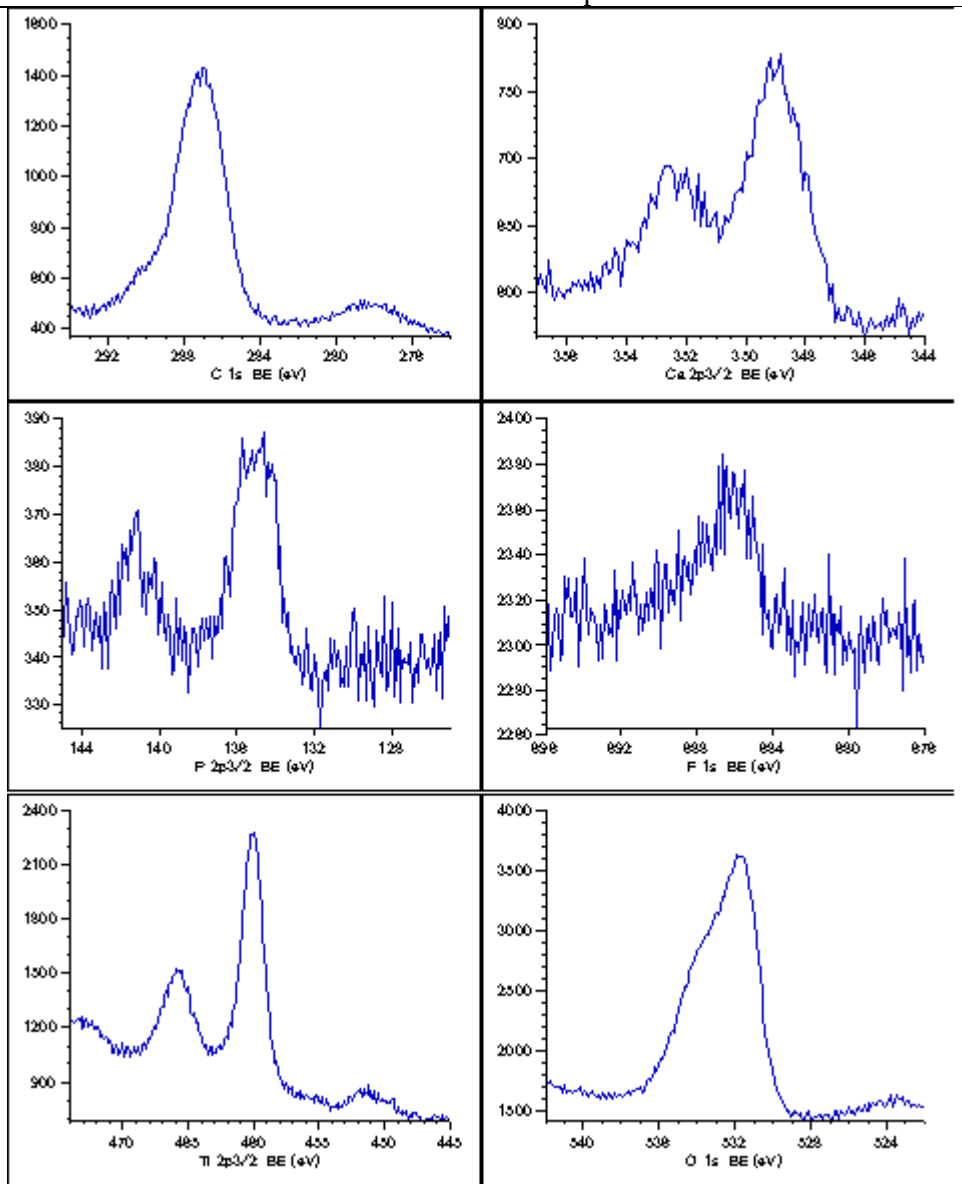

Figure 33. Comparison of Ca 2p 3/2, P 2p 3/2, F 1s, Ti 2p 3/2 and O 1s XPS spectrum between PEO coated scaffolds; (a) S_2mm_5mins, (b) S_2mm_7mins, (c) S_3mm_5mins, and (d) S_3mm_7mins (Continue on next page).

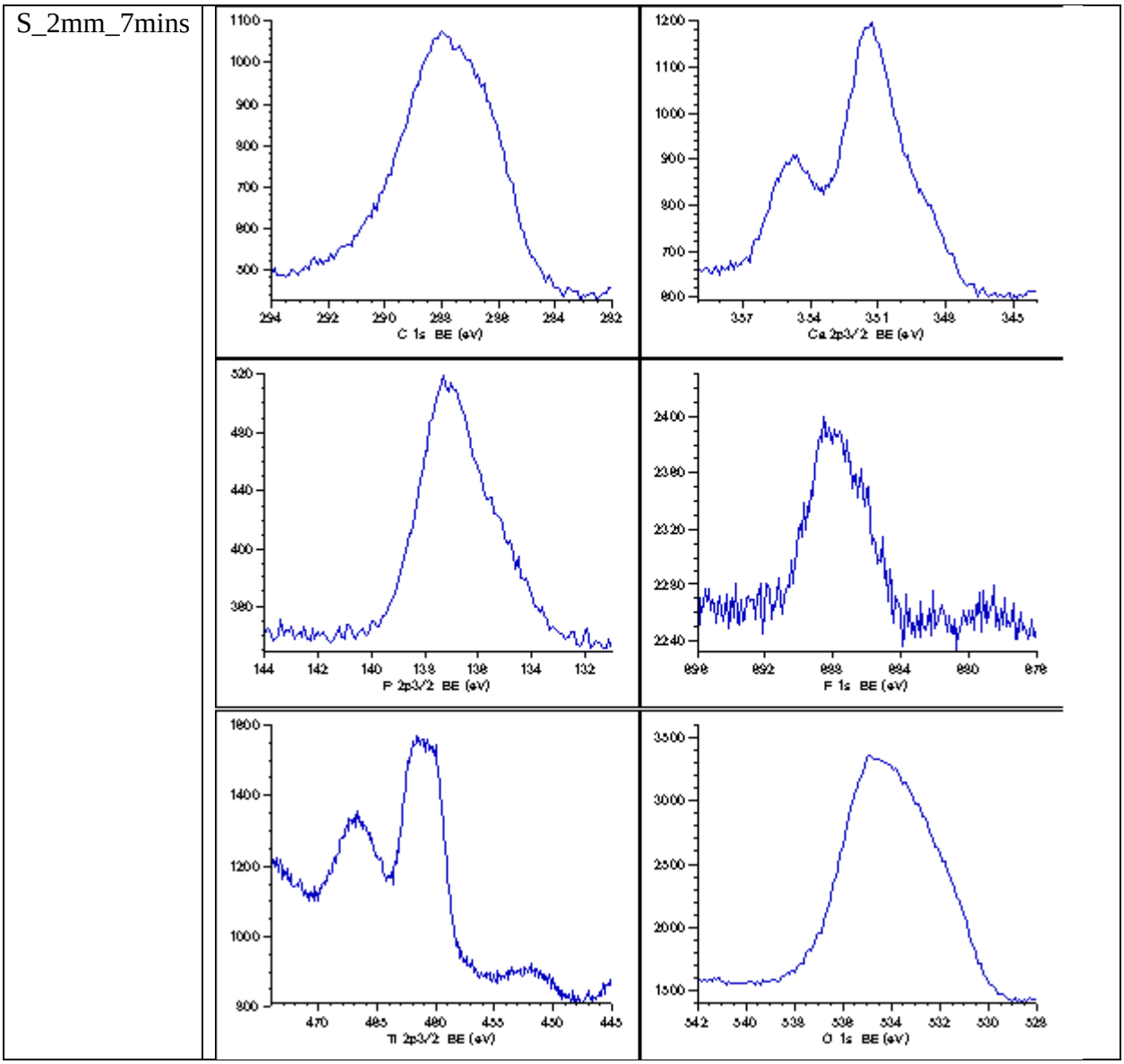

Figure 33. Comparison of Ca 2p 3/2, P 2p 3/2, F 1s, Ti 2p 3/2 and O 1s XPS spectrum between PEO coated scaffolds; (a) S_2mm_5mins, (b) S_2mm_7mins, (c) S_3mm_5mins, and (d) S_3mm_7mins (Continue on next page).

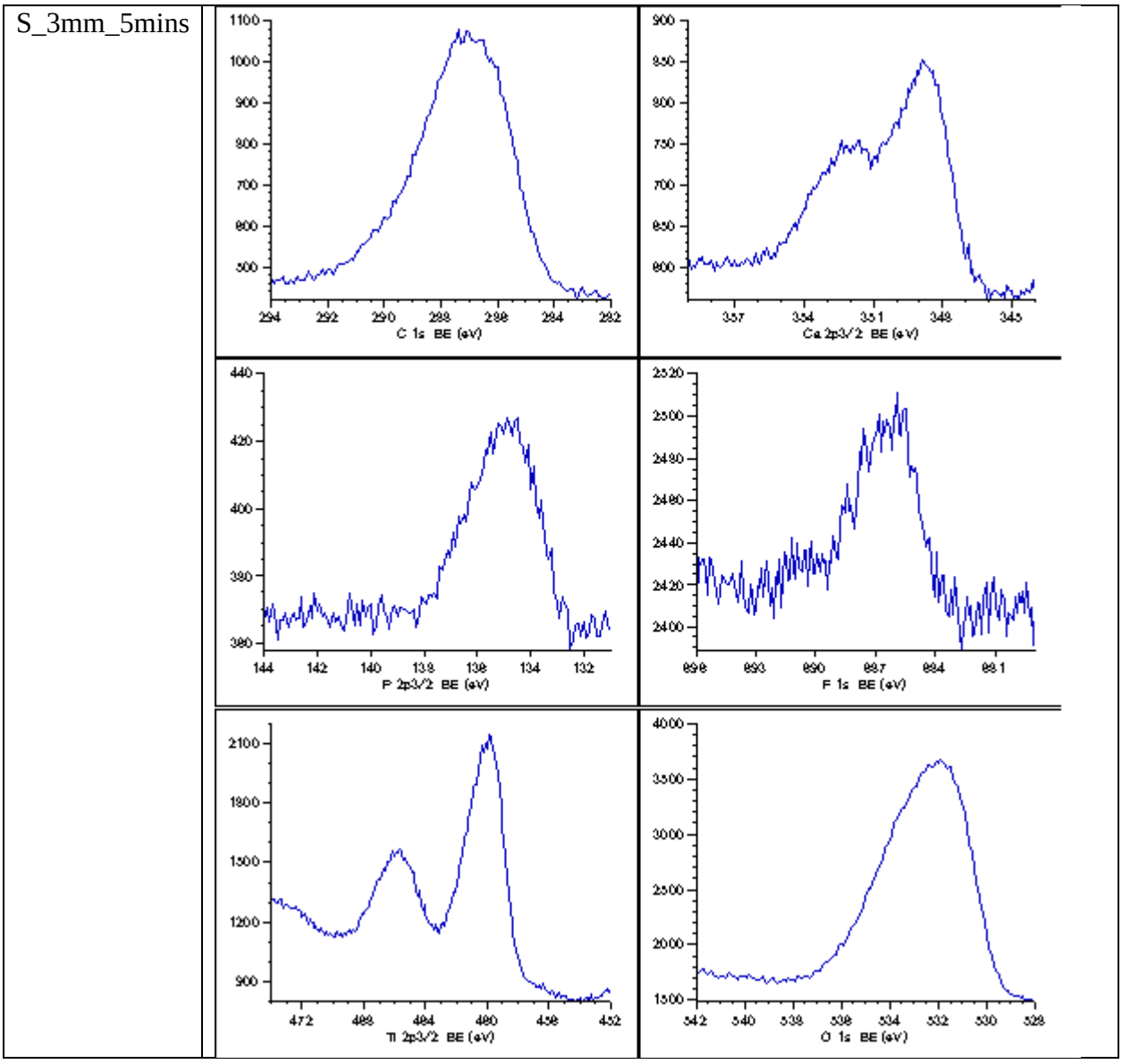

Figure 33. Comparison of Ca 2p 3/2, P 2p 3/2, F 1s, Ti 2p 3/2 and O 1s XPS spectrum between PEO coated scaffolds; (a) S_2mm_5mins, (b) S_2mm_7mins, (c) S_3mm_5mins, and (d) S_3mm_7mins (Continue on next page).

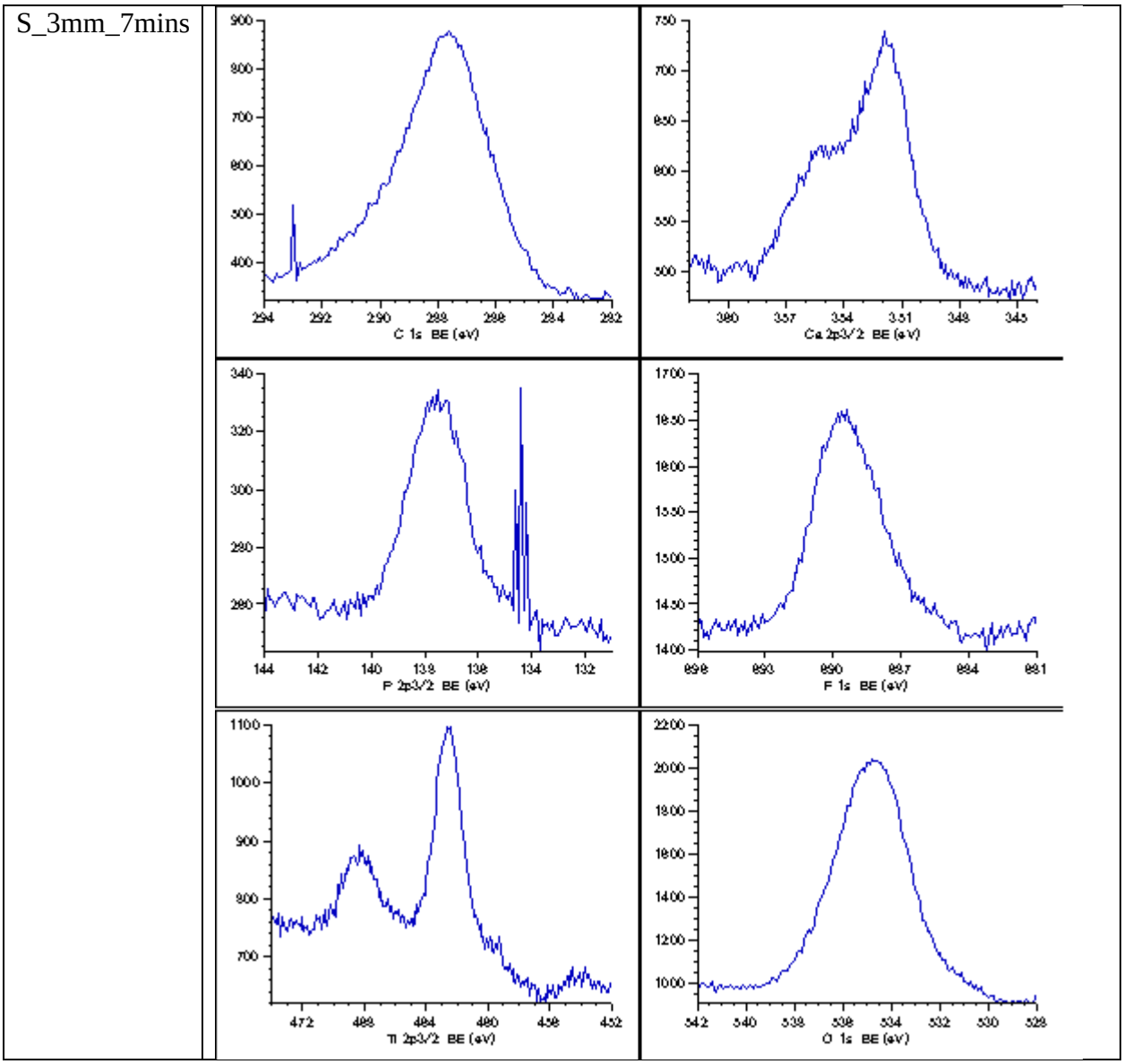

Figure 33. Comparison of Ca 2p 3/2, P 2p 3/2, F 1s, Ti 2p 3/2 and O 1s XPS spectrum between PEO coated scaffolds; (a) S_2mm_5mins, (b) S_2mm_7mins, (c) S_3mm_5mins, and (d) S_3mm_7mins.

4.3.4 MECHANICAL TEST

To evaluate the effect of PEO treatment on the mechanical properties of the porous scaffolds, we performed a quasi-static compression test. It is crucial to investigate the mechanical properties of porous biomaterials for orthopedic implants as it must be able to accomplish the purpose to diminish the stiffness mismatch between the implant and the adjacent tissue and thus reduce the risk of stress shielding. Besides, the scaffolds should be capable of conferring adequate mechanical strength to ensure no failure occurs when subjected to physiological mechanical loading. Two batches of scaffolds were manufactured at different times.

Figure 34 illustrates typical stress-strain curves of porous scaffolds which yield substantial information on porous structure behavior. PEO treatment does not modify the trend of stress-strain curves which can be seen in Figure 34, stress-strain curves for PEO-treated scaffolds exhibit a similar trend with and without PEO coating scaffolds. The compression test was conducted in three sets of samples (18 comparisons in total) with two different batches of SLM-fabricated scaffolds. S_2mm_5mins (1), S_2mm_7mins (1), S_3mm (1), S_3mm_5mins (1) and S_3mm_7mins (1) are from the first batch of fabrication, on that account, their stress-strain curves trend are slightly different due to the influence parameters during production and post-processing of production.

The scaffolds S_2mm_(1), S_2mm_5mins (1), S_2mm_7mins (1), S_3mm (1), S_3mm_5mins (1) and S_3mm_7mins (1) are from the first batch of fabrication which has been treated with heat treatment at the post-processing stage. Heat treatment was applied to improve the ductility of the SLM-fabricated porous scaffolds. However, an error occurred during the compression test of S_2mm_(1) and we had a limited number of scaffolds. Therefore, it is unfeasible to calculate energy absorption from the scaffold S_2mm_(1). The scaffolds S_2mm_(2), S_2mm_5mins (2), S_2mm_7mins (2), S_3mm (2), S_3mm_5mins (2) and S_3mm_7mins (2),

S_2mm_(3), S_2mm_5mins (3), S_2mm_7mins (3), S_3mm (3), S_3mm_5mins (3) and S_3mm_7mins (3) are from the second batch of fabrication and all the scaffolds were made of from similar SLM metallic powder with similar manufacturing. The scaffolds from the second batch were not treated with heat treatment.

In the initial parts of the response of the strain-stress curve with linear trends to the maximum stress point for all scaffolds followed by a sudden drop to the minimum point of the curves when the scaffolds are crushed. In a study with almost similar unit cell structure [95], a sudden drop of stress value is attributed to the early failure in the connection points between struts in the middle of the structure and an instantaneous stress-release at the failure point. The test proved that lower relative density scaffolds caused earlier failure where the failure of S_3mm, S_3mm_5mins and S_3mm_7mins scaffolds occurred before 7% of strain compared to others scaffolds with higher relative density.

In the later region of the stress-strain curves, multiple fluxes of stress values appear to be related to the collapse of different layers. The scaffolds broke diagonally (after the compression test began) where the fracture initially occurred at the weaker struts and collapsed on the lower layers. The diagonal deformation correlated with the diagonal shear mechanism in which the shear failure mode occurs due to the size of the lattice array and structure response to the outer open cell boundary conditions [95]. The shearing failure mechanism or diagonal shear mechanism which can be observed in this study is also correlated to the orientation of the tying struts [96], the higher the inclination angle, the more shearing failure is observed for the porous scaffold. Shearing of layers coincide with the bending failure of the tying struts parallel to the load direction and consequently influence the stress-strain behavior of scaffolds [97,98]. The successive local peaks in the second part of the stress-strain curve represent the failure of the successive layers of the

porous structure. The value of local peaks related to the collapse of successive layers of the porous structure is lower than the first peak value (maximum stress point) attributable to the fact that a proportion of the struts in the following layers are also destructed after the collapse of the first diagonally broken layer. These fluctuations of the stress continue until the crosshead movement reached the set-up limit. In a previous study [44], the stress-strain curves continue up to the collapse of all layers until the final linear part appears which indicates the densification of porous structures. This is a common behavior of stress-strain curve for porous structures which is associated with the ability to absorb energy to any increment of stress value [99].

PEO-treated scaffolds exhibit higher ductility compared to the as-manufactured scaffolds and prolonged treatment time slightly impacted the ductility of the SLM-manufactured scaffolds. Khan et al. [100], investigated the effect of the applied current density and electrolyte concentration during PEO process on the surface morphology of the coating and mechanical properties of aluminum alloy. They suggested that plasma micro-discharge events caused by high local temperatures during the PEO process could affect the mechanical properties of the coating. Thus, in the case of SLM-manufactured scaffolds, PEO treatment may anneal and sinter partially melted powder, separated particles and tiny defects formed during SLM fabrication such as incomplete fusion holes and cracks [101] and mitigate the probable defects. Ultimately, the sintering and annealing effects during the PEO process may slightly enhance the mechanical properties of SLM-fabricated scaffolds. Furthermore, repeated rapid cooling during the SLM process bring forth the accumulation of residual stresses in the scaffold structure which may cause the extensive formation of brittle martensitic microstructures [44]. Therefore, heat treatment in the post-processing stage is required as a means to control the phase transformation and optimize the mechanical properties of the SLM-manufactured part [102]. In addition, local high temperatures

during PEO process may benefit slightly in the accumulated residual stresses released attributable to the stress relaxation effect [100,103].

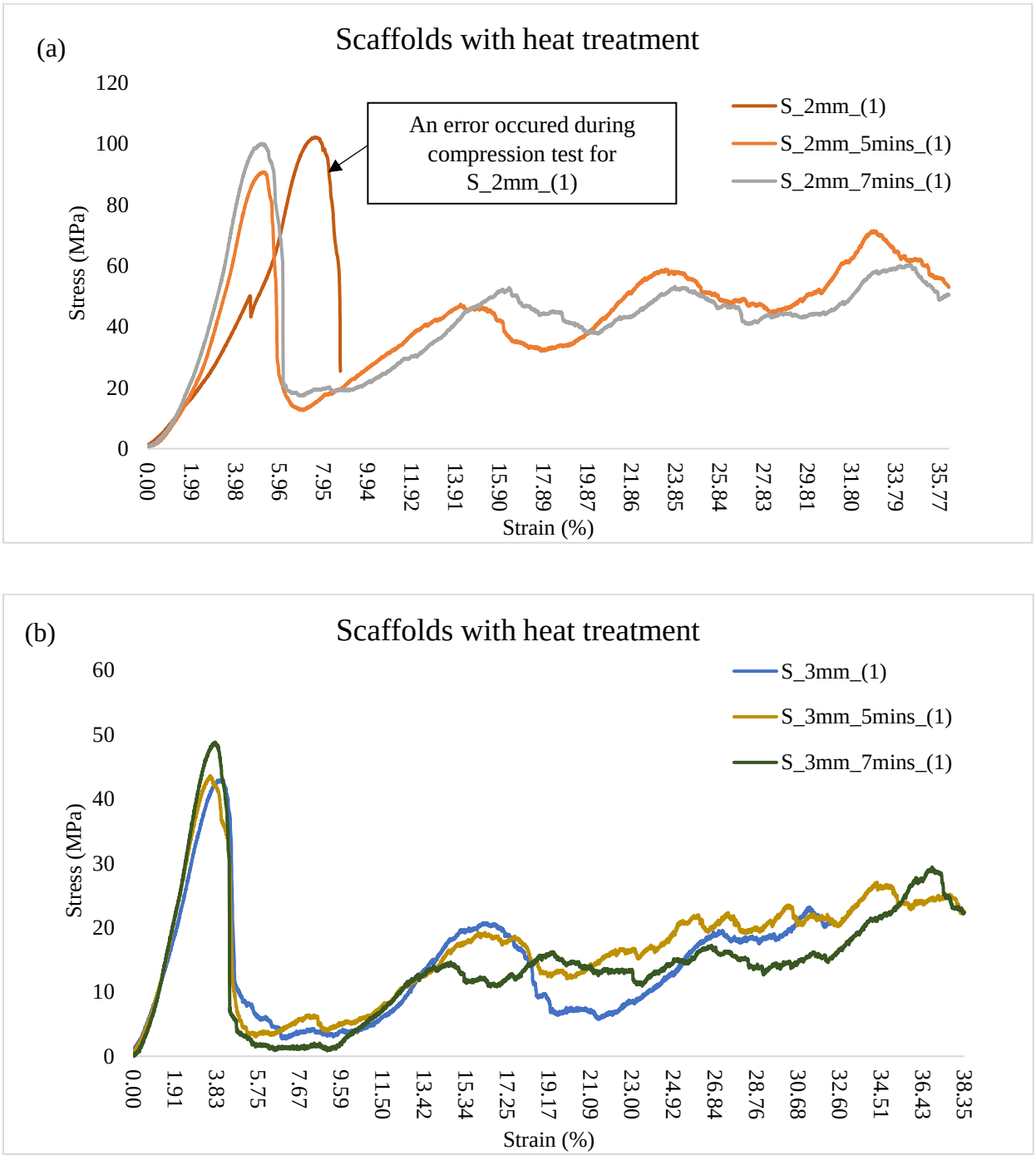

Figure 34. Stress-strain curves for heat-treated scaffolds; (a) uncoated and coated scaffolds with D=2mm and (b) uncoated and coated scaffolds with D=3mm.

Figure 35 exhibits the stress-strain curves of scaffolds without heat treatment. The trend of the curves is almost similar to the curves with heat treatment except for the sudden drop after the first linear steep increase. Remarkably, the stress value drops to slightly below zero for all the scaffolds without heat treatment. According to a study by Yue et al. [104], this behavior is due to the formation of shear bands which can be observed during the compression test. However, this shear band formation can be suppressed by post-processing heat treatment as can be seen in the stress-strain curves of the scaffold with heat treatment. This finding confirms that post-processing heat treatment potentially could improve the compressive strength of SLM-manufactured porous scaffold and shear band formation would cause negative effects on the compressive strength and energy absorption. In addition, the subsequent peaks after the first peak stress are lower for scaffolds without heat treatment compared to scaffolds with heat treatment.

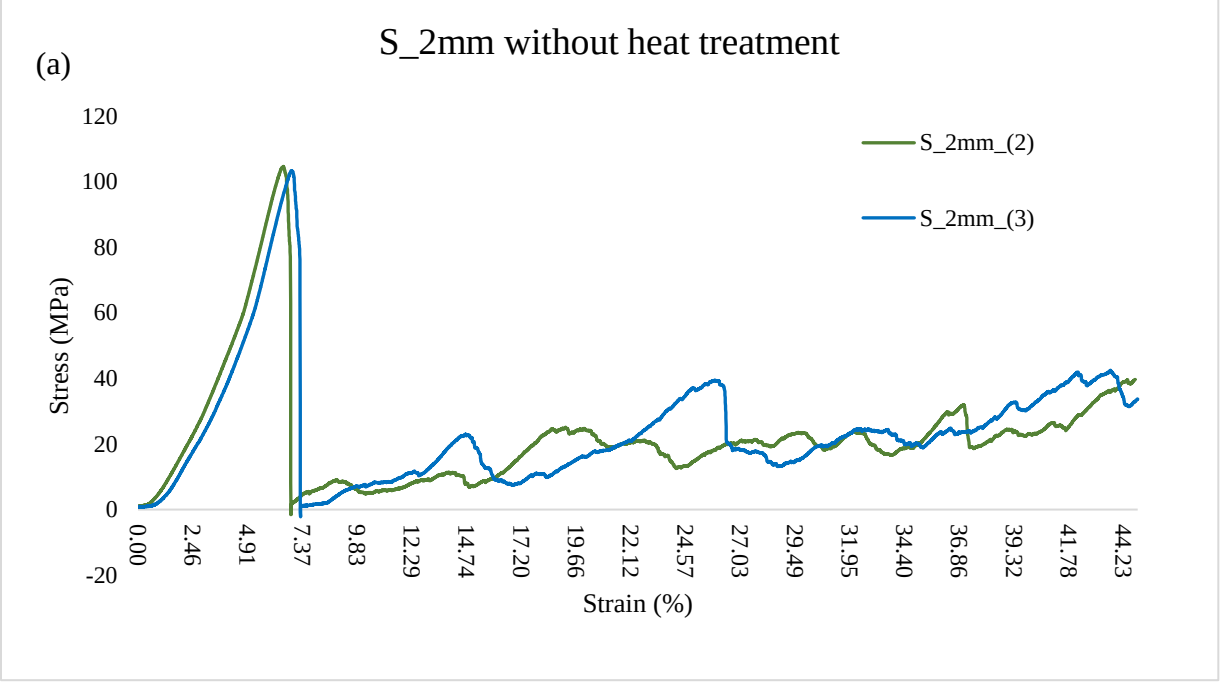

Figure 35. Stress-strain curves without post-processing heat treatment for uncoated and PEO coated scaffolds; (a) S_2mm, (b) S_2mm_5mins, (c) S_2mm_7mins, (d) S_3mm, (e) S_3mm_5mins, and (d) S_3mm_7mins (Continue on next page).

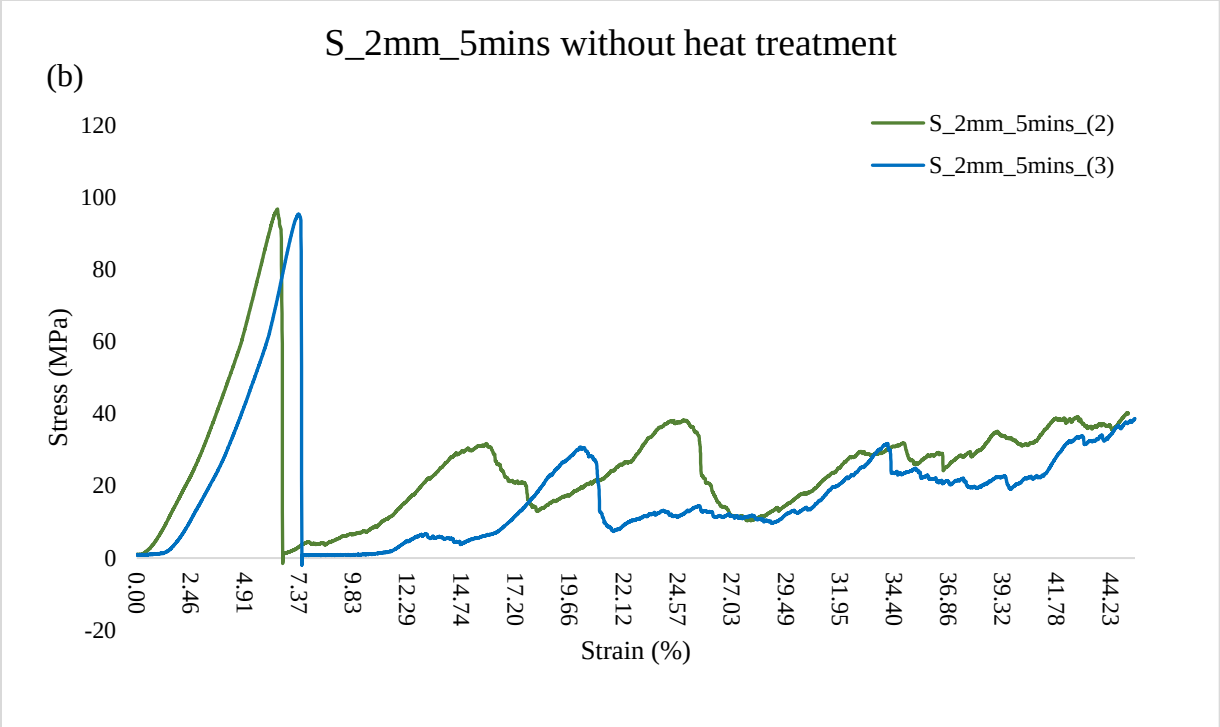

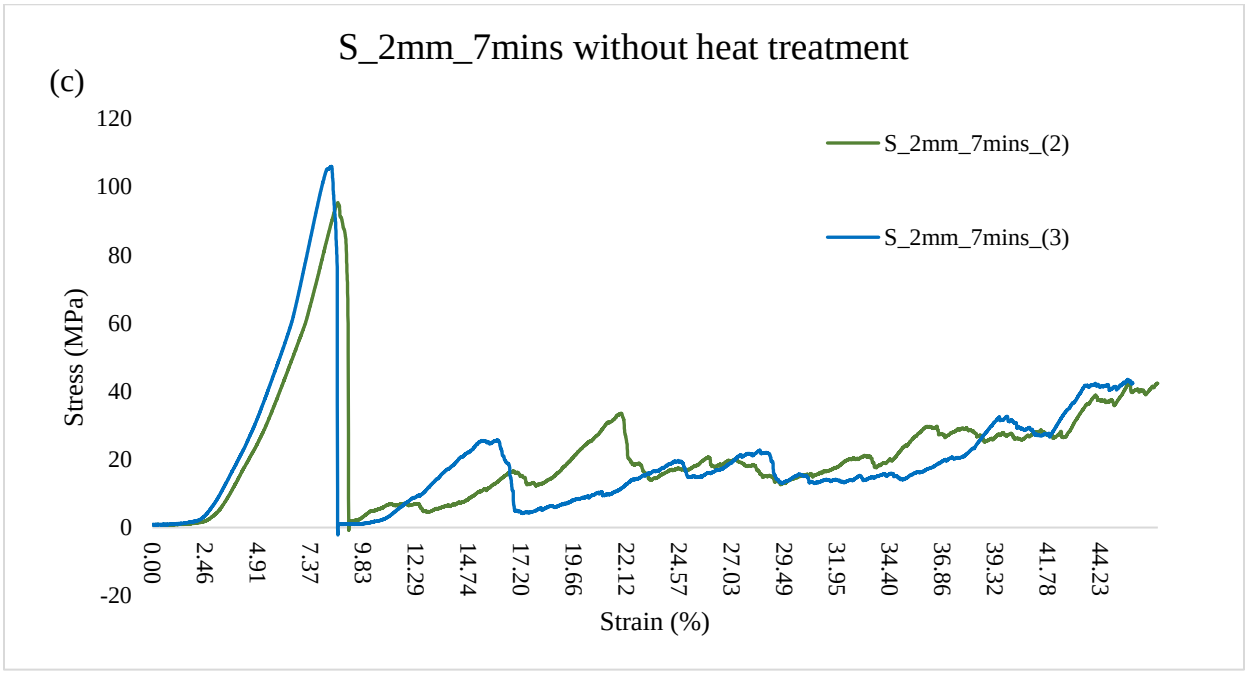

Figure 35. Stress-strain curves without post-processing heat treatment for uncoated and PEO coated scaffolds; (a) S_2mm, (b) S_2mm_5mins, (c) S_2mm_7mins, (d) S_3mm, (e) S_3mm_5mins, and (d) S_3mm_7mins (Continue on next page).

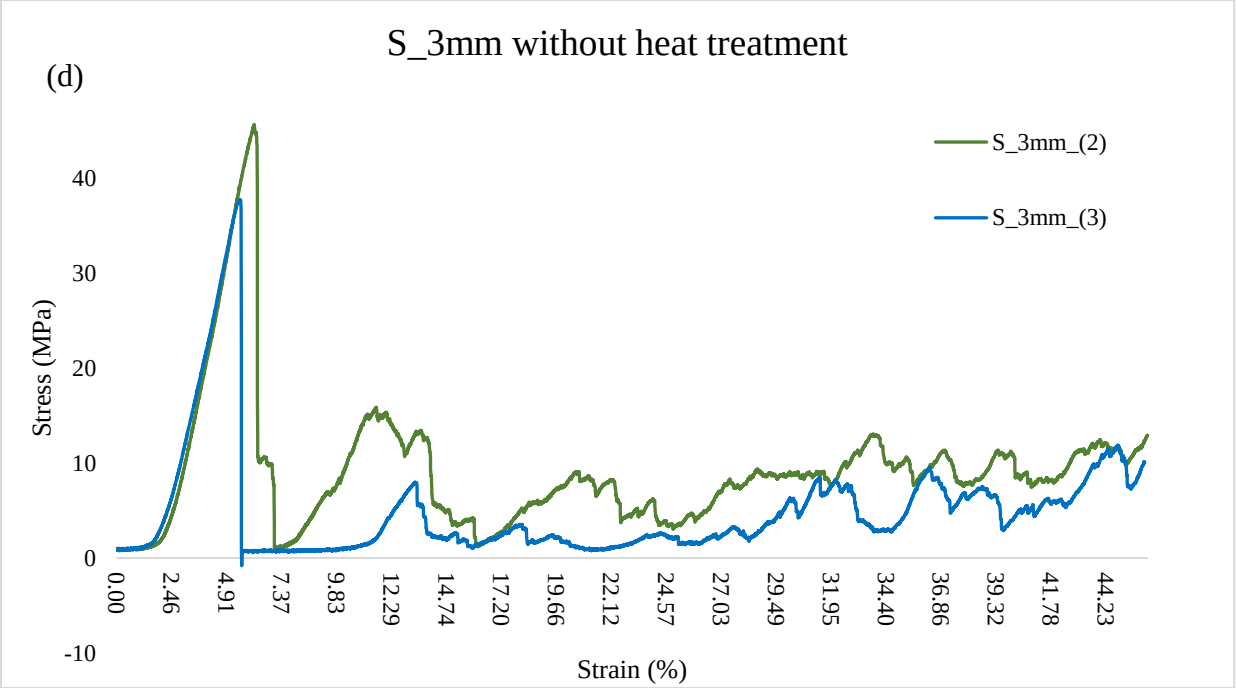

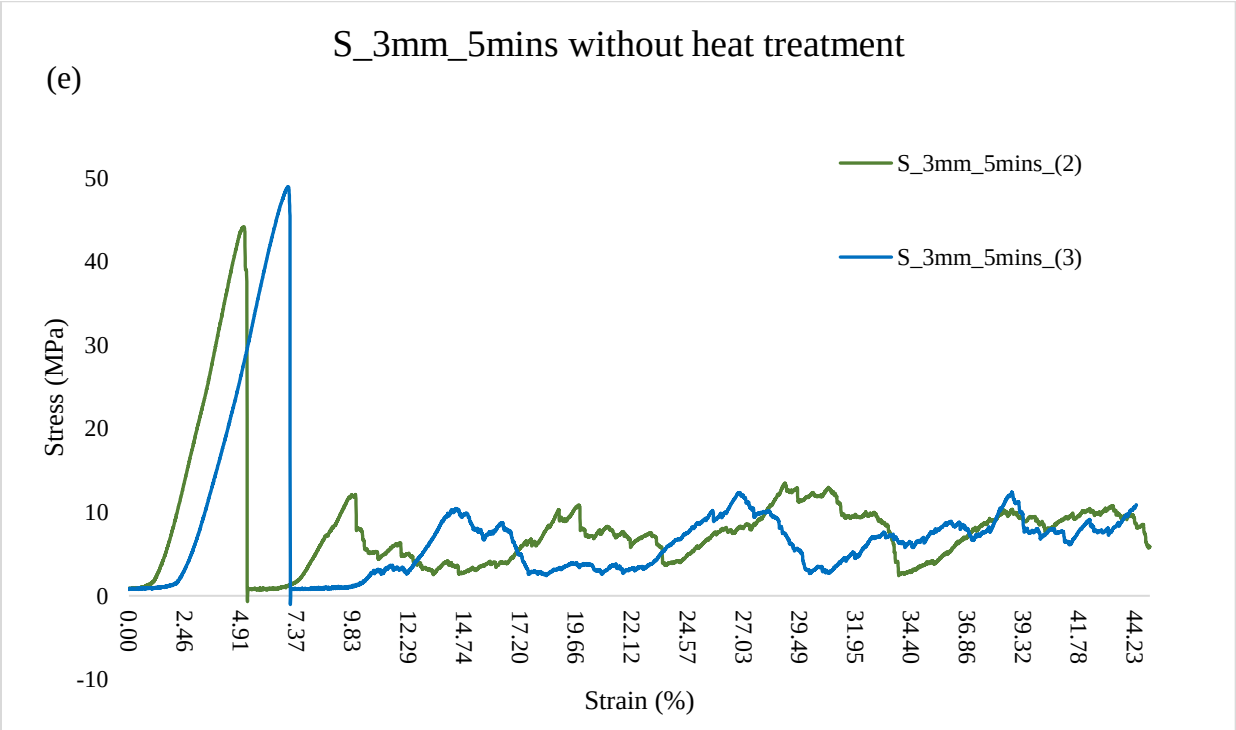

Figure 35. Stress-strain curves without post-processing heat treatment for uncoated and PEO coated scaffolds; (a) S_2mm, (b) S_2mm_5mins, (c) S_2mm_7mins, (d) S_3mm, (e) S_3mm_5mins, and (d) S_3mm_7mins (Continue on next page).

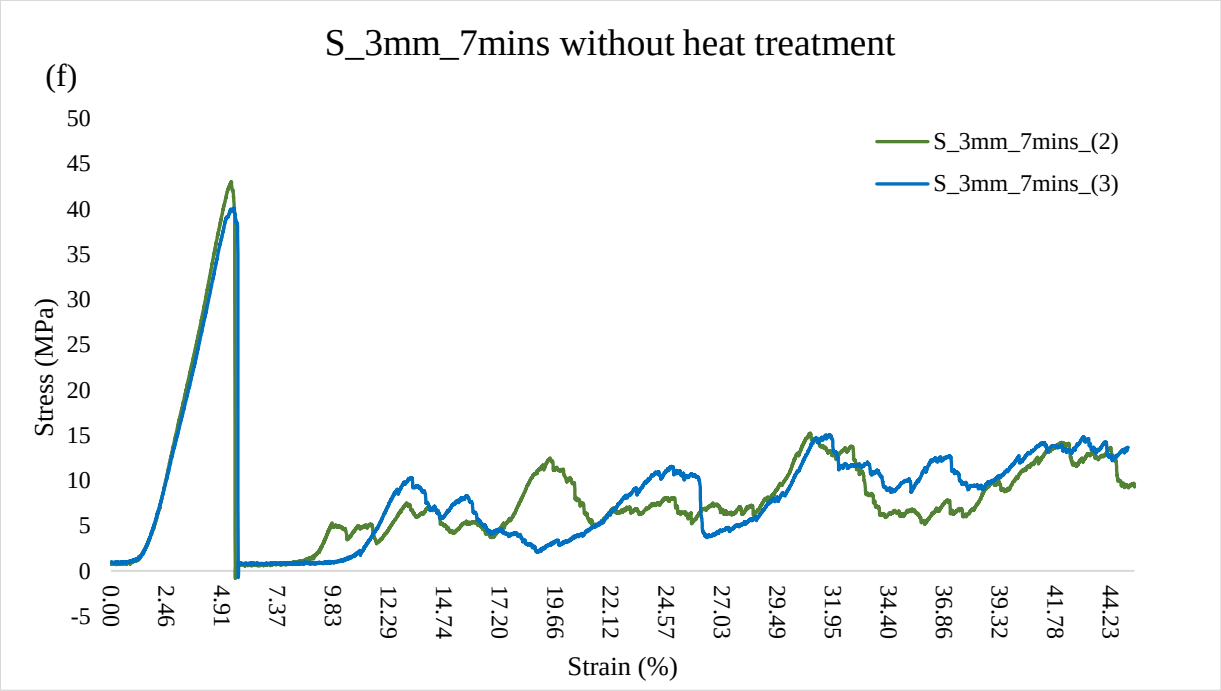

Figure 35. Stress-strain curves without post-processing heat treatment for uncoated and PEO coated scaffolds; (a) S_2mm, (b) S_2mm_5mins, (c) S_2mm_7mins, (d) S_3mm, (e) S_3mm_5mins, and (d) S_3mm_7mins.

Figure 36 reveals the average maximum stress of as-manufactured scaffolds and PEO-treated scaffolds with and without heat treatment. Ideally, as-manufactured scaffolds have inferior mechanical properties for instances lower maximum stress, quasi-elastic gradient and energy absorption compared to PEO treated scaffolds, however in this study, S_2mm exhibits higher maximum stress compared to S_2mm_5mins and S_2mm_7mins. The behavior is consistent for both categories of scaffolds, with and without heat treatment. Yet, the PEO-treated scaffolds for lower density scaffolds (S_3mm_5mins and S_3mm_7mins) are able to bear higher maximum stress at the early stages of deformation compared to the as-manufactured scaffold (S_3mm) is consistent with a previous study [44].

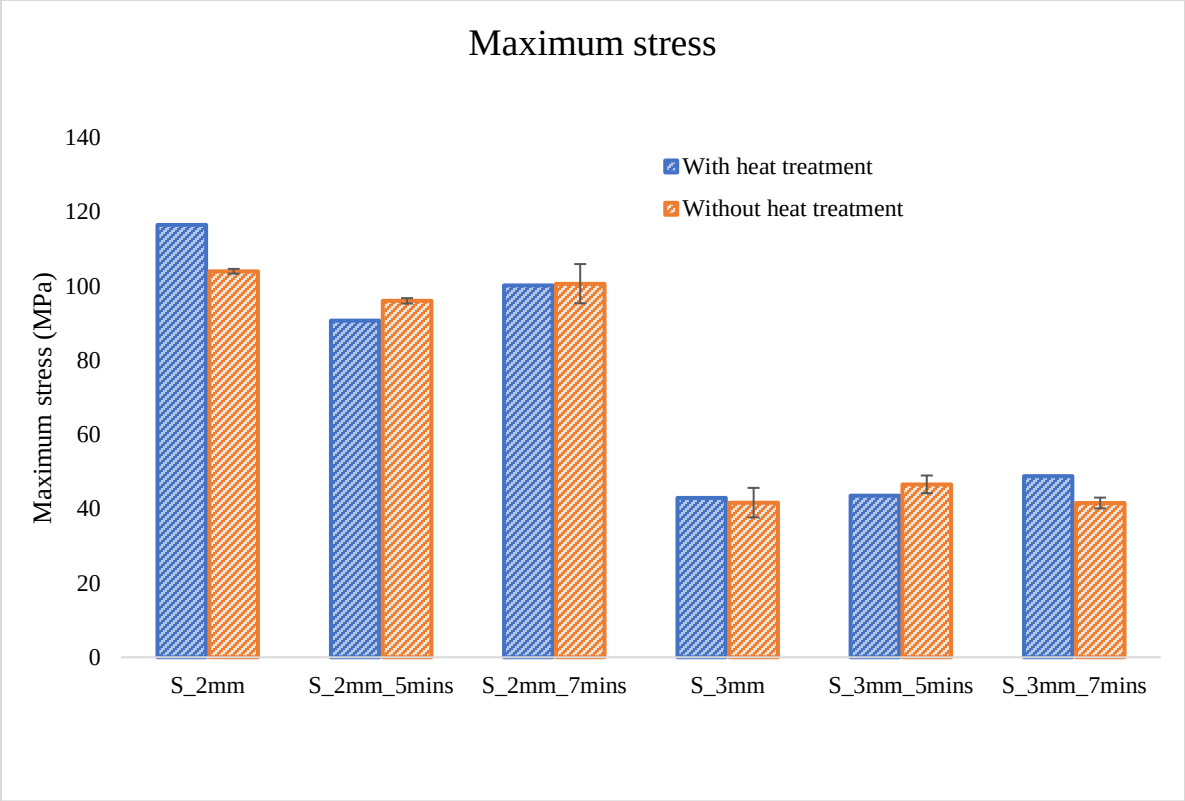

Figure 36. Maximum stress of scaffolds with and without post-processing heat treatment.

The quasi-elastic gradient of as-manufactured scaffolds and PEO treated scaffolds with and without heat treatment are depicted in Figure 37. Under quasi-static loading, the longer the treatment time of PEO process, the higher the quasi-elastic gradient value which is consistent with a previous study [44]. Heat-treated scaffolds depict a higher value of quasi-elastic gradient compared to without heat treatment scaffolds. Subsequently, PEO treatment causes the increase of quasi-elastic gradient value especially for heat-treated S_2mm scaffold when its quasi-elastic gradient 16.27 MPa increase to 21.98 MPa after 5 minutes treatment time (S_2mm_5mins with heat treatment) – an increment of 5.71 MPa. Moreover, a longer treatment of 7 minutes elevates the quasi-elastic gradient to 24.42 MPa for S_2mm_7mins with heat treatment– an increment of 2.44 MPa. In comparison, longer treatment does not substantially affect S_3mm_7mins with heat treatment – the increment from 5 minutes to 7 minutes is only 0.65 MPa. Larger pores allow easier

heat transfer, thus the scaffolds were annealed and sintered with lower temperature which eventually leads to a minor impact on mechanical properties of the scaffolds [44]. Reaching substantially improved elastic moduli in scaffolds especially for smaller pore scaffolds with different oxidation times indicates that the elastic modulus is more responsive to the formation of the PEO oxide layer.

The scaffolds without heat treatment, however, exhibit lower mechanical properties in this case quasi-elastic gradient. The behavior of S_2mm, S_2mm_5mins and S_2mm_7mins are consistent whereby the value decreases after 5 minutes of PEO treatment are applied and increase again after 7 minutes of PEO treatment. While S_3mm, S_3mm_5mins and S_3mm_7mins show a minor increase trend as the treatment time increase. Quasi elastic gradient could represent the elastic modulus of the scaffolds and all scaffolds pose the elastic modulus that is concordant with human cancellous bone. All values were found within the range of the elastic moduli for human cancellous bone tissue (10 to 1570 MPa) [105,106].

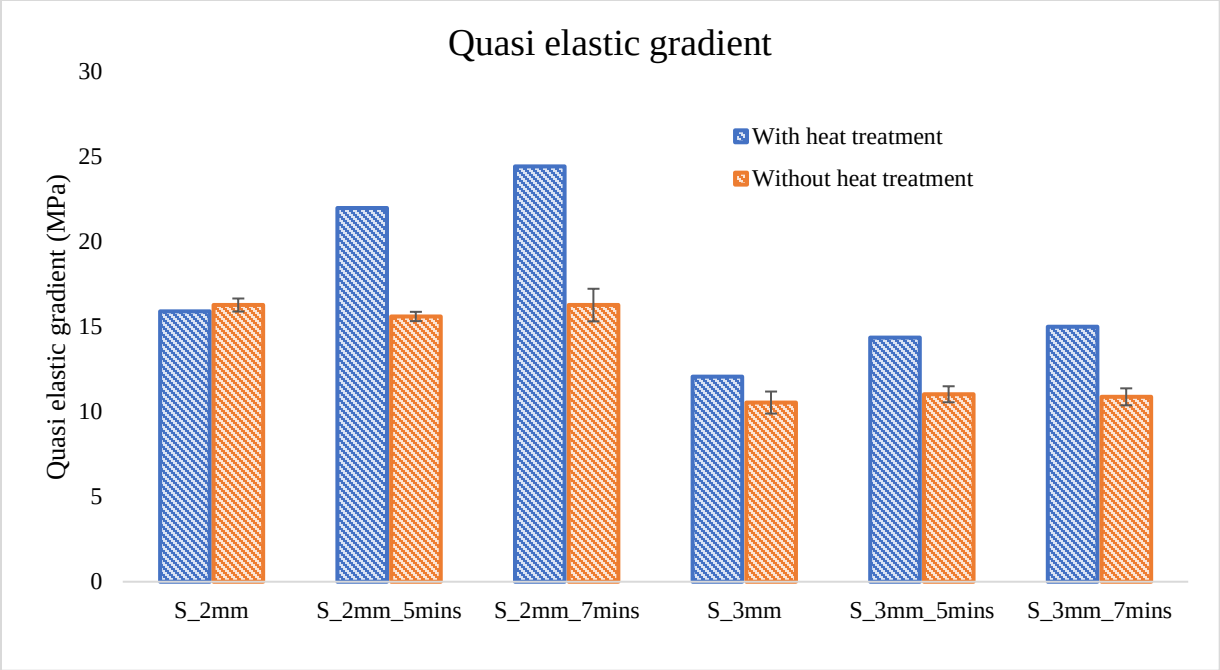

Figure 37. Quasi elastic gradient of scaffolds with and without post-processing heat treatment.

In order to get insights into the toughness of porous scaffolds, the energy absorption was calculated for each scaffold, as shown in Figure 38 and Figure 39. The energy absorption is defined by the area under the stress-strain curve by

$$W = \frac{1}{100}\int_0^{e_0} \sigma de$$

where W is the energy absorption per unit volume, σ is the compressive stress and e_0 is the upper limit of the compressive strain. Increased porosity percentage is expected to degrade the energy absorption due to the lower maximum stress and stress fluctuation region for this study.

Energy absorption of PEO-treated scaffolds with heat treatment was calculated (Figure 38) and the finding suggests that PEO enhances the toughness of the scaffolds notably with smaller pore size. The energy absorption of S_2mm_5mins is 15.18 MJ/m^3 and increases to 19.29 MJ/m^3

after 7 minutes of PEO treatment. The energy absorption of S_3mm_5mins is 6.45 MJ/m^3 and slightly increase to 7.86 MJ/m^3 after 7 minutes of PEO treatment.

For scaffolds without heat treatment (Figure 39), S_3mm (3.37 MJ/m^3) exhibits a significantly different ability of absorbing energy to S_2mm (10.49 MJ/m^3) with almost threefold increment. The prolonged PEO treatment from 5 minutes to 7 minutes increases the energy absorption for S_3mm_5mins and S_3mm_7mins; the difference between S_3mm_5mins and S_3mm_7mins is 0.33 MJ/m^3. In contrast, longer PEO treatment time barely reduces the energy absorption for S_2mm_5mins and S_2mm_ 7mins with a difference of 1.33 MJ/m^3. The pattern of energy absorption of heat-treated scaffolds exhibits the better ability of absorbing energy compared to inconsistent behavior of without heat treatment scaffolds.

The energy absorption ability of porous structure may play a notable role for bone replacement as the bone is always subjected to cyclic load, the energy absorptive properties are essential to protect bone and articular cartilage from deformation [107]. Additionally, the unit cell, geometry, relative density, the properties of base material and the loading rate would decide the energy absorption ability of porous structure [108]. Hence, in this study, S_2mm_7mins with heat treatment outperform others scaffolds for energy-absorbing application.

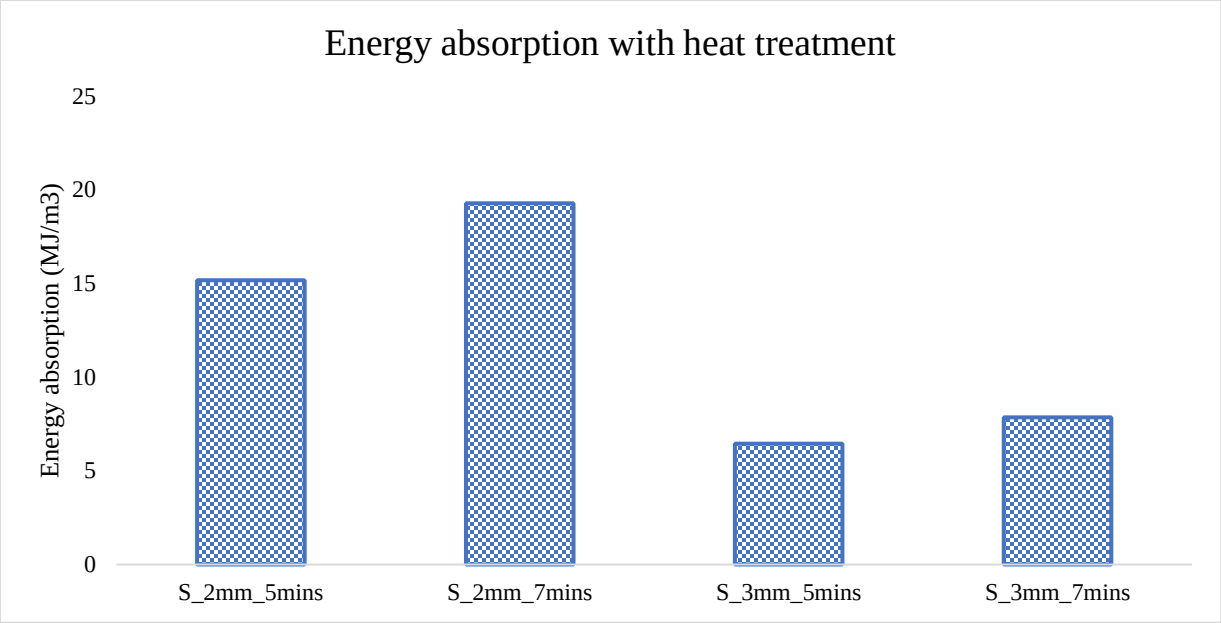

Figure 38. Energy absorption of scaffolds treated with post-processing heat treatment.

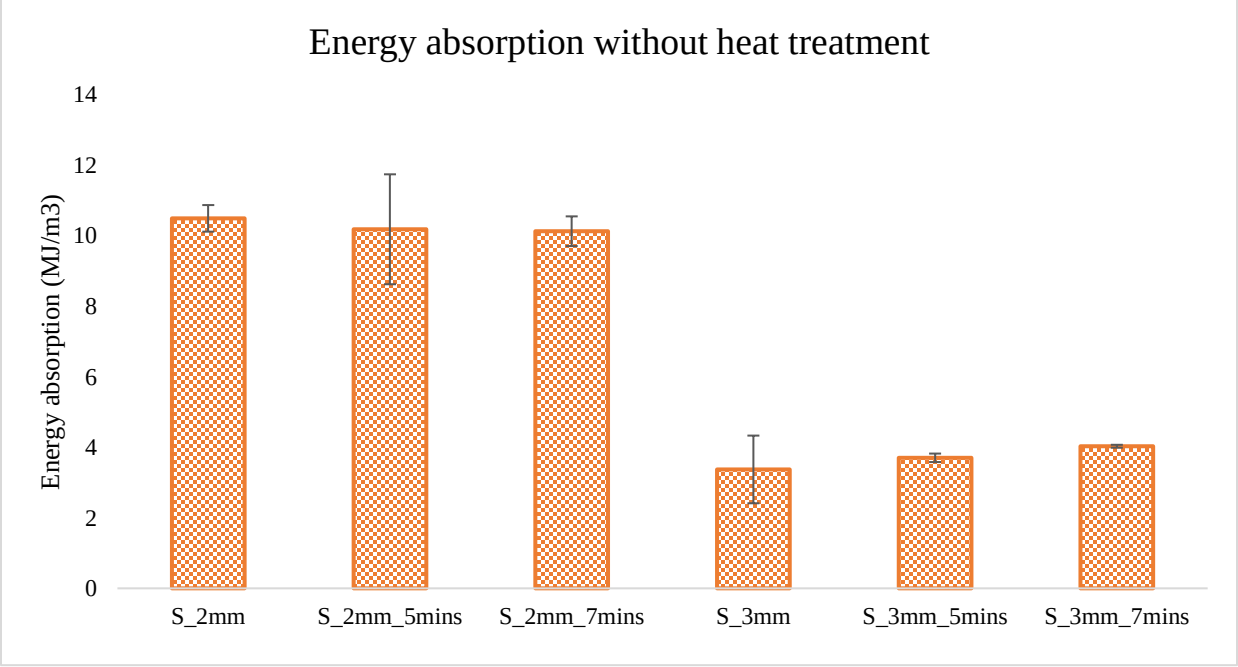

Figure 39. Energy absorption of scaffolds that did not treat with post-processing heat treatment.

Table 8. Summary of mechanical properties of scaffolds with and without post-processing heat treatment.

Scaffolds	Mechanical properties		
	Maximum stress (MPa)	**Quasi elastic gradient (MPa)**	**Energy absorption (MJ/m^3)**
With heat treatment			
S_2mm	116.46	15.91	-
S_2mm_5mins	90.66	21.98	15.18
S_2mm_7mins	100.19	24.42	19.29
S_3mm	42.92	12.06	4.46
S_3mm_5mins	43.55	14.36	6.45
S_3mm_7mins	48.82	15.01	7.86
Without heat treatment			
S_2mm	103.10 ± 0.64	16.28 ± 0.38	10.49 ± 0.38
S_2mm_5mins	96.02 ± 0.73	15.60 ± 0.27	10.18 ± 1.56
S_2mm_7mins	100.64 ± 5.30	16.27 ± 0.96	10.13 ± 0.42
S_3mm	41.66 ± 3.98	10.54 ± 0.65	3.37 ± 0.96
S_3mm_5mins	46.59 ± 2.39	11.03 ± 0.47	3.70 ± 0.12
S_3mm_7mins	48.82 ± 1.46	10.88 ± 0.50	4.03 ± 0.04

Studies have confirmed that Ti6Al4V part manufactured by SLM technology depicted the presence of a martensitic structure comprised of an α phase and β phase at grain boundaries [109–115]. Table 8 summarizes the results obtained from the compression test for all sets of scaffolds. Hence, the SLM-manufactured part usually displays limited ductility as shown in this study. Heat treatment has a substantial effect on the mechanical properties of titanium alloy prepared by SLM for better performance in structural applications [116]. Furthermore, post-processing heat treatment poses a positive effect on reducing the number of pores formed in the structure and

partially melted powder, eventually ameliorate homogeneity of the structure [117]. The effect of high temperature from heat treatment of post-processing and PEO process in this study is not comparable due to significant temperature difference; heat treatment of post-processing is 935°C while PEO treatment is approximately 53°C. Yet, PEO treatment slightly contributes to the minor improvement of the mechanical properties of SLM-manufactured porous scaffolds. This study suggests that to have better homogeneity mechanical properties, post-processing heat treatment should be applied on the scaffolds before conducting PEO treatment.

4.4 SUMMARY

In this second phase, SLM-manufactured porous scaffolds with two different porosity percentages were treated through the PEO process for two different treatment time. The deposition of the bio-functional coating on the porous scaffold through PEO treatment is feasible and exhibits different behavior according to the size of pores. Regarding electrical response, four different stages involved in the process with distinct patterns compared to plate substrate. TiO_2, tricalcium phosphate, HAp and FAp were found in the coating layer. The characterization of pore morphology demonstrates that the size of pore could be related to the spark discharging intensity during the PEO process.

PEO treatment slightly altered the mechanical properties (quasi elastic-gradient, maximum stress and energy absorption) of the scaffolds, this is in agreement with a previous study conducting by Karaji et al. [44]. Higher porosity percentage scaffolds exhibit lower mechanical performance compared to lower porosity percentage scaffolds, yet the strength is still comparable to human cancellous bone tissue. S_2mm_7mins outperforms others scaffolds in term of mechanical properties. Post-processing heat treatment ameliorates the ductility of SLM-manufactured scaffolds. In practice, post-processing with heat treatment is necessary before applying PEO

treatment to achieve better mechanical properties and relieve residual stresses developed during SLM process. Future work shall investigate better unit cell design that would allow the homogeneous deposition of PEO coating from periphery to the middle of the scaffolds and able to bear cyclic loading for long lifespan performance.

CHAPTER 5: EVALUATION OF APATITE FORMATION ABILITY OF TI6AL4V PLATE AND SELECTIVE LASER MELTED POROUS SCAFFOLD COATED WITH PEO COATING LAYER

5.1 INTRODUCTION

In general, the in vivo bioactivity of biomaterial could be explained by bone-bonding mechanisms. It involves five stages where the first two stages could be mimicked by an in vitro solution with an ion concentration almost equal to human blood plasma to predict the ability of bone tissue to interlock onto the surfaces of biomaterial. The five stages of the bioactivity mechanisms of biomaterials related to the bone application are: the reduction of homeostatic pH at the implant/bone interface environment, the dissolution of calcium and phosphate ions from the biomaterial and concurrent apatite formation as a foothold of bone-bonding on the material surface, the generation of the extracellular matrix, the mineralization of collagen fibrils, apatite and the reinforcement of bone fixation at the bone/implant interface by mineralized collagen [118–120]. The aim of this chapter is to investigate the apatite formation ability of PEO coating formed on the surface of Ti6Al4V plate and Ti6Al4V additively manufactured porous scaffolds.

5.2 MATERIALS AND METHODS

5.2.1 SIMULATED BODY FLUID IMMERSION TEST

In vitro bioactivity of coated substrates was determined by evaluating the apatite-forming ability. Static simulated body fluid was used as a soaking solution with an ionic composition almost equal to human plasma. The solution was prepared according to the protocol by Kokubo et al. [121] by dissolving reagents of NaCl, $NaHCO_3$, KCL, K_2HPO_4. $3H_2O$, $MgCl_2.6H_2O$, $CaCl_2$, Na_2SO_4 and $(HOCH_2)3CNH_2$ with 1000 mL in instructed order (Table 9). Figure 40 shows the setup to prepare the SBF solution. Tris-HCL (Tris-hydroxymethyl aminomethane—hydrochloric

acid) served as a buffer to maintain a constant pH value of 7.4 at 36.5 ± 0.5 °C. For Ti6Al4V plate substrates, uncoated substrates (control samples) and coated substrates were immersed in 30 mL of SBF for 14 and 28 days in an incubator at a constant temperature of 37 °C. The procedure for SLM-fabricated porous scaffolds was slightly modified. Uncoated porous scaffolds and coated scaffolds were immersed in 30 mL of SBF for 28 days and the solution was changed daily to maintain the ions concentration throughout the immersion period. After various immersion times, the substrates were washed thoroughly with distilled water and allowed to dry at room temperature. Dried immersed substrates were kept in a desiccator before surface characterization.

Table 9. The reagents are required to prepare Kokubo SBF solution.

Order	**Reagent**	**Amount**
1	Sodium chloride (NaCl)	8.035 g
2	Sodium hydrogen carbonate ($NaHCO_3$)	0.355 g
3	Potassium chloride (KCl)	0.225 g
4	Di-potassium hydrogen phosphate trihydrate ($K_2HPO_4.3H_2O$)	0.231 g
5	Magnesium chloride hexahydrate ($MgCl_2.6H_2O$)	0.311 g
6	1M (mol/l) Hydrochloric acid, 1.0M-HCL	39ml
7	Calcium chloride ($CaCl_2$)	0.292 g
8	Sodium sulfate (Na_2SO_4)	0.072
9	Tris-hydroxymethyl aminomethane: ($(HOCH_2)_3CNH_2$) (Tris)	6.118 g
10	1M (mol/l) Hydrochloric acid, 1.0M-HCL	0 – 5 ml

Apatite formation on surfaces of SBF immersed was characterized by FESEM, EDS and XPS. The morphologies were observed by FESEM and chemical compositions of dispersed apatite on the coating surfaces were examined by EDS and XPS. The FESEM images of apatite deposited on the coating surfaces were examined by ImageJ software to investigate the coating characteristics such as pore population and pore sizes.

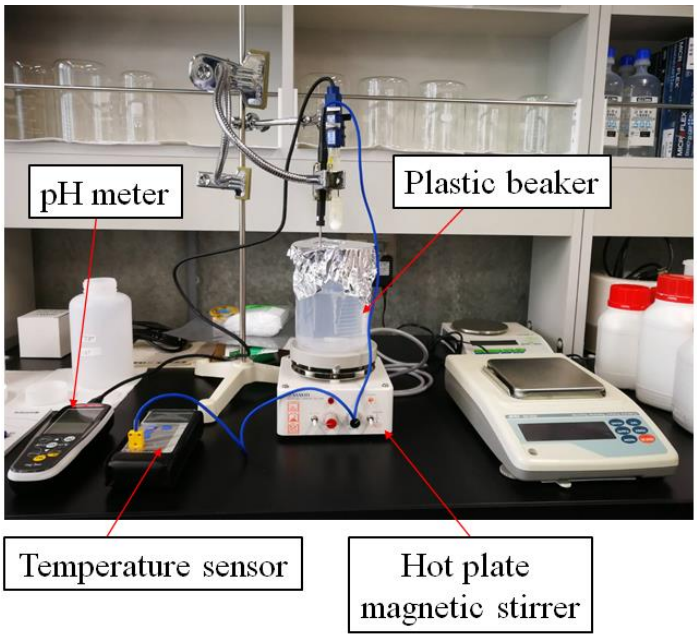

Figure 40. The set up to prepare SBF solution.

5.2.2 CHARACTERIZATION OF APATITE FORMATION ON THE COATING SURFACE

Similar FESEM-EDS, XRD and ImageJ software that were used to characterizing PEO coating were used to investigate the apatite formation on the coating layer and the details have been described in section 3.2.3.1 and 3.2.3.2. In addition, similar XPS that were used to characterize chemical elements in coating layer of porous scaffolds was used and the details also have been described in section 4.2.3.1.

5.3 RESULTS AND DISCUSSION

5.3.1 TI6AL4V PLATE SUBSTRATE

To evaluate the apatite formation ability of the coating, a static SBF immersion test was performed for two distinct immersion periods (14 days and 28 days). After the immersion test was completed, the morphologies of the apatite formed on the coating were analyzed by FESEM as shown in Figure 41. The size range of apatite formed on the coating surface was analyzed by ImageJ as shown in Table 10. We observed that the white flocculent products were present for both coating surfaces with different immersion periods. After 14 days of immersion in SBF solution, the flocculent apatite was randomly dispersed, especially around the edges of micropores on the surface coating with a size range of 0.098~0.237 μm^2 (Figure 41b). Larger size of flocculent conglomerates could be seen for the SBF-immersed substrate of 28 days with a size range of 0.258~1.093 μm^2 generated on the coating surface as shown in Figure 41d. Measurement of the Ca/P ratio of these two SBF-immersed substrates is revealed by EDS analysis (Table 11). SBF-immersed coated substrates exemplify a slightly lower Ca/P ratio compared to the coated substrate before the SBF immersion test as discussed earlier. These differences resulted from the partial dissolution process of tricalcium phosphate, HAp and FAp from the coating layer to upsurge the concentration of Ca^{2+} and PO_4^{3-} in the solution environment which eventually provoked the nucleation and precipitation of apatitic crystallization while merging with carbonate, hydroxyl and various cations from the SBF solution [120,122]. Therefore, the biomaterial for orthopedic application is necessary to have the ability to marginally dissolve to induce the apatite formation which will promote the chemical bond with the host bonny tissue. Uncoated Ti6Al4V substrates were immersed for 14 days and 28 days as well and they act as control samples to ascertain the Ti alloys could not activate any apatite nucleation on the surface. FESEM-EDS analysis upheld that

uncoated Ti alloy could not provoke any apatite formation where Ca and P elements could not be detected, hence it confirmed that bio-functional coating would strengthen the bone-bonding mechanism between the implant and the adjacent bone tissue.

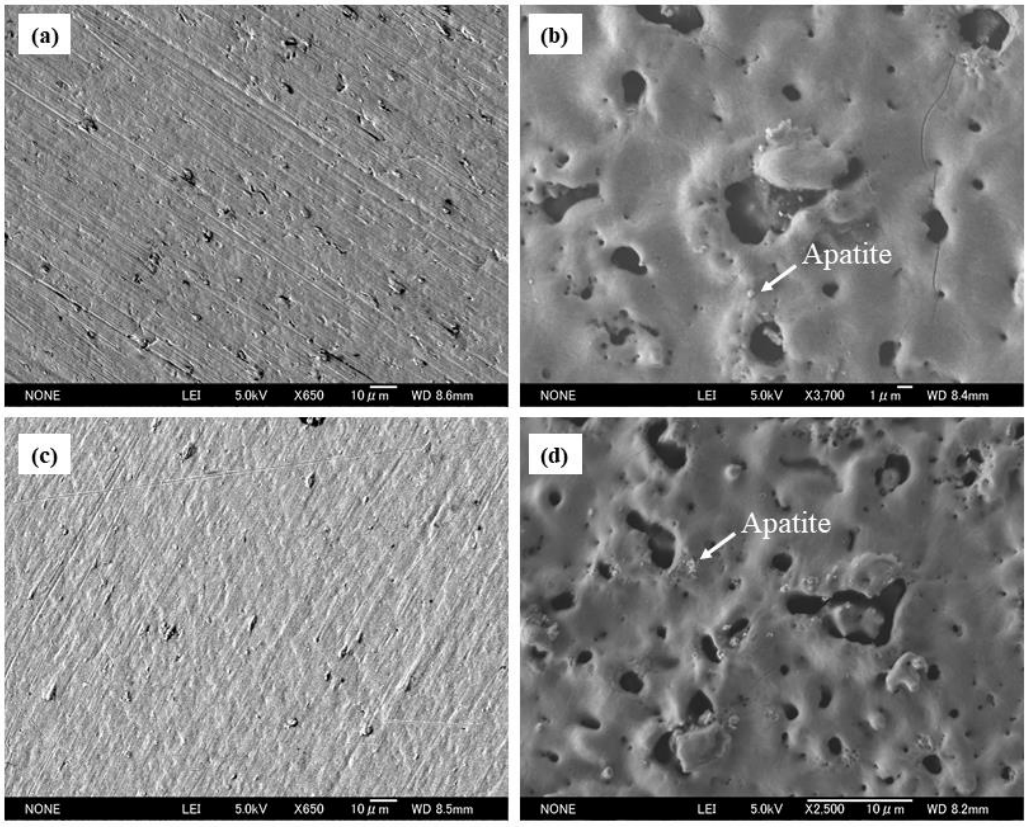

Figure 41. Morphologies of apatite formed after SBF immersion test: (a) uncoated Ti6Al4V immersed for 14 days (control sample), (b) coated Ti6Al4V immersed for 14 days, (c) uncoated Ti6Al4V immersed for 28 days (control sample), and (d) coated Ti6Al4V immersed for 28 days.

Table 10. Apatite sizes and Ca/P ratio at post-immersion in SBF.

Apatite formed properties	**14 days**	**28 days**
Size range of apatite (μm^2)	0.098~0.237	0.258~1.093
Ca/P ratio	1.296	1.294

Table 11. EDS spectra results for SBF immersion test of uncoated and coated substrates.

Element	**14 days**				**28 days**			
	Uncoated		**Coated**		**Uncoated**		**Coated**	
	Wt%	**At%**	**Wt%**	**At%**	**Wt%**	**At%**	**Wt%**	**At%**
Ca	-	-	0.46	0.25	-	-	0.98	0.60
P	< 0.42	< 0.73	5.51	3.87	< 0.51	< 0.94	5.57	4.43
Ti	98.00	94.69	34.96	15.87	99.49	99.06	47.48	24.42
O	1.58	4.58	57.82	78.58	-	-	44.95	69.22
F	-	-	1.25	1.43	-	-	1.02	1.33

The phase compositions of the SBF post-immersion PEO coating and titanium substrates were investigated by XRD, as shown in Figure 42 a,b. The XRD pattern of SBF post-immersion of titanium substrate shows that the crystallinity of apatite could not be found. The phases of anatase, rutile, tricalcium phosphate, HAp and FAp already existed in the coating, as shown in Figure 32, and the phases were enriched under the SBF condition after 14 days and 28 days of immersion time. The XRD pattern for titanium substrate indicated that the Ti6Al4V substrate could not induce apatite formation on the surface while PEO-coated titanium with bio-functional elements

spontaneously allow the growth of apatite on the surface. This suggests that PEO coating with HAp and FAp has good bioactivity and Ti6Al4V surface could not prompt the nucleation of HAp, thus it would delay the process of osseointegration between adjacent bone tissue and implants. The prolonged immersion time in the SBF could also enhance the formation of apatite as evidenced in Figure 42a. The increase in tricalcium phosphate, HAp and FAp compounds on the coating is the result of the reaction between the Ca^{2+} and PO_4^{3-} in SBF solution with TiO_2 and F^- in the coating during the immersion test. According to [123], the presence of FAp in the coating assists in improving the bioactivity of the coating, therefore the incorporation of fluoride elements into the coating becomes an excellent alternative for more robust orthopedic implants application.

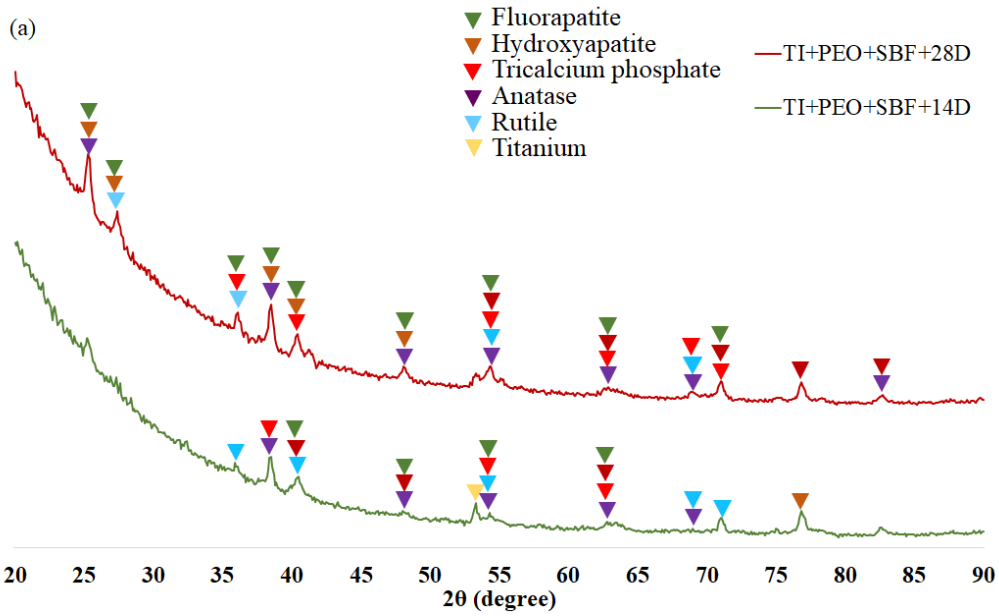

Figure 42. XRD analysis results after the SBF immersion test with two immersion times (14 days and 28 days): (a) coated Ti6Al4v plate substrate; and (b) uncoated Ti6Al4V plate substrate

(Continue on next page).

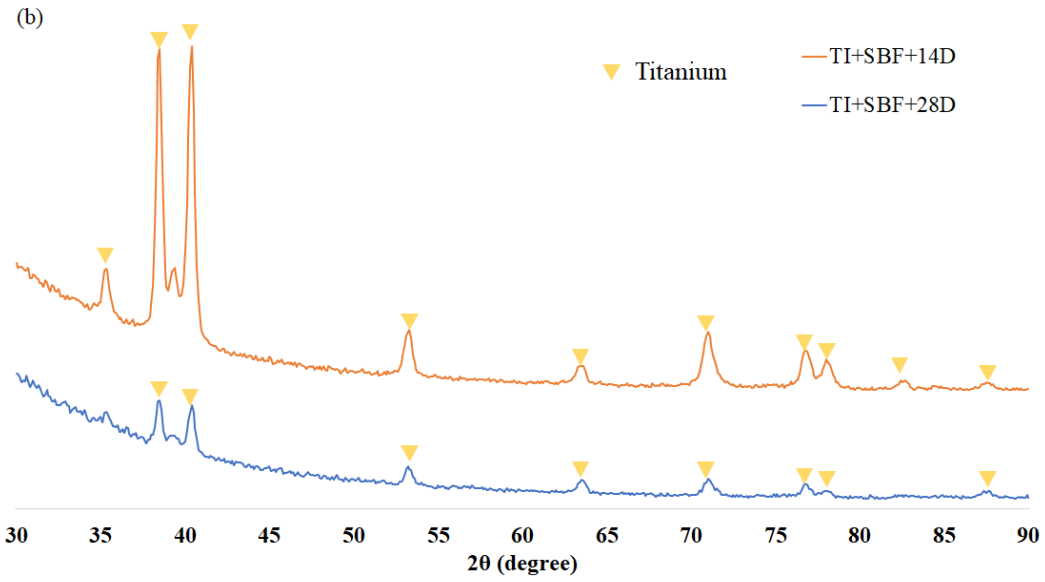

Figure 42. XRD analysis results after the SBF immersion test with two immersion times (14 days and 28 days): (a) coated Ti6Al4v plate substrate; and (b) uncoated Ti6Al4V plate substrate

5.3.2 SELECTIVE LASER MELTING MANUFACTURED TI6AL4V POROUS SCAFFOLD

The nucleation of biological apatite precipitation on the HAp ceramics coating or layer in vivo and in vitro has been extensively reported [120,124–128]. Figure 43 shows the morphology and chemical constituents of the four PEO-coated scaffolds after 28 days of SBF immersion. All PEO-coated scaffolds studied here induced the formation of apatite, determining the bioactive conformation of the PEO coating. Yet, the morphologies of the apatite are dissimilar. Thereby further indicated a difference in mechanisms of nucleation and growth of the apatite crystals as the result of different PEO-coated surface characteristics of the scaffolds. The phases of Ti, TiO_2, anatase, rutile, tricalcium phosphate, HAp and FAp have already prevailed on the surface of the PEO-coated scaffold. It has been confirmed that TiO_2 is a positively charged oxides [129]. It had been suggested the amorphous CaP could likely convert into apatite when the Ca/P ratio in the local region attains 1.67 [130].

An important finding in this SBF immersion test was the observation of different morphologies of apatite formed on the surface for each scaffold. Confluent flaky-shaped apatite formation and globular morphology apatite with some micropores around the formation can be observed on the S_2mm_5mins and S_2mm_7mins scaffolds, respectively. Apatite growth in globular aggerates with a smooth surface can be observed on the surfaces of S_3mm_5mins and S_3mm_7mins scaffolds. Micro-cracks in the apatite layer of these two scaffolds presumably due to the contraction of the porous hydrated layer when the scaffolds were dried during SBF post-immersion [131].

The micropores structure on the coating surface as shown in Figure 27 is favorable for apatite crystal growth [131–133]. The sizes of micropores of PEO coating likely influence the morphology, structure and Ca and P constituent of the apatite layer. The micropores on PEO coating of S_3mm_5mins and S_3mm_7mins exhibited larger size (refer in Figure 27) compared to S_2mm_5mins and S_2mm_7mins, thus the smooth mud-like surface formed on these coatings with higher amount of Ca and P as can be seen in Figure 43. According to a study [134], suitable pore size for the anchorage of HA nuclei prior to bone-like apatite layer growing is approximately 3 microns and S_3mm_5mins PEO-coating layer mostly covered with 2.31 μm^2 pore sizes, the closest size to 3µm. Hence, it is understandable that S_3mm_5mins contains higher Ca and P atomic % compared to others because the apatite growth favorable region is around pores [132,133]. The finding reported in a former study [134,135] which mentioned the nucleation of apatite or hydroxycarbonate apatite (HCA) commence initially on the surfaces of recessed regions and pores, fissures, or along micro cracks pre-existing in the surface before the exposure to SBF which is consistent with this theory and with our observation on the Ti6Al4V plate substrate in section 6.3.1.

According to a study by Wang et al. [136], confined space promotes the nucleation of apatite and micropores is categorized as a confined space. Wang et al. investigated the bioactivity of alkali-treated titanium plates with SBF immersion test and the apatite formation was confirmed only on the surface in contact with the curved bottom of the container. However, on the surface that was exposed to SBF no apatite nucleation could be found. Subsequently, in their thoroughgoing study [137], the apatite deposition from the SBF immersion test was concentrated in a specific V-shaped arrangement of thermally oxidized titanium specimens after 7 days immersion time. While no apatite can be observed on the external surfaces that are exposed to SBF despite 2 months' time-point. In line with a study by Sugino et al. [138], the above observations occur due to intense negative surface charges within the special gap of the V-shaped structure and/or local change to ionic concentration, thereafter lead to the rise of Ca ions concentration which eventually restricting the mobility of ions in SBF [139].

The variation in morphology also could be associated with the mechanics of the formation of bone-like apatite [140,141]; SBF solution does not furnish the sufficient of Ca and P ions for apatite nucleation. The supersaturation of Ca and P ions is low during the initial immersion time point. Therefore, the local ion concentrations on the scaffold surface could induce the apatite layer growth and the aggregates of crystal nuclei are formed. The crystal would absorb the ions from the surrounding environment and would spontaneously grow in preferential orientation (a process of heterogeneous nucleation). In most cases, the crystals heterogeneously nucleate on the bioactive surface. The preferential orientation would lead to the leaf-like crystals [142,143]. As the concentration of Ca and P ions increases the leaf-like crystals would transform into polycrystals and leaf-like crystals would disappear. Thereby, depositing coating with a higher concentration of

Ca and P ions is not only crucial for apatite formation but also a fundamental factor in polycrystals morphology [144].

Scaffolds	Apatite morphology	Chemical composition
S_2mm	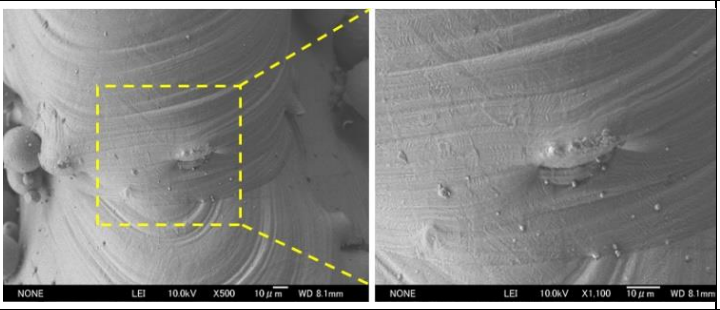	Element / Weight % / Atomic % Ti K 78.16 57.74 Al K 4.26 5.59 V K 1.34 0.93 Ca K 0.07 0.06 P K 0.09 0.10 F K - - O K 16.08 35.57 Total 100 100
S_2mm_ 5mins	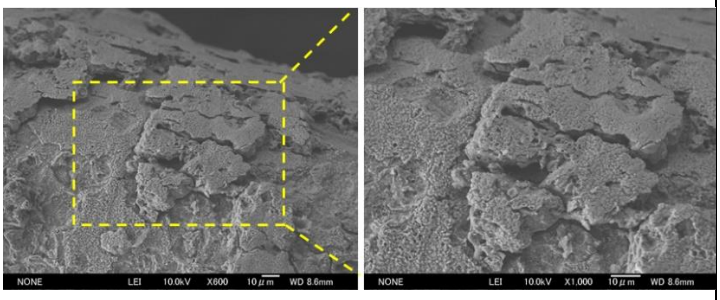	Element / Weight % / Atomic % Ti K 44.62 21.64 Al K 1.72 1.48 V K 0.06 0.03 Ca K 0.86 0.50 P K 0.26 0.20 F K 0.20 0.25 O K 52.28 75.91 Total 100 100
S_2mm_ 7mins	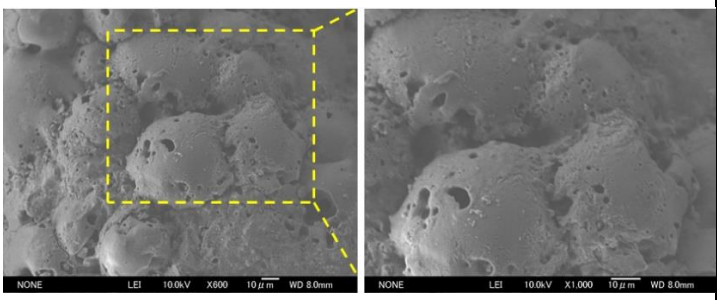	Element / Weight % / Atomic % Ti K 29.98 14.20 Al K 0.75 0.63 V K 0.03 0.01 Ca K 7.69 4.35 P K 8.90 6.52 F K 1.76 2.10 O K 50.90 72.19 Total 100 100
S_3mm	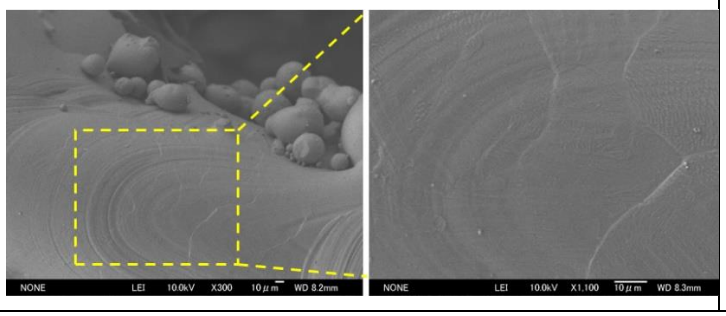	Element / Weight % / Atomic % Ti K 75.21 56.15 Al K 5.09 6.74 V K 4.53 3.18 Ca K - - P K - - F K - - O K 15.18 33.92 Total 100 100

Figure 43. FESEM images with two different magnifications of apatite formed on the scaffolds and summaries of elemental compositions consist in the apatite (Continue on next page).

S_3mm_5mins

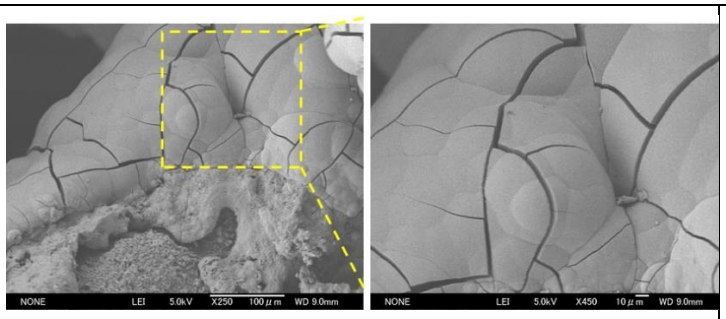

Element	Weight %	Atomic %
Ti K	1.21	0.54
Al K	-	-
V K	-	-
Ca K	27.92	14.90
P K	15.31	10.57
F K	1.38	1.55
O K	54.18	72.43
Total	100	100

S_3mm_7mins

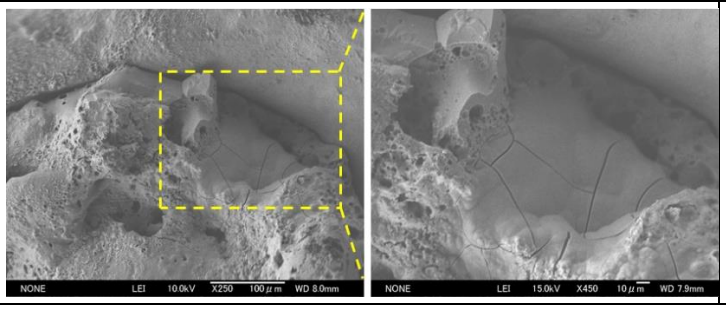

Element	Weight %	Atomic %
Ti K	13.57	6.32
Al K	0.44	0.36
V K	0.42	0.19
Ca K	20.07	11.17
P K	13.73	9.89
F K	0.64	0.75
O K	51.14	71.32
Total	100	100

Figure 43. FESEM images with two different magnifications of apatite formed on the scaffolds and summaries of elemental compositions consist in the apatite.

Figure 44 exhibits the local atomic % of Ca and P in all PEO-coated scaffolds. S_3mm_5mins and S_3mm_7mins scaffolds contain a larger atomic amount of Ca and P compared to S_2mm_5mins and S_2mm_7mins. The ionic concentrations/ constituents of Ca and P would follow a similar principle: the more closely the size of micropores to 3µm, the higher the probability for any local increases in calcium and phosphorus in the SBF, and the greater the probability for dissolution [134]. This may justify the comparatively higher constituent of these ions for S_3mm_5mins and S_3mm_7mins scaffolds. Additionally, Figure 45 and Table 12 demonstrate the Ca/P ratio of S_3mm_5mins and S_3mm_7mins scaffolds are more approaching of 1.67 Ca/P ratio of bone-like apatite.

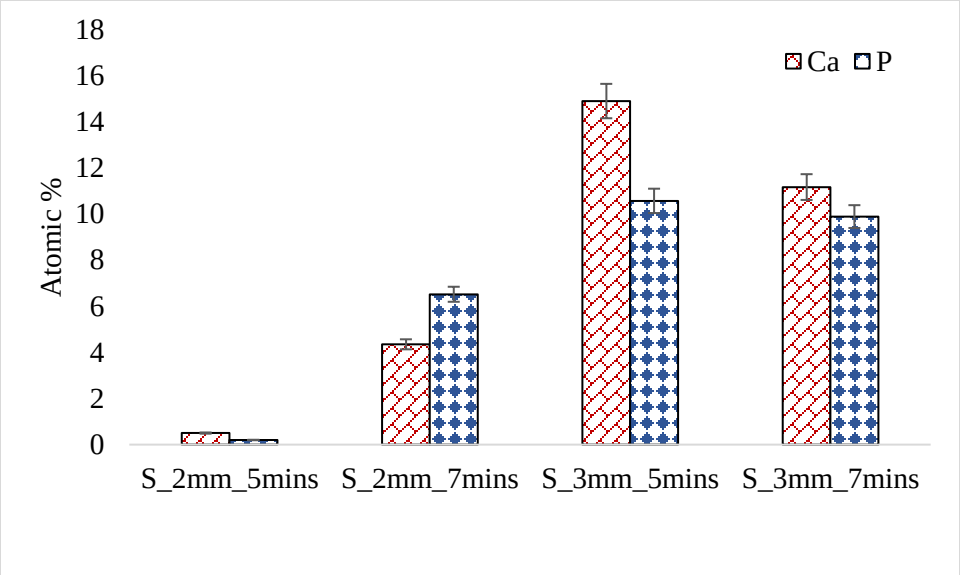

Figure 44. Atomic % of Ca and P containing in the coating layer on coated scaffolds after SBF immersion test.

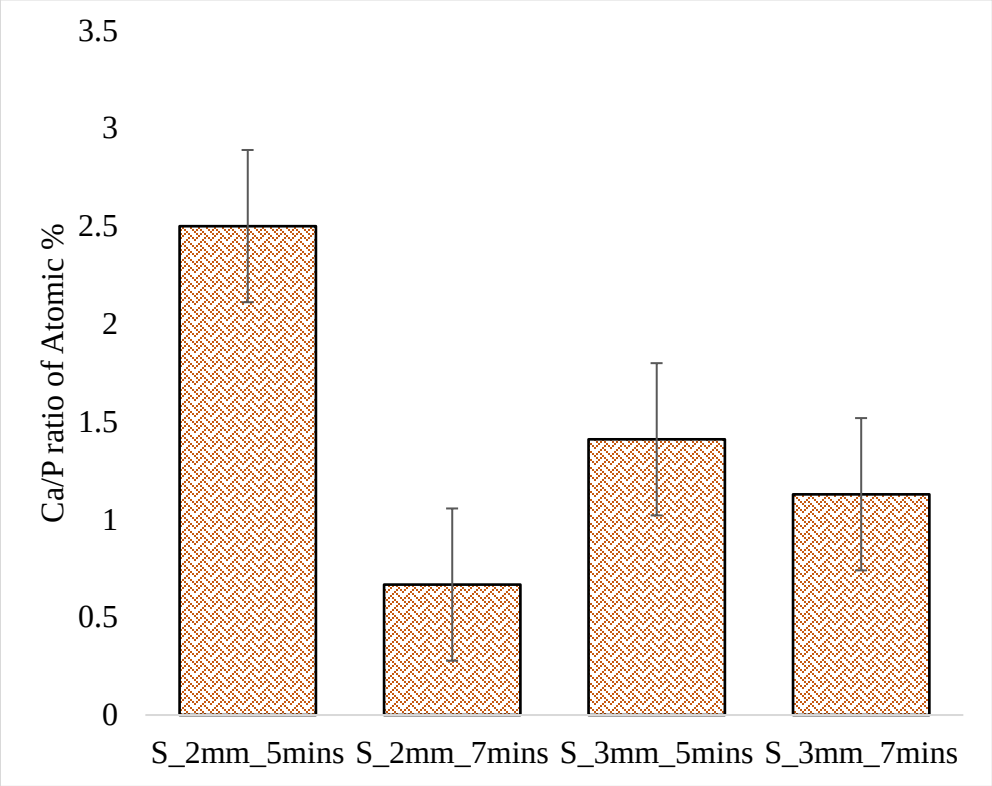

Figure 45. Ca/P ratio of atomic % for PEO-coated scaffolds after SBF immersion test.

Table 12. Summary of Ca/P ratio of atomic % for PEO-coated scaffolds after SBF immersion test.

Scaffolds	Ca/P ratio of Atomic %
S_2mm_5mins	2.50
S_2mm_7mins	0.67
S_3mm_5mins	1.41
S_3mm_7mins	1.13

As seen in Figure 46, the amount and intensity of crystalline HAp and FAp formed on the S_3mm_5mins and S_3mm_7mins scaffolds surfaces are greater than other scaffolds. The number of HAp peaks is higher for those two scaffolds as well. Thus, based on the facts explained above and local Ca and P ions concentration and the crystals formed on the surfaces, it can be inferred that the bioactivity of the S_3mm_5mins and S_3mm_7mins exhibit better bioactivity and bio-functionality.

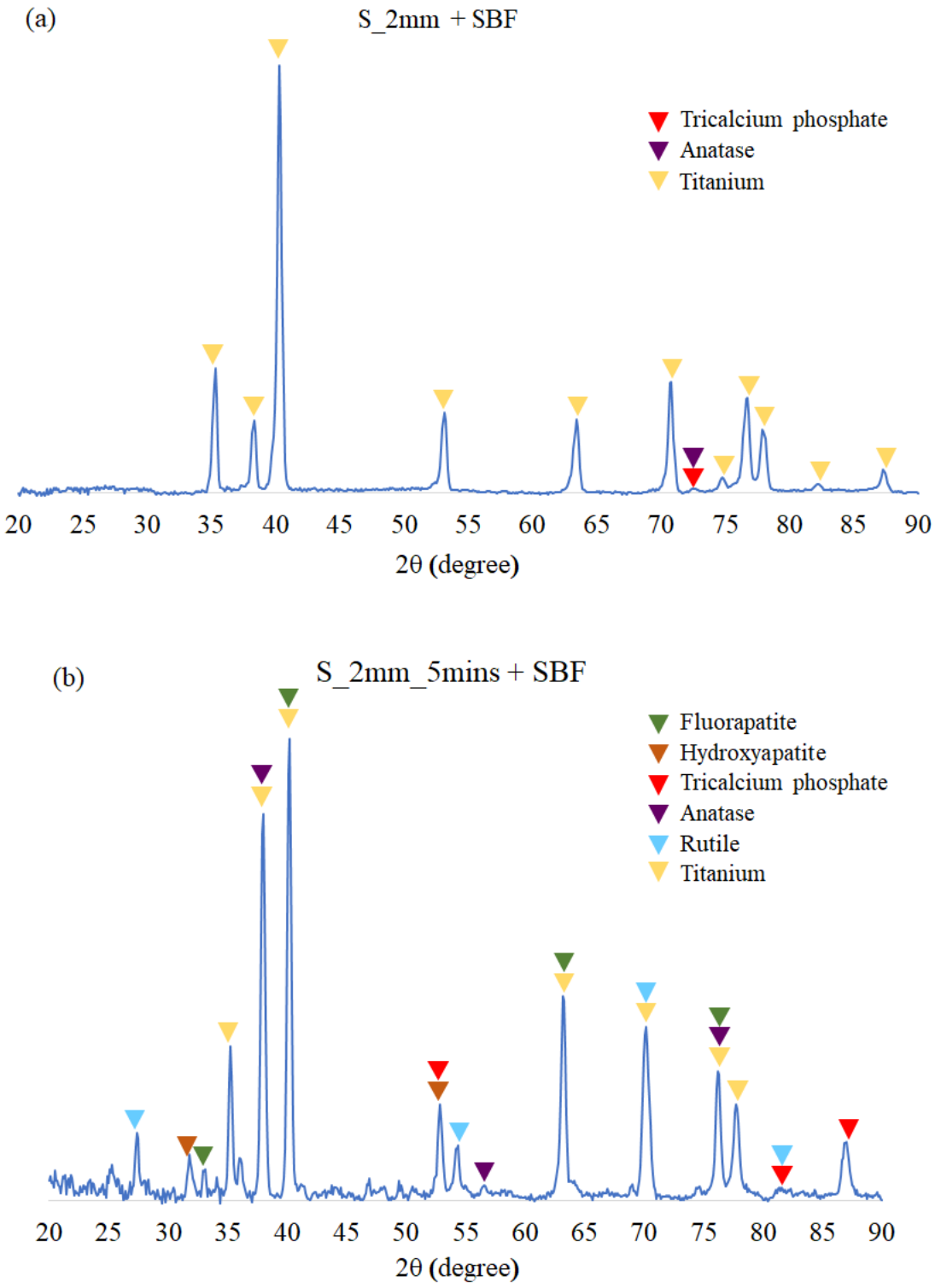

Figure 46. XRD patterns of porous scaffolds after SBF immersion test (Continue on next page).

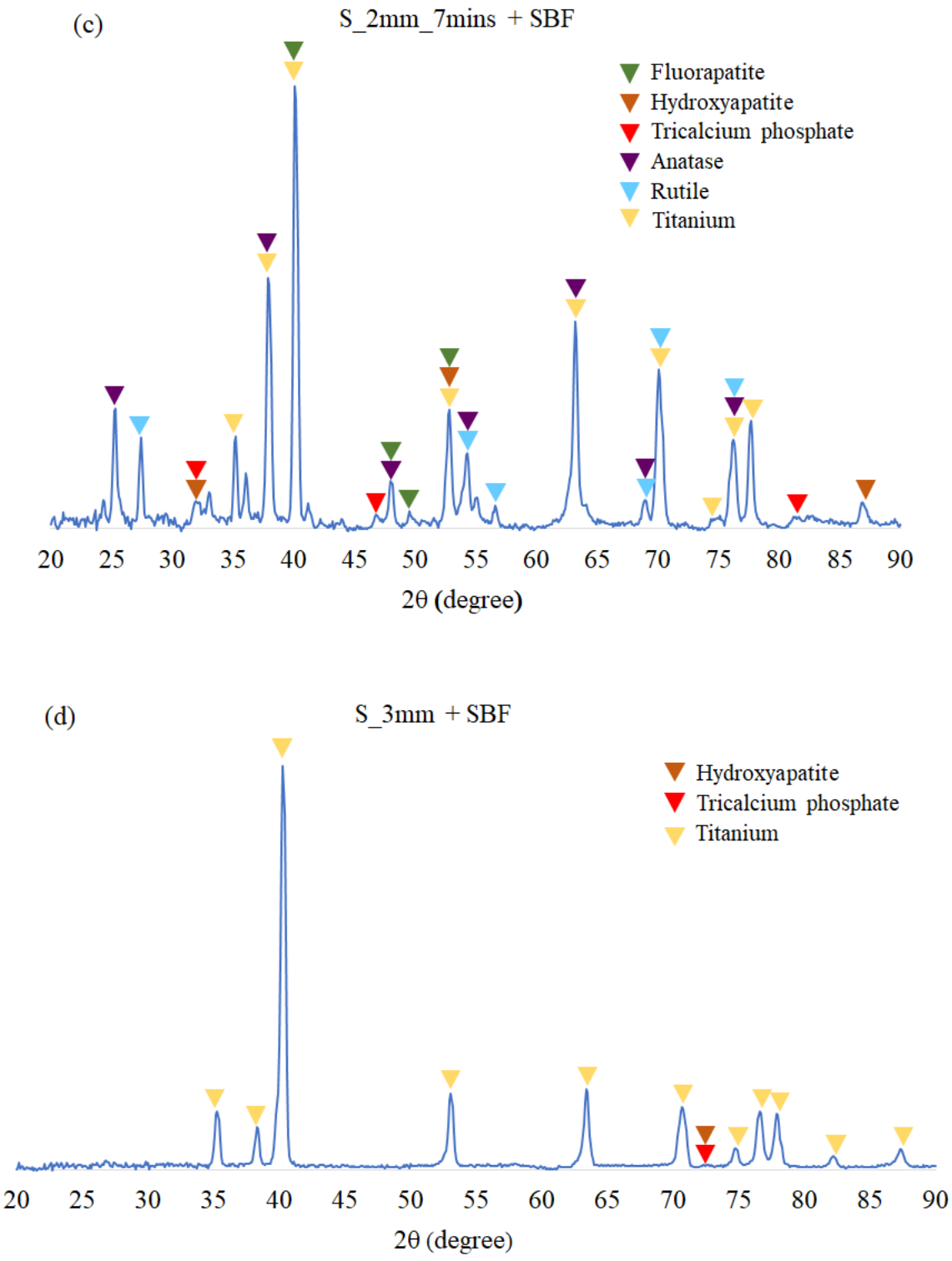

Figure 46. XRD patterns of porous scaffolds after SBF immersion test (Continue on next page).

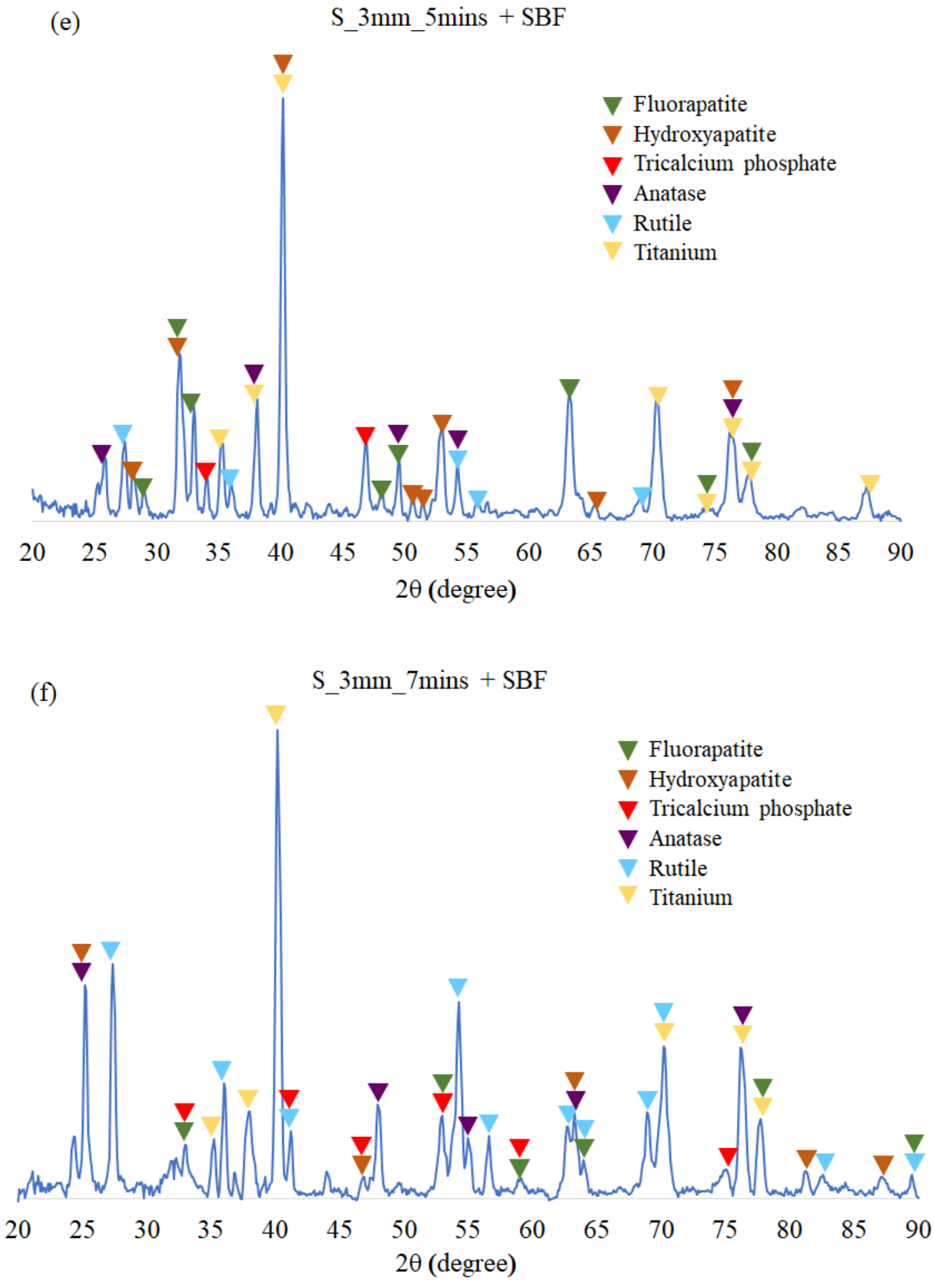

Figure 46. XRD patterns of porous scaffolds after SBF immersion test.

In order to identify the apatite formation in the composite coating, the XPS analysis of the composite coating for Ca 2p 3/2 and P 2p 3/2 was performed (Figure 47). The peaks of Ca 2p 3/2 can be observed at 350.8 eV, 351.4 eV, 351.5 eV and 350.9 eV for S_2mm_5mins, S_2mm_7mins, S_3mm_5mins and S_3mm_7mins, respectively. At the range of 134.9 to 137.5 eV, the P 2p 3/2 can be found for all PEO coated scaffolds. The O 1s spectrum with BE values within the range of 533 – 535.1 eV also can be detected in the coating after SBF immersion test. The presence of Ca 2p 3/2, P 2p 3/2 and O 1s confirms the formation of apatite groups on the coating [145–149]. On the other hand, the O 1s spectrum is in the accordance with the binding energies of TiO_2 consist in coating layer.

Scaffolds	XPS narrow wide scan
S_2mm_5mins	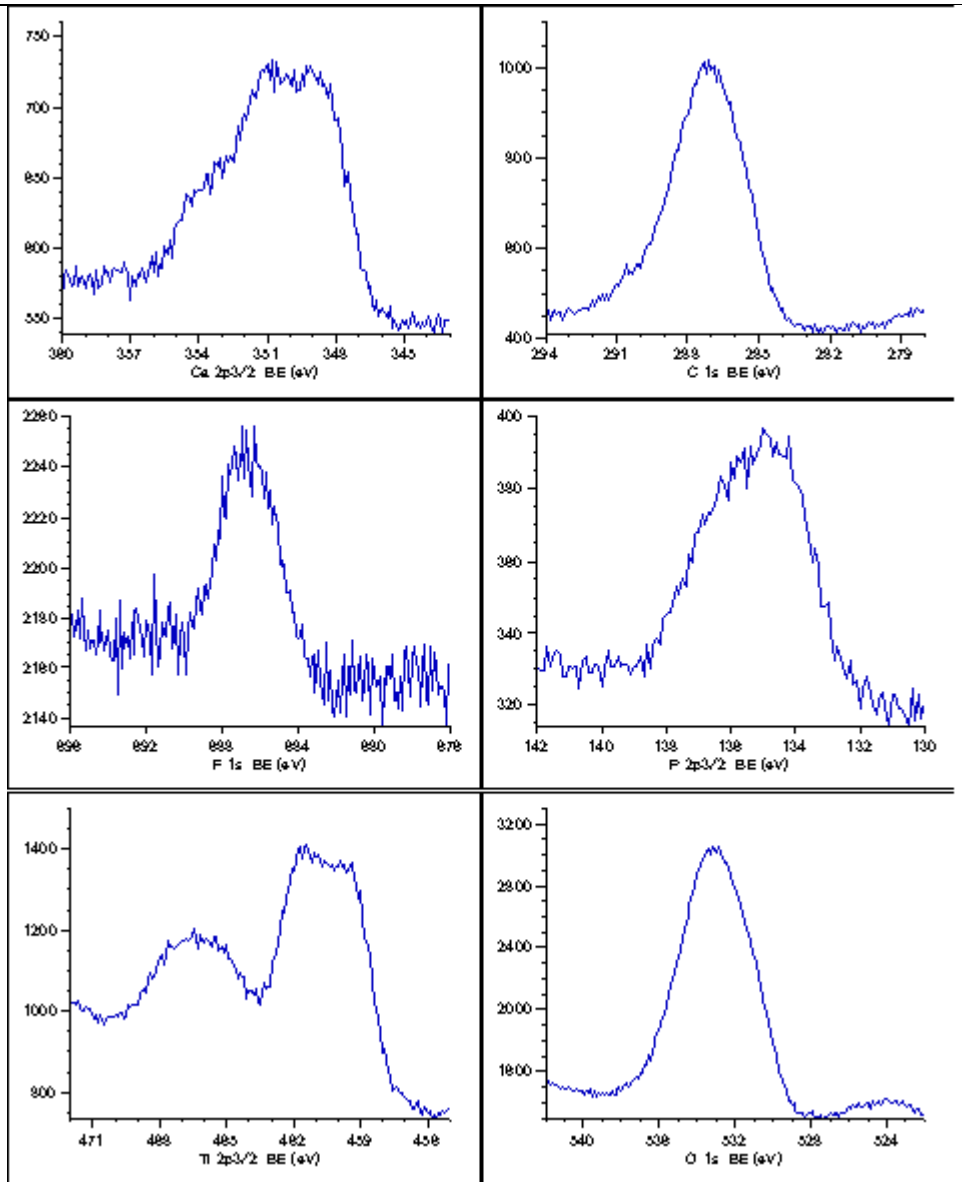

Figure 47. XPS spectrums of Ca 2p 3/2, C 1s, F 1s, P 2p 3/2, Ti 2p 3/2 and O 1s for PEO-coated scaffolds post-SBF immersion test (Continue on next page).

S_2mm_7mins	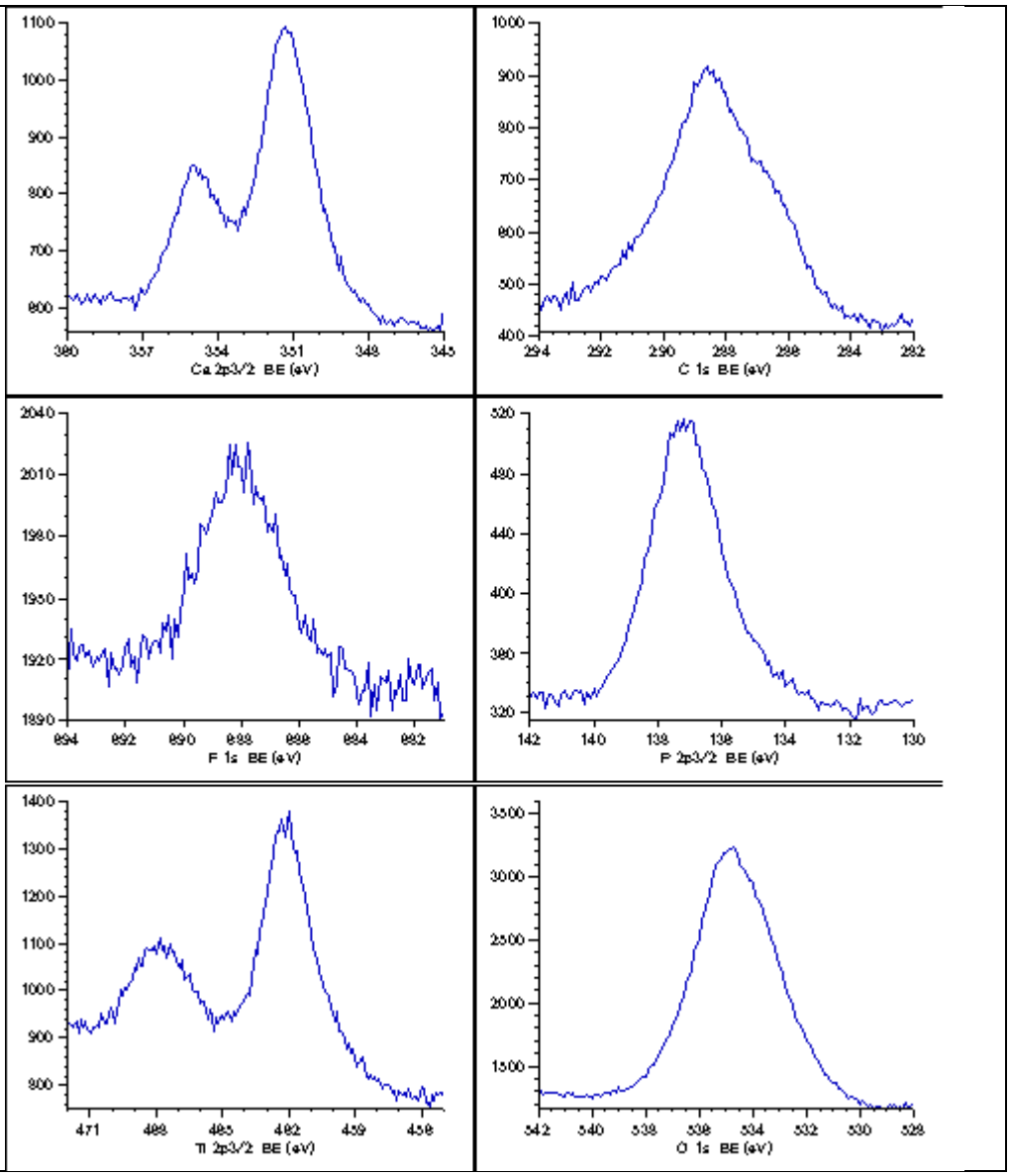

Figure 47. XPS spectrums of Ca 2p 3/2, C 1s, F 1s, P 2p 3/2, Ti 2p 3/2 and O 1s for PEO-coated scaffolds post-SBF immersion test (Continue on next page).

S_3mm_5mins	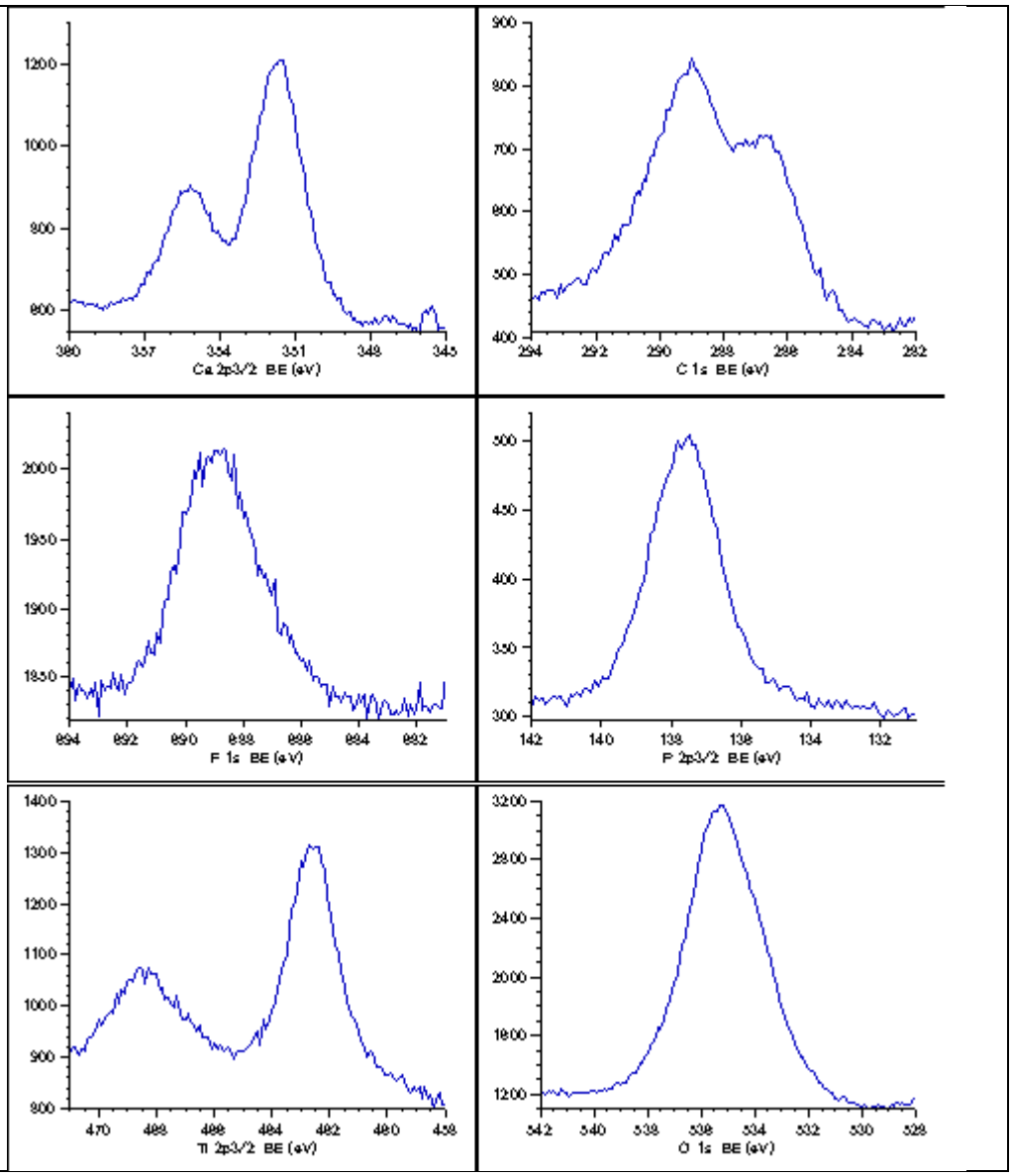

Figure 47. XPS spectrums of Ca 2p 3/2, C 1s, F 1s, P 2p 3/2, Ti 2p 3/2 and O 1s for PEO-coated scaffolds post-SBF immersion test (Continue on next page).

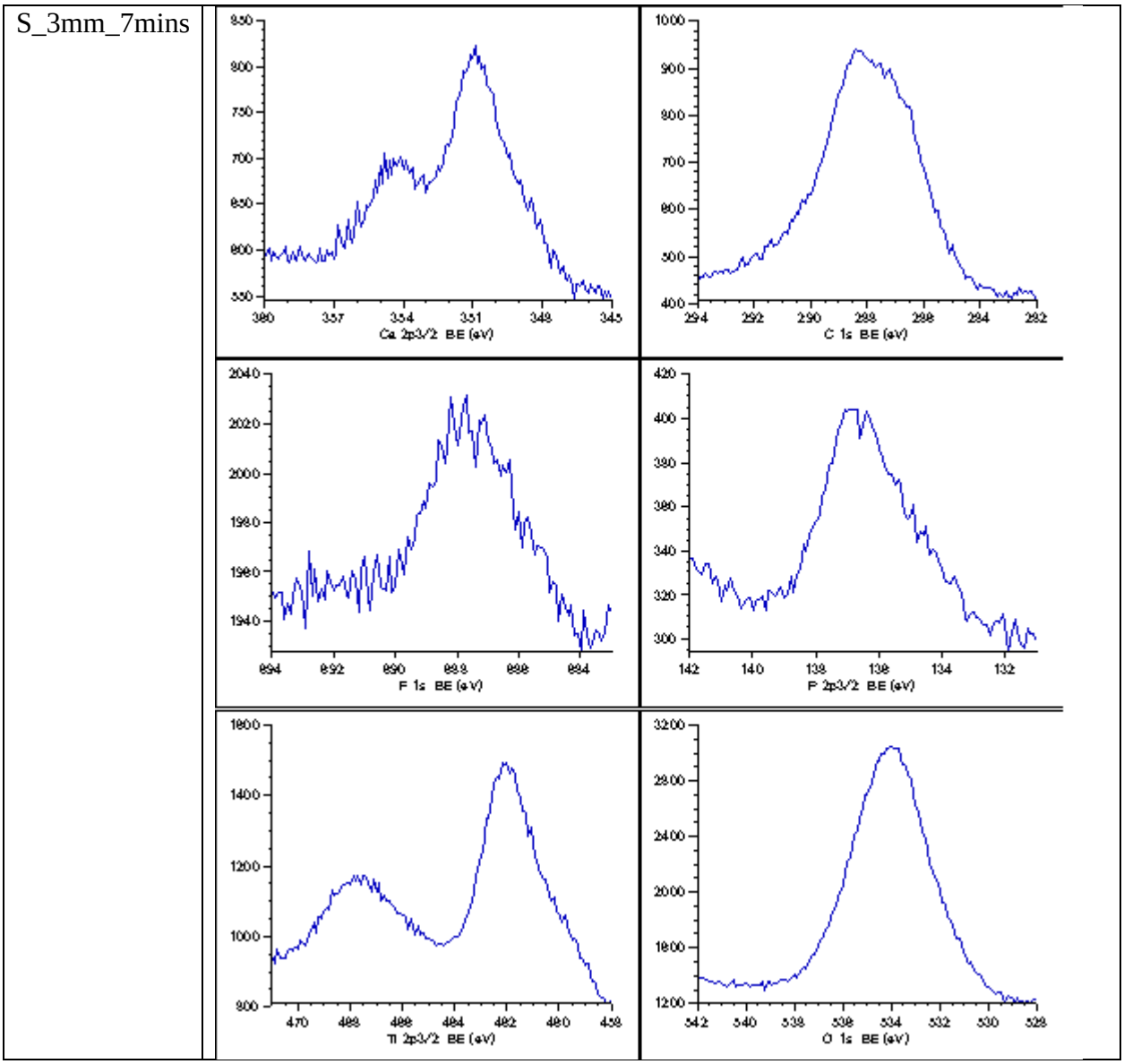

Figure 47. XPS spectrums of Ca 2p 3/2, C 1s, F 1s, P 2p 3/2, Ti 2p 3/2 and O 1s for PEO-coated scaffolds post-SBF immersion test.

5.4 SUMMARY

Generally, the main outcome drawn from this part of the study is that the bio-functional coating produced on the substrate (Ti6Al4V plate and SLM-manufactured porous scaffold) by PEO promotes the apatite formation after 28 days of SBF immersion test. Daily SBF solution

changes are suggested to maintain ion concentrations of SBF solution during the immersion period. Longer PEO treatment time would allow higher crystallization of HAp and FAp phases in the coating, thus induce higher apatite formation on the coating surface. Therefore, the developed PEO bio-functional coating in this study may offer a better proliferation of osteoblast cells on the coating. However, the bioactivity of the actual osteoblast cells' response to these PEO-treated coatings will require specific investigations in a further step of the work.

CHAPTER 6: CONCLUSIONS

6.1 CONCLUSIONS

The study has substantially expanded the understanding of PEO coating growth mechanism and behavior, particularly Ti6Al4V SLM-manufactured porous scaffold. The electrolyte solution used in this study successfully provides bioactive elements to the PEO coating and produces hybrid HAp-TiO_2 coatings. The finding on the effect of PEO treatment on the SLM-manufactured porous scaffolds had previously scarcely reported and this would broaden the knowledge on the potential of PEO treatment to enhance the surface of complex geometries for the orthopedic and orthodontic implant applications. Furthermore, coatings with comparable apatite formation ability have been successfully produced on both Ti6Al4V plate and SLM-manufactured porous scaffolds. The major findings of this research can be summarized as follows;

1. Bio-functional coating containing fluoridated hydroxyapatite on Ti6Al4V was characterized and significant HAp and FAp crystallization was found in the coating, thereby verified the electrolyte solution developed in this study could be potentially used to deposit a bioactive coating on the valve metals surfaces through PEO technique.
2. Ti6Al4V porous scaffolds were successfully fabricated by SLM technique and PEO coating was effectively deposited on the scaffolds. The results revealed the size of macropores may influence the coating growth behavior on the surface with different amount of HAp and FAp crystallization. Therefore, optimal pore sizes to allow homogeneous PEO coating deposition from the periphery to the inner part of the scaffolds are crucial to investigate.
3. Quasi-static compression test result exhibits the mechanical properties of all scaffolds developed in this study are comparable to the mechanical properties of human cancellous

bone. PEO treatment slightly affected the mechanical strength of the SLM-manufactured porous scaffold with increasing treatment time. Post-processing heat treatment is essential prior PEO treatment to enhance the ductility of the scaffolds.

4. Bioactivity examination of PEO coatings on Ti6Al4V SLM-manufactured porous scaffolds produced in electrolytes containing fluoride and calcium salt has shown good bioactivity in vitro. The apatite formation can be observed on all coated scaffolds. It was concluded the combination of bio-functional coating on the surface of the SLM-manufactured porous scaffold provides the synergistic effects, which was beneficial to improve the performance of orthopedic metallic implants.

6.2 FUTURE WORKS

The synergistic combination in the development of bio-functional surface on SLM-manufactured porous scaffolds is scarcely reported until the present, despite their potential in orthopedic implants application. The extension of this understanding of the following aspects would be particularly beneficial;

1. Investigation of the optimal amount of fluoride in the coating layer which would promote excellent results without causing adverse effects in adjacent tissue.
2. Dynamic mechanical testing to investigate the fatigue behavior of the scaffolds under cyclic loading.
3. Bioactivity test to examine the *in vitro* cell response to the coatings with osteoblast cells.
4. Investigation of *in vitro* antibacterial activity of the coatings with *S. aureus* and *E. coli* by colony counting method.

REFERENCES

1. Kaseem, M.; Ko, Y.G. Effect of starch on the corrosion behavior of Al-Mg-Si alloy processed by micro arc oxidation from an ecofriendly electrolyte system. *Bioelectrochemistry* **2019**, *128*, 133–139.

2. Kaluđerović, M.R.; Schreckenbach, J.P.; Graf, H.-L. Titanium dental implant surfaces obtained by anodic spark deposition – From the past to the future. *Mater. Sci. Eng. C* **2016**, *69*, 1429–1441.

3. Kaseem, M.; Fatimah, S.; Nashrah, N.; Gun Ko, Y. Recent progress in surface modification of metals coated by plasma electrolytic oxidation: Principle, structure, and performance. *Prog. Mater. Sci.* **2020**, 100735.

4. Wang, D.; Liu, X.; Wu, Y.; Han, H.; Yang, Z.; Su, Y.; Zhang, X.; Wu, G.; Shen, D. Evolution process of the plasma electrolytic oxidation (PEO) coating formed on aluminum in an alkaline sodium hexametaphosphate ((NaPO3)6) electrolyte. *J. Alloys Compd.* **2019**, *798*, 129–143.

5. Bordbar-Khiabani, A.; Ebrahimi, S.; Yarmand, B. Plasma electrolytic oxidation of monocrystalline silicon using silicate electrolyte containing boric acid. *Appl. Surf. Sci.* **2018**, *462*.

6. Fattah-alhosseini, A.; Molaei, M.; Babaei, K. The effects of nano- and micro-particles on properties of plasma electrolytic oxidation (PEO) coatings applied on titanium substrates: A review. *Surfaces and Interfaces* **2020**, *21*, 100659.

7. Rafieerad, A.R.; Ashra, M.R.; Mahmoodian, R.; Bushroa, A.R. Surface characterization and corrosion behavior of calcium phosphate-base composite layer on titanium and its alloys via plasma electrolytic oxidation: A review paper. *Mater. Sci. Eng. C* **2015**, *57*, 397–413.

8. Xu, L.; Wu, C.; Lei, X.; Zhang, K.; Liu, C.; Ding, J.; Shi, X. Effect of oxidation time on cytocompatibility of ultrafine-grained pure Ti in micro-arc oxidation treatment. *Surf. Coatings Technol.* **2018**, *342*, 12–22.

9. Santos, E.; de Souza, G.B.; Serbena, F.C.; Santos, H.L.; de Lima, G.G.; Szesz, E.M.; Lepienski, C.M.; Kuromoto, N.K. Effect of anodizing time on the mechanical properties of porous titania coatings formed by micro-arc oxidation. *Surf. Coatings Technol.* **2017**, *309*, 203–211.

10. Shin, K.R.; Ko, Y.G.; Shin, D.H. Effect of electrolyte on surface properties of pure titanium coated by plasma electrolytic oxidation. *J. Alloys Compd.* **2011**, *509*, S478–S481.

11. Wang, Y.; Wang, L.; Zheng, H.; Du, C.; ChengyunNing; Shi, Z.; Xu, C. Effect of frequency on the structure and cell response of Ca- and P-containing MAO films. *Appl. Surf. Sci.* **2010**, *256*, 2018–2024.

12. Babaei, M.; Dehghanian, C.; Taheri, P.; Babaei, M. Effect of duty cycle and electrolyte additive on photocatalytic performance of TiO2-ZrO2 composite layers prepared on CP Ti

by micro arc oxidation method. *Surf. Coatings Technol.* **2016**, *307*, 554–564.

13. S., H.; Ashfaq, M.; T., A.; Harilal, M.; N., R. Role of electrolyte additives on in-vitro corrosion behavior of DC plasma electrolytic oxidization coatings formed on Cp-Ti. *Surf. Coatings Technol.* **2016**, *292*, 20–29.

14. Roknian, M.; Fattah-alhosseini, A.; Gashti, S.O. Plasma Electrolytic Oxidation Coatings on Pure Ti Substrate: Effects of Na3PO4 Concentration on Morphology and Corrosion Behavior of Coatings in Ringer's Physiological Solution. *J. Mater. Eng. Perform.* **2018**, *27*, 1343–1351.

15. Vakili-Azghandi, M.; Fattah-alhosseini, A.; Keshavarz, M.K. Optimizing the electrolyte chemistry parameters of PEO coating on 6061 Al alloy by corrosion rate measurement: Response surface methodology. *Measurement* **2018**, *124*, 252–259.

16. Fattah-alhosseini, A.; Sabaghi Joni, M. Effect of KOH Concentration on the Microstructure and Electrochemical Properties of MAO-Coated Mg Alloy AZ31B. *J. Mater. Eng. Perform.* **2015**, *24*, 3444–3452.

17. Fattah-Alhosseini, A.; Vakili-Azghandi, M.; Keshavarz, M.K. Influence of Concentrations of KOH and Na2SiO3 Electrolytes on the Electrochemical Behavior of Ceramic Coatings on 6061 Al Alloy Processed by Plasma Electrolytic Oxidation. *Acta Metall. Sin. (English Lett.* **2016**, *29*, 274–281.

18. Hussein, R.O.; Nie, X.; Northwood, D.O.; Yerokhin, A.; Matthews, A. Spectroscopic study of electrolytic plasma and discharging behaviour during the plasma electrolytic oxidation (PEO) process. *J. Phys. D. Appl. Phys.* **2010**, *43*, 105203.

19. Hussein, R.O.; Northwood, D.O.; Nie, X. Coating growth behavior during the plasma electrolytic oxidation process. *J. Vac. Sci. Technol. A* **2010**, *28*, 766–773.

20. Yerokhin, A.L.; Snizhko, L.O.; Gurevina, N.L.; Leyland, A.; Pilkington, A.; Matthews, A. Discharge characterization in plasma electrolytic oxidation of aluminium. *J. Phys. D. Appl. Phys.* **2003**, *36*, 2110–2120.

21. Algahtani, A.; Mahmoud, E.R.I. Erosion and corrosion resistance of plasma electrolytic oxidized 6082 aluminum alloy surface at low and high temperatures. *J. Mater. Res. Technol.* **2019**, *8*, 2699–2709.

22. Sukumaran, A.; Sampatirao, H.; Balasubramanian, R.; Parfenov, E.; Mukaeva, V.; Nagumothu, R. Formation of ZrO2–SiC Composite Coating on Zirconium by Plasma Electrolytic Oxidation in Different Electrolyte Systems Comprising of SiC Nanoparticles. *Trans. Indian Inst. Met.* **2018**, *71*, 1699–1713.

23. Wang, J.-M.; Tsai, D.-S.; Tsai, J.T.J.; Chou, C.-C. Coloring the aluminum alloy surface in plasma electrolytic oxidation with the green pigment colloid. *Surf. Coatings Technol.* **2017**, *321*, 164–170.

24. Antônio, C.A.; Cruz, N.C.; Rangel, E.C.; Rangel, R. de C.C.; Araujo, T. do E.S.; Durrant, S.F.; Más, B.A.; Duek, E.A.R. Hydroxyapatite coating deposited on grade 4 Titanium by Plasma Electrolytic Oxidation . *Mater. Res.* 2014, *17*, 1427–1433.

25. Kazek-Kęsik, A.; Kalemba-Rec, I.; Simka, W. Anodization of a Medical-Grade Ti-6Al-7Nb Alloy in a Ca(H2PO2)2-Hydroxyapatite Suspension. *Mater.* 2019, *12*.

26. Curran, J.; Clyne, B. Porosity in plasma electrolytic oxide coatings. *Acta Mater.* **2006**, *54*, 1985–1993.

27. Teixeira, L.N.; Crippa, G.E.; Lefebvre, L.-P.; De Oliveira, P.T.; Rosa, A.L.; Beloti, M.M. The influence of pore size on osteoblast phenotype expression in cultures grown on porous titanium. *Int. J. Oral Maxillofac. Surg.* **2012**, *41*, 1097–1101.

28. Yerokhin, A.L.; Shatrov, A.; Samsonov, V.; Shashkov, P.; Pilkington, A.; Leyland, A.; Matthews, A. Oxide ceramic coatings on aluminium alloys produced by a pulsed bipolar plasma electrolytic oxidation process. *Surf. Coatings Technol.* **2005**, *199*, 150–157.

29. Wang, Y.; Jiang, Z.; Yao, Z. Microstructure, bonding strength and thermal shock resistance of ceramic coatings on steels prepared by plasma electrolytic oxidation. *Appl. Surf. Sci.* **2009**, *256*, 650–656.

30. Khan, R.H.U.; Yerokhin, A.L.; Pilkington, T.; Leyland, A.; Matthews, A. Residual stresses in plasma electrolytic oxidation coatings on Al alloy produced by pulsed unipolar current. *Surf. Coatings Technol.* **2005**, *200*, 1580–1586.

31. Guan, Y.; Xia, Y.; Xu, F. Interface fracture property of PEO ceramic coatings on aluminum alloy. *Surf. Coatings Technol.* **2008**, *202*, 4204–4209.

32. Ishizawa, H.; Ogino, M. Formation and characterization of anodic titanium oxide films containing Ca and P. *J. Biomed. Mater. Res.* **1995**, *29*, 65–72.

33. Yap, C.Y.; Chua, C.K.; Dong, Z.L.; Liu, Z.H.; Zhang, D.Q.; Loh, L.E.; Sing, S.L. Review of selective laser melting: Materials and applications. *Appl. Phys. Rev.* **2015**, *2*, 41101.

34. Kruth, J.; Vandenbroucke, B.; Vaerenbergh, J. V; Naert, I. Digital manufacturing of biocompatible metal frameworks for complex dental prostheses by means of SLS/SLM.; 2005.

35. Wehmöller, M.; Warnke, P.H.; Zilian, C.; Eufinger, H. Implant design and production—a new approach by selective laser melting. *Int. Congr. Ser.* **2005**, *1281*, 690–695.

36. Chen, G.X.; Zeng, X.Y.; Wang, Z.M.; Guan, K.; Peng, C.W. Fabrication of Removable Partial Denture Framework by Selective Laser Melting. *Adv. Mater. Res.* **2011**, *317–319*, 174–178.

37. Richard, B.; Dominic, E.; Peter, E.; Alan, B.; Adrian, S. Rapid manufacture of custom-fitting surgical guides. *Rapid Prototyp. J.* **2009**, *15*, 346–354.

38. Nguyen, D.-S.; Park, H.-S.; Lee, C.-M. Applying Selective Laser Melting to Join Al and Fe: An Investigation of Dissimilar Materials. *Appl. Sci.* 2019, *9*.

39. Puleo, D.A.; Nanci, A. Understanding and controlling the bone–implant interface. *Biomaterials* **1999**, *20*, 2311–2321.

40. McNamara, L.E.; Sjöström, T.; Burgess, K.E. V; Kim, J.J.W.; Liu, E.; Gordonov, S.; Moghe, P. V; Meek, R.M.D.; Oreffo, R.O.C.; Su, B.; et al. Skeletal stem cell physiology

on functionally distinct titania nanotopographies. *Biomaterials* **2011**, *32*, 7403–7410.

41. Popat, K.C.; Leoni, L.; Grimes, C.A.; Desai, T.A. Influence of engineered titania nanotubular surfaces on bone cells. *Biomaterials* **2007**, *28*, 3188–3197.

42. Xiu, P.; Jia, Z.; Lv, J.; Yin, C.; Cheng, Y.; Zhang, K.; Song, C.; Leng, H.; Zheng, Y.; Cai, H.; et al. Tailored Surface Treatment of 3D Printed Porous Ti6Al4V by Microarc Oxidation for Enhanced Osseointegration via Optimized Bone In-Growth Patterns and Interlocked Bone/Implant Interface. *ACS Appl. Mater. & Interfaces* **2016**, *8*, 17964–17975.

43. van Hengel, I.A.J.; Gelderman, F.S.A.; Athanasiadis, S.; Minneboo, M.; Weinans, H.; Fluit, A.C.; van der Eerden, B.C.J.; Fratila-Apachitei, L.E.; Apachitei, I.; Zadpoor, A.A. Functionality-packed additively manufactured porous titanium implants. *Mater. Today Bio* **2020**, *7*, 100060.

44. Gorgin Karaji, Z.; Hedayati, R.; Pouran, B.; Apachitei, I.; Zadpoor, A.A. Effects of plasma electrolytic oxidation process on the mechanical properties of additively manufactured porous biomaterials. *Mater. Sci. Eng. C* **2017**, *76*, 406–416.

45. Golestani-Fard, F.; Bayati, M.R.; Zargar, H.R.; Abbasi, S.; Rezaei, H.R. MAO-preparation of nanocrystalline hydroxyapatite–titania composite films: Formation stages and effect of the growth time. *Mater. Res. Bull.* **2011**, *46*, 2422–2426.

46. Qiao, L.P.; Lou, J.; Zhang, S.F.; Qu, B.; Chang, W.H.; Zhang, R.F. The entrance mechanism of calcium and phosphorus elements into micro arc oxidation coatings developed on Ti6Al4V alloy. *Surf. Coatings Technol.* **2016**, *285*, 187–196.

47. Zhu, L.; Ye, X.; Tang, G.; Zhao, N.; Gong, Y.; Zhao, Y.; Zhao, J.; Zhang, X. Biomimetic coating of compound titania and hydroxyapatite on titanium. *J. Biomed. Mater. Res. Part A* **2007**, *83A*, 1165–1175.

48. Kulkarni Aranya, A.; Pushalkar, S.; Zhao, M.; LeGeros, R.Z.; Zhang, Y.; Saxena, D. Antibacterial and bioactive coatings on titanium implant surfaces. *J. Biomed. Mater. Res. Part A* **2017**, *105*, 2218–2227.

49. Santos-Coquillat, A.; Gonzalez Tenorio, R.; Mohedano, M.; Martinez-Campos, E.; Arrabal, R.; Matykina, E. Tailoring of antibacterial and osteogenic properties of Ti6Al4V by plasma electrolytic oxidation. *Appl. Surf. Sci.* **2018**, *454*, 157–172.

50. Hanawa, T. 2.1 - Transition of surface modification of titanium for medical and dental use. In *Titanium in Medical and Dental Applications*; Froes, F., Qian, M., Eds.; Woodhead Publishing, 2018; pp. 95–113 ISBN 978-0-12-812456-7.

51. Kaseem, M.; Choe, H.-C. Triggering the hydroxyapatite deposition on the surface of PEO-coated Ti–6Al–4V alloy via the dual incorporation of Zn and Mg ions. *J. Alloys Compd.* **2020**, *819*, 153038.

52. Yu, J.-M.; Kim, H.-J.; Ahn, S.-G.; Choe, H.-C. Plasma electrolytic oxidation of Ti-6Al-4V alloy in electrolytes containing bone formation ions. *Appl. Surf. Sci.* **2020**, *513*, 145776.

53. Durdu, S.; Usta, M.; Berkem, A.S. Bioactive coatings on Ti6Al4V alloy formed by plasma

electrolytic oxidation. *Surf. Coatings Technol.* **2016**, *301*, 85–93.

54. Adeleke, S.A.; Ramesh, S.; Bushroa, A.R.; Ching, Y.C.; Sopyan, I.; Maleque, M.A.; Krishnasamy, S.; Chandran, H.; Misran, H.; Sutharsini, U. The properties of hydroxyapatite ceramic coatings produced by plasma electrolytic oxidation. *Ceram. Int.* **2018**, *44*, 1802–1811.

55. Ahounbar, E.; Mousavi Khoei, S.M.; Omidvar, H. Characteristics of in-situ synthesized Hydroxyapatite on TiO2 ceramic via plasma electrolytic oxidation. *Ceram. Int.* **2019**, *45*, 3118–3125.

56. Durdu, S. Characterization, Bioactivity and Antibacterial Properties of Copper-Based TiO2 Bioceramic Coatings Fabricated on Titanium. *Coatings* **2018**, *9*, 1.

57. Wang, R.; He, X.; Gao, Y.; Zhang, X.; Yao, X.; Tang, B. Antimicrobial property, cytocompatibility and corrosion resistance of Zn-doped ZrO2/TiO2 coatings on Ti6Al4V implants. *Mater. Sci. Eng. C* **2017**, *75*, 7–15.

58. Li, H.; Sun, Y.; Zhang, J. Effect of ZrO2 particle on the performance of micro-arc oxidation coatings on Ti6Al4V. *Appl. Surf. Sci.* **2015**, *342*, 183–190.

59. Zhao, D.; Lu, Y.; Wang, Z.; Zeng, X.; Liu, S.; Wang, T. Antifouling properties of micro arc oxidation coatings containing Cu2O/ZnO nanoparticles on Ti6Al4V. *Int. J. Refract. Met. Hard Mater.* **2016**, *54*, 417–421.

60. Mohedano, M.; Luthringer, B.J.C.; Mingo, B.; Feyerabend, F.; Arrabal, R.; Sanchez-Egido, P.J.; Blawert, C.; Willumeit-Römer, R.; Zheludkevich, M.L.; Matykina, E. Bioactive plasma electrolytic oxidation coatings on Mg-Ca alloy to control degradation behaviour. *Surf. Coatings Technol.* **2017**, *315*, 454–467.

61. Wang, L.; Feng, T.; Yu, S.; Cheng, Y.; Bu, Z.; Hu, X. Fluoride effect on plasma electrolytic oxidation coating formed on Mg-Al alloy in alkaline electrolytes. *Mater. Res. Express* **2020**, *7*, 16412.

62. Němcová, A.; Skeldon, P.; Thompson, G.E.; Pacal, B. Effect of fluoride on plasma electrolytic oxidation of AZ61 magnesium alloy. *Surf. Coatings Technol.* **2013**, *232*, 827–838.

63. Santos-Coquillat, A.; Mohedano, M.; Martinez-Campos, E.; Arrabal, R.; Pardo, A.; Matykina, E. Bioactive multi-elemental PEO-coatings on titanium for dental implant applications. *Mater. Sci. Eng. C* **2019**, *97*, 738–752.

64. Liu, F.; Wang, F.; Shimizu, T.; Igarashi, K.; Zhao, L. Hydroxyapatite formation on oxide films containing Ca and P by hydrothermal treatment. *Ceram. Int.* **2006**, *32*, 527–531.

65. Astashina, N.; Lugovskoy, A.; Kossenko, A.; Lugovskoy, S.; Rogozhnikov, G.; Zinigrad, M. Investigation of the Effectiveness of Dental Implant Osseointegration Characterized by Different Surface Types. *Met.* 2017, *7*.

66. Khiabani, A.B.; Ghanbari, A.; Yarmand, B.; Zamanian, A.; Mozafari, M. Improving corrosion behavior and in vitro bioactivity of plasma electrolytic oxidized AZ91 magnesium alloy using calcium fluoride containing electrolyte. *Mater. Lett.* **2018**, *212*,

98–102.

67. Barati Darband, G.; Aliofkhazraei, M.; Hamghalam, P.; Valizade, N. Plasma electrolytic oxidation of magnesium and its alloys: Mechanism, properties and applications. *J. Magnes. Alloy.* **2017**, *5*, 74–132.

68. Chang, L. Growth regularity of ceramic coating on magnesium alloy by plasma electrolytic oxidation. *J. Alloys Compd.* **2009**, *468*, 462–465.

69. Clyne, T.W.; Troughton, S.C. A review of recent work on discharge characteristics during plasma electrolytic oxidation of various metals. *Int. Mater. Rev.* **2019**, *64*, 127–162.

70. Hussein, R.O.; Nie, X.; Northwood, D.O. An investigation of ceramic coating growth mechanisms in plasma electrolytic oxidation (PEO) processing. *Electrochim. Acta* **2013**, *112*, 111–119.

71. Singh, R.; Tan, C.; Abd Shukor, M.; Sopyan, I.; Teng, W. The influence of Ca/P ratio on the properties of hydroxyapatite bioceramics. *Proc SPIE* **2007**, *6423*.

72. Laveissière, M.; Cerda, H.; Roche, J.; Cassayre, L.; Arurault, L. In-depth study of the influence of electrolyte composition on coatings prepared by plasma electrolytic oxidation of TA6V alloy. *Surf. Coatings Technol.* **2019**, *361*, 50–62.

73. Sundararajan, G.; Rama Krishna, L. Mechanisms underlying the formation of thick alumina coatings through the MAO coating technology. *Surf. Coatings Technol.* **2003**, *167*, 269–277.

74. Rama Krishna, L.; Somaraju, K.R.C.; Sundararajan, G. The tribological performance of ultra-hard ceramic composite coatings obtained through microarc oxidation. *Surf. Coatings Technol.* **2003**, *163–164*, 484–490.

75. Banakh, O.; Snizhko, L.; Journot, T.; Gay, P.-A.; Csefalvay, C.; Kalinichenko, O.; Girin, O.; Marger, L.; Durual, S. The Influence of the Electrolyte Nature and PEO Process Parameters on Properties of Anodized Ti-15Mo Alloy Intended for Biomedical Applications. *Met.* 2018, *8*.

76. Sowa, M.; Piotrowska, M.; Widziołek, M.; Dercz, G.; Tylko, G.; Gorewoda, T.; Osyczka, A.M.; Simka, W. Bioactivity of coatings formed on Ti–13Nb–13Zr alloy using plasma electrolytic oxidation. *Mater. Sci. Eng. C* **2015**, *49*, 159–173.

77. Cooper, L.F. A role for surface topography in creating and maintaining bone at titanium endosseous implants. *J. Prosthet. Dent.* **2000**, *84*, 522–534.

78. Le Guehennec, L.; Lopez-Heredia, M.-A.; Enkel, B.; Weiss, P.; Amouriq, Y.; Layrolle, P. Osteoblastic cell behaviour on different titanium implant surfaces. *Acta Biomater.* **2008**, *4*, 535–543.

79. Anselme, K.; Bigerelle, M. Topography effects of pure titanium substrates on human osteoblast long-term adhesion. *Acta Biomater.* **2005**, *1*, 211–222.

80. Kim, M.-J.; Kim, C.-W.; Lim, Y.-J.; Heo, S.-J. Microrough titanium surface affects biologic response in MG63 osteoblast-like cells. *J. Biomed. Mater. Res. Part A* **2006**, *79A*,

1023–1032.

81. Zhu, X.; Chen, J.; Scheideler, L.; Reichl, R.; Geis-Gerstorfer, J. Effects of topography and composition of titanium surface oxides on osteoblast responses. *Biomaterials* **2004**, *25*, 4087–4103.

82. Li, L.-H.; Kong, Y.-M.; Kim, H.-W.; Kim, Y.-W.; Kim, H.-E.; Heo, S.-J.; Koak, J.-Y. Improved biological performance of Ti implants due to surface modification by micro-arc oxidation. *Biomaterials* **2004**, *25*, 2867–2875.

83. Hussein, R.O.; Zhang, P.; Nie, X.; Xia, Y.; Northwood, D.O. The effect of current mode and discharge type on the corrosion resistance of plasma electrolytic oxidation (PEO) coated magnesium alloy AJ62. *Surf. Coatings Technol.* **2011**, *206*, 1990–1997.

84. Holmberg, K.; Laukkanen, A.; Ronkainen, H.; Wallin, K.; Varjus, S.; Koskinen, J. Tribological contact analysis of a rigid ball sliding on a hard coated surface: Part I: Modelling stresses and strains. *Surf. Coatings Technol.* **2006**, *200*, 3793–3809.

85. Habazaki, H.; Uozumi, M.; Konno, H.; Shimizu, K.; Skeldon, P.; Thompson, G.E. Crystallization of anodic titania on titanium and its alloys. *Corros. Sci.* **2003**, *45*, 2063–2073.

86. Teh, T.H.; Berkani, A.; Mato, S.; Skeldon, P.; Thompson, G.E.; Habazaki, H.; Shimizu, K. Initial stages of plasma electrolytic oxidation of titanium. *Corros. Sci.* **2003**, *45*, 2757–2768.

87. Neupane, M.P.; Kim, Y.K.; Park, I.S.; Lee, S.J.; Lee, M.H.; Bae, T.S. Effect of electrolyte pH on the structure andin vitro osteoblasts response to anodic titanium oxide. *Met. Mater. Int.* **2008**, *14*, 607–613.

88. Fousová, M.; Vojtěch, D.; Doubrava, K.; Daniel, M.; Lin, C.-F. Influence of Inherent Surface and Internal Defects on Mechanical Properties of Additively Manufactured Ti6Al4V Alloy: Comparison between Selective Laser Melting and Electron Beam Melting. *Mater.* 2018, *11*.

89. Yan, C.; Hao, L.; Hussein, A.; Young, P. Ti–6Al–4V triply periodic minimal surface structures for bone implants fabricated via selective laser melting. *J. Mech. Behav. Biomed. Mater.* **2015**, *51*, 61–73.

90. Melhem, A.; Henrion, G.; Czerwiec, T.; Briançon, J.L.; Duchanoy, T.; Brochard, F.; Belmonte, T. Changes induced by process parameters in oxide layers grown by the PEO process on Al alloys. *Surf. Coatings Technol.* **2011**, *205*, S133–S136.

91. Wang, L.S.; Pan, C.X. Characterisation of microdischarge evolution and coating morphology transition in plasma electrolytic oxidation of magnesium alloy. *Surf. Eng.* **2007**, *23*, 324–328.

92. Polo, T.O.B.; da Silva, W.P.; Momesso, G.A.C.; Lima-Neto, T.J.; Barbosa, S.; Cordeiro, J.M.; Hassumi, J.S.; da Cruz, N.C.; Okamoto, R.; Barão, V.A.R.; et al. Plasma Electrolytic Oxidation as a Feasible Surface Treatment for Biomedical Applications: an in vivo study. *Sci. Rep.* **2020**, *10*, 10000.

93. Garcia-Cabezón, C.; Rodriguez-Mendez, M.L.; Amigo Borrás, V.; Raquel, B.; Rodriguez Cabello, J.C.; Ibañez Fonseca, A.; Martin-Pedrosa, F. Application of Plasma Electrolytic Oxidation Coating on Powder Metallurgy Ti-6Al-4V for Dental Implants. *Met.* 2020, *10*.

94. Shin, K.R.; Yoon, S. Il; Ko, Y.G.; Shin, D.H. Deposition of hydroxyl-apatite on titanium subjected to electrochemical plasma coating. *Electrochim. Acta* **2013**, *109*, 173–180.

95. Jin, N.; Wang, F.; Wang, Y.; Zhang, B.; Cheng, H.; Zhang, H. Failure and energy absorption characteristics of four lattice structures under dynamic loading. *Mater. Des.* **2019**, *169*, 107655.

96. Kadkhodapour, J.; Montazerian, H.; Raeisi, S. Investigating internal architecture effect in plastic deformation and failure for TPMS-based scaffolds using simulation methods and experimental procedure. *Mater. Sci. Eng. C* **2014**, *43*, 587–597.

97. Kadkhodapour, J.; Montazerian, H.; Darabi, A.C.; Anaraki, A.P.; Ahmadi, S.M.; Zadpoor, A.A.; Schmauder, S. Failure mechanisms of additively manufactured porous biomaterials: Effects of porosity and type of unit cell. *J. Mech. Behav. Biomed. Mater.* **2015**, *50*, 180–191.

98. Zhang, X.-Y.; Fang, G.; Zhou, J. Additively Manufactured Scaffolds for Bone Tissue Engineering and the Prediction of their Mechanical Behavior: A Review. *Materials (Basel).* 2017, *10*.

99. Gorny, B.; Niendorf, T.; Lackmann, J.; Thoene, M.; Troester, T.; Maier, H.J. In situ characterization of the deformation and failure behavior of non-stochastic porous structures processed by selective laser melting. *Mater. Sci. Eng. A* **2011**, *528*, 7962–7967.

100. Khan, R.H.U.; Yerokhin, A.; Li, X.; Dong, H.; Matthews, A. Surface characterisation of DC plasma electrolytic oxidation treated 6082 aluminium alloy: Effect of current density and electrolyte concentration. *Surf. Coatings Technol.* **2010**, *205*, 1679–1688.

101. Zhang, B.; Li, Y.; Bai, Q. Defect Formation Mechanisms in Selective Laser Melting: A Review. *Chinese J. Mech. Eng.* **2017**, *30*, 515–527.

102. Zhao, Z.-Y.; Li, L.; Bai, P.-K.; Jin, Y.; Wu, L.-Y.; Li, J.; Guan, R.-G.; Qu, H.-Q. The Heat Treatment Influence on the Microstructure and Hardness of TC4 Titanium Alloy Manufactured via Selective Laser Melting. *Mater.* 2018, *11*.

103. Amin Yavari, S.; Ahmadi, S.M.; van der Stok, J.; Wauthle, R.; Riemslag, A.C.; Janssen, M.; Schrooten, J.; Weinans, H.; Zadpoor, A.A. Effects of bio-functionalizing surface treatments on the mechanical behavior of open porous titanium biomaterials. *J. Mech. Behav. Biomed. Mater.* **2014**, *36*, 109–119.

104. Yue, X.-Z.; Fukazawa, H.; Maruyama, K.; Matsuo, K.; Kitazono, K. Effect of Post Heat Treatment on the Mechanical Properties of Porous Ti–6Al–4V Alloys Manufactured through Powder Bed Fusion Process. *Mater. Trans.* **2019**, *60*, 74–79.

105. Yánez, A.; Herrera, A.; Martel, O.; Monopoli, D.; Afonso, H. Compressive behaviour of gyroid lattice structures for human cancellous bone implant applications. *Mater. Sci. Eng. C* **2016**, *68*, 445–448.

106. Y.H. An, R.A.D. *Mechanical Testing of Bone and the Bone-Implant Interface*; CRC Press, 2010;

107. Linde, F.; Hvid, I.; Pongsoipetch, B. Energy absorptive properties of human trabecular bone specimens during axial compression. *J. Orthop. Res.* **1989**, *7*, 432–439.

108. Zhang, L.; Feih, S.; Daynes, S.; Chang, S.; Wang, M.Y.; Wei, J.; Lu, W.F. Energy absorption characteristics of metallic triply periodic minimal surface sheet structures under compressive loading. *Addit. Manuf.* **2018**, *23*, 505–515.

109. Thijs, L.; Verhaeghe, F.; Craeghs, T.; Humbeeck, J. Van; Kruth, J.-P. A study of the microstructural evolution during selective laser melting of Ti–6Al–4V. *Acta Mater.* **2010**, *58*, 3303–3312.

110. Krakhmalev, P.; Fredriksson, G.; Yadroitsava, I.; Kazantseva, N.; Plessis, A. du; Yadroitsev, I. Deformation Behavior and Microstructure of Ti6Al4V Manufactured by SLM. *Phys. Procedia* **2016**, *83*, 778–788.

111. Vrancken, B.; Thijs, L.; Kruth, J.-P.; Van Humbeeck, J. Heat treatment of Ti6Al4V produced by Selective Laser Melting: Microstructure and mechanical properties. *J. Alloys Compd.* **2012**, *541*, 177–185.

112. Murr, L.E.; Quinones, S.A.; Gaytan, S.M.; Lopez, M.I.; Rodela, A.; Martinez, E.Y.; Hernandez, D.H.; Martinez, E.; Medina, F.; Wicker, R.B. Microstructure and mechanical behavior of Ti–6Al–4V produced by rapid-layer manufacturing, for biomedical applications. *J. Mech. Behav. Biomed. Mater.* **2009**, *2*, 20–32.

113. Song, B.; Dong, S.; Zhang, B.; Liao, H.; Coddet, C. Effects of processing parameters on microstructure and mechanical property of selective laser melted Ti6Al4V. *Mater. Des.* **2012**, *35*, 120–125.

114. Campanelli, S.L.; Contuzzi, N.; Ludovico, A.D.; Caiazzo, F.; Cardaropoli, F.; Sergi, V. Manufacturing and Characterization of Ti6Al4V Lattice Components Manufactured by Selective Laser Melting. *Mater.* 2014, *7*.

115. Sidambe, A.T. Biocompatibility of Advanced Manufactured Titanium Implants—A Review. *Mater.* 2014, *7*.

116. Khorasani, A.M.; Gibson, I.; Ghaderi, A.; Mohammed, M.I. Investigation on the effect of heat treatment and process parameters on the tensile behaviour of SLM Ti-6Al-4V parts. *Int. J. Adv. Manuf. Technol.* **2019**, *101*, 3183–3197.

117. Kiel-Jamrozik M., Jamrozik W., W.I. The heat treatment influence on the structure and mechanical properties of Ti6Al4V alloy manufactured by SLM technology. *Innov. Biomed. Eng. IBE 2017. Adv. Intell. Syst. Comput.* **2018**, *623*.

118. Nordström, E.; Sanchez-Munoz, O. Physics of bone bonding mechanism of different surface bioactive ceramic materials in vitro and in vivo. *Biomed. Mater. Eng.* **2001**, *11*, 221–231.

119. Chioibasu, D.; Duta, L.; Popescu-Pelin, G.; Popa, N.; Milodin, N.; Iosub, S.; Balescu, M.L.; Catalin Galca, A.; Claudiu Popa, A.; Oktar, N.F.; et al. Animal Origin Bioactive

Hydroxyapatite Thin Films Synthesized by RF-Magnetron Sputtering on 3D Printed Cranial Implants. *Met.* 2019, *9*.

120. Daculsi, G.; Legeros, R.Z.; Nery, E.; Lynch, K.; Kerebel, B. Transformation of biphasic calcium phosphate ceramics in vivo: Ultrastructural and physicochemical characterization. *J. Biomed. Mater. Res.* **1989**, *23*, 883–894.

121. Kokubo, T.; Takadama, H. How useful is SBF in predicting in vivo bone bioactivity? *Biomaterials* **2006**, *27*, 2907–2915.

122. Porter, A.E.; Patel, N.; Skepper, J.N.; Best, S.M.; Bonfield, W. Comparison of in vivo dissolution processes in hydroxyapatite and silicon-substituted hydroxyapatite bioceramics. *Biomaterials* **2003**, *24*, 4609–4620.

123. Chien, C.-S.; Ko, Y.-S.; Kuo, T.-Y.; Liao, T.-Y.; Lee, T.-M.; Hong, T.-F. Effect of TiO2 addition on surface microstructure and bioactivity of fluorapatite coatings deposited using Nd:YAG laser. *Proc. Inst. Mech. Eng. Part H J. Eng. Med.* **2014**, *228*, 379–387.

124. de Bruijn, J.D.; Bovell, Y.P.; van Blitterswijk, C.A. Structural arrangements at the interface between plasma sprayed calcium phosphates and bone. *Biomaterials* **1994**, *15*, 543–550.

125. Bagambisa, F.B.; Joos, U.; Schilli, W. Mechanisms and structure of the bond between bone and hydroxyapatite ceramics. *J. Biomed. Mater. Res.* **1993**, *27*, 1047–1055.

126. Davies, J.E.; Baldan, N. Scanning electron microscopy of the bone-bioactive implant interface. *J. Biomed. Mater. Res.* **1997**, *36*, 429–440.

127. Porter, A.E.; Hobbs, L.W.; Rosen, V.B.; Spector, M. The ultrastructure of the plasma-sprayed hydroxyapatite–bone interface predisposing to bone bonding. *Biomaterials* **2002**, *23*, 725–733.

128. Radin, S.R.; Ducheyne, P. The effect of calcium phosphate ceramic composition and structure on in vitro behavior. II. Precipitation. *J. Biomed. Mater. Res.* **1993**, *27*, 35–45.

129. Fukuzaki, S.; Urano, H.; Nagata, K. Adsorption of bovine serum albumin onto metal oxide surfaces. *J. Ferment. Bioeng.* **1996**, *81*, 163–167.

130. Narayanan, R.; Seshadri, S.K.; Kwon, T.Y.; Kim, K.H. Calcium phosphate-based coatings on titanium and its alloys. *J. Biomed. Mater. Res. Part B Appl. Biomater.* **2008**, *85B*, 279–299.

131. Hsu, H.-C.; Hsu, S.-K.; Tsou, H.-K.; Wu, S.-C.; Lai, T.-H.; Ho, W.-F. Fabrication and characterization of porous Ti–7.5Mo alloy scaffolds for biomedical applications. *J. Mater. Sci. Mater. Med.* **2013**, *24*, 645–657.

132. Li, X.; Shi, J.; Zhu, Y.; Shen, W.; Li, H.; Liang, J.; Gao, J. A template route to the preparation of mesoporous amorphous calcium silicate with high in vitro bone-forming bioactivity. *J. Biomed. Mater. Res. Part B Appl. Biomater.* **2007**, *83B*, 431–439.

133. Izquierdo-Barba, I.; Ruiz-González, L.; Doadrio, J.C.; González-Calbet, J.M.; Vallet-Regí, M. Tissue regeneration: A new property of mesoporous materials. *Solid State Sci.*

2005, *7*, 983–989.

134. Campion, C.R.; Ball, S.L.; Clarke, D.L.; Hing, K.A. Microstructure and chemistry affects apatite nucleation on calcium phosphate bone graft substitutes. *J. Mater. Sci. Mater. Med.* **2013**, *24*, 597–610.

135. Weng, J.; Liu, Q.; Wolke, J.G.C.; Zhang, X.; de Groot, K. Formation and characteristics of the apatite layer on plasma-sprayed hydroxyapatite coatings in simulated body fluid. *Biomaterials* **1997**, *18*, 1027–1035.

136. Wang, X.-X.; Hayakawa, S.; Tsuru, K.; Osaka, A. A comparative study of in vitro apatite deposition on heat-, H2O2-, and NaOH-treated titanium surfaces. *J. Biomed. Mater. Res.* **2001**, *54*, 172–178.

137. Wang, X.-X.; Yan, W.; Hayakawa, S.; Tsuru, K.; Osaka, A. Apatite deposition on thermally and anodically oxidized titanium surfaces in a simulated body fluid. *Biomaterials* **2003**, *24*, 4631–4637.

138. Sugino, A.; Uetsuki, K.; Tsuru, K.; Hayakawa, S.; Osaka, A.; Ohtsuki, C. Surface Topography Designed to Provide Osteoconductivity to Titanium after Thermal Oxidation. *Mater. Trans.* **2008**, *49*, 428–434.

139. Ravelingien, M.; Hervent, A.-S.; Mullens, S.; Luyten, J.; Vervaet, C.; Remon, J.P. Influence of surface topography and pore architecture of alkali-treated titanium on in vitro apatite deposition. *Appl. Surf. Sci.* **2010**, *256*, 3693–3697.

140. Pecheva, E.; Pramatarova, L. *Modified Inorganic Surfaces as a Model for Hydroxyapatite Growth*; 2006;

141. Eichert, D.; Combes, C.; Drouet, C.; Rey, C. Formation and Evolution of Hydrated Surface Layers of Apatites . *Key Eng. Mater.* **2005**, *284–286*, 3–6.

142. Kokubo, T.; Hanakawa, M.; Kawashita, M.; Minoda, M.; Beppu, T.; Miyamoto, T.; Nakamura, T. Apatite formation on non-woven fabric of carboxymethylated chitin in SBF. *Biomaterials* **2004**, *25*, 4485–4488.

143. Zhang, Q.Y.; Cao, Y.; Chen, J.Y.; Feng, J.M.; Zhang, X.D. Comparative Study of Bioceramic Coatings in Static and in Simulated Physiological Conditions. *Key Eng. Mater.* **2002**, *240–242*, 319–322.

144. FAN, X.; CHEN, J.; ZOU, J.; WAN, Q.; ZHOU, Z.; RUAN, J. Bone-like apatite formation on HA/316L stainless steel composite surface in simulated body fluid. *Trans. Nonferrous Met. Soc. China* **2009**, *19*, 347–352.

145. Radev, L.; Michailova, I.; Stateva, S.; Zaimova, D.; Georgiev, H.; Apostolova, M. In vitro bioactivity of glass-ceramic/fibroin composites. *Process. Appl. Ceram.* **2017**, *11*, 136–146.

146. Kačiulis, S.; Mattogno, G.; Pandolfi, L.; Cavalli, M.; Gnappi, G.; Montenero, A. XPS study of apatite-based coatings prepared by sol–gel technique. *Appl. Surf. Sci.* **1999**, *151*, 1–5.

147. Solla, E.L.; Borrajo, J.P.; González, P.; Serra, J.; Chiussi, S.; Serra, C.; León, B.; Pérez-Amor, M. Pulsed laser deposition of silicon-substituted hydroxyapatite coatings. *Vacuum* **2008**, *82*, 1383–1385.

148. Boyd, A.R.; Rutledge, L.; Randolph, L.D.; Meenan, B.J. Strontium-substituted hydroxyapatite coatings deposited via a co-deposition sputter technique. *Mater. Sci. Eng. C* **2015**, *46*, 290–300.

149. Chung, R.-J.; Hsieh, M.-F.; Panda, R.N.; Chin, T.-S. Hydroxyapatite layers deposited from aqueous solutions on hydrophilic silicon substrate. *Surf. Coatings Technol.* **2003**, *165*, 194–200.